Variation and Fluctuations in a Bacterial Signaling Network

JOHANNES M. KEEGSTRA

This thesis was reviewed by:

prof. dr. F.J. Bruggeman	Vrije Universiteit Amsterdam
prof. dr. A. Briegel	Universiteit Leiden
prof. dr. T. Emonet	Yale University, New Haven, USA
prof. dr. P.R. Ten Wolde	Vrije Universiteit Amsterdam
dr. A. Vaknin	Hebrew University of Jerusalem, Israel

The research described in this thesis was performed at AMOLF, Science Park 104, 1098 XG Amsterdam, The Netherlands. This work is part of the research programme of the Netherlands Organization for Scientific Research (NWO).

Cover Design: Daphne Keegstra - Van Dooren, 2018
Printed by: GVO, Ede, The Netherlands

ISBN 978-94-92323-19-4
Nederlandse titel: Variatie en fluctuaties in een bacterieel signaalnetwerk

A digital copy of this thesis is available online at `www.ub.vu.nl` and `www.amolf.nl`.
Printed copies available on request via `library@amolf.nl`.

VRIJE UNIVERSITEIT

VARIATION AND FLUCTUATIONS IN A BACTERIAL SIGNALING NETWORK

ACADEMISCH PROEFSCHRIFT

ter verkrijging van de graad Doctor aan
de Vrije Universiteit Amsterdam,
op gezag van de rector magnificus
prof.dr. V. Subramaniam,
in het openbaar te verdedigen
ten overstaan van de promotiecommissie
van de Faculteit der Bètawetenschappen
op donderdag 17 mei 2018 om 15.45 uur
in de aula van de universiteit,
De Boelelaan 1105

door

Johannes Martijn Keegstra

geboren te Utrecht

promotor: prof.dr. T.S. Shimizu

Die größte Freude,
die ein Mensch in der Welt haben kann,
besteht in der Entdeckung neuer Wahrheiten.

— Friederich II von Preußen

Contents

1 Introduction

This chapter introduces some of the main concepts used in this thesis to the reader in four parts. First, the scientific questions regarding noise and variability in biology are discussed, with special attention to the influence of molecular noise on cellular physiology. Second, the biological model system to explore these concepts, the chemotaxis network in *Eschechia coli*, is introduced. This model system has been characterized in great detail in over half a century of research. Third, I continue with a discussion to the experimental approach to investigate the model system and describe *in vivo* Förster Resonance Energy transfer [FRET], a fluorescence microscopy method to measure signalling dynamics in living cells. Fourth, I give a brief overview of the contents of this thesis, in which the *in vivo* FRET technique is extended to the measurements of single-cell signalling dynamics in the chemotaxis network, to show that there is large variability in the chemotaxis system, both across individuals within a population and over time in single cells.

1.1 Variability in Biology

Life on earth is incredibly diverse and variable. It has been estimated that there are millions of species [39], ranging from the birds in the sky, fishes in the sea and creatures on land, but only a small minority has been catalogued, and only a few dozen species have been studied in great detail. Also within the same species enormous variability can be found. Remarkably, at the molecular level living systems are much more alike, with many processes conserved from bacteria to humans, most notably the expression of proteins from the genetic code. While the differences between genomes are greater between species, there is also diversity in genomes across individuals of the same species. Yet not all variability is determined by the genome. This is clear from the limiting case of genetically (nearly) identical individuals, which may still exhibit different phenotypes, such as the fingerprint of identical human twins or the fur pattern of genetically identical cats.

Figure 1.1: Example of non-genetic variability in biology. Fingerprints of identical twins are similar but not identical. Fingerprint data taken from [203].

Traditionally, variability between genetically identical individuals have been explained in terms of environmental differences. These are indeed important in shaping cellular physiology. In fact, research over the last decades has shown that environmental differences can lead to changes in the cell and can even become heritable without changing genetic code itself (this is called epigenetics [74]). While the exact impact of these mechanisms is still somewhat unclear, at least for higher organisms, it is a technical possibility to capture the information of certain environmental differences for later generations. But there is also an increasing body of evidence that shows that besides genes and environmental differences there is an additional source of variability: chance events within the molecular processes of the cell. While this purely physical source of variability was hypothesised already in the 1940's [45, 170], it received little attention before

the last two decades, when quantitative measurements of single-cells became feasable. In this section, I will describe the developments that lead to the belief that probabilistic processes have far reaching consequences for biological systems.

How did researchers come to embrace with the idea that living systems are shaped by chance? What are the necessary conditions for a biological system to be influenced by stochastic effects? Physicist Erwin Schrödinger, expressed his fascination for the coherence and order observed in living systems:

> *"For it is simply a fact of observation that the guiding principle in every cell is embodied in a single atomic association existing in only one copy (sometimes two)? and a fact of observation that it results in producing events which are paragons of orderliness" [170]*

At the time of writing — the early 1940's — Schrödinger was not aware of the molecular details of DNA, it was nearly a decade before the discovery of the double helix structure and identification of this molecule as responsible for storing the genetic information in the cell. Hence this implies he considered the expected disorder to be a property not specific to genes, but rather a general property of systems with a small number of components, of which genes are an example. Why was this a natural assumption to Schrödinger? He was a leading scientist in the field of quantum mechanics, a scientific theory with probabilistic principles at its core (as evident from the famous Schrödingers' cat thought experiment). One important difference between physical processes on a macroscopic scale (our world with typical length scales of meters) and the microscopic scale (the world of molecules and cells which is on the nanometer to micrometer range), is the importance of thermal noise, the ubiquitous fluctuations due to random molecular collisions, of which the typical magnitude (in energy units) at temperature T equals simply kT [133] (in which k is Boltzmann's constant, a fundamental physical constant). At room temperature, this equals approximately 4 pN·nm [133]. Hence for processes that operate at nanometer length scales with piconewton forces at room temperature, thermal noise becomes very relevant, and this is precisely the scale at which many cellular processes take place. However, averaging generally decreases variability. This is very clear in the case of rolling a dice. While the outcome of each roll of a dice is stochastic, the average outcome of many rolls will converge rapidly to 3.5 and the width of the distribution decays with the inverted square root of the number of events (a consequence of the central limit theorem, a fundamental result of probability theory). This means that if we average over thousands or millions of molecules or cells, effects of individual variation may become neglibly small and one can use deterministic chemical descriptions of reaction kinetics. But if the number of molecules is small, these stochastic effects may become important. The physicist Max Delbrück, who thought about a special class of chemical reactions around the same time as Schrödinger, namely autocatalytic reactions, thought also about the implications of small numbers.

Some proteolytic enzymes, like pepsin, are produced from a pepsin precursor in a autocatalytic process.

> *"In fact one molecule of pepsin should be sufficient under favorable conditions to covert in a few hours any weighable amount of pepsin precursor. In experiments designed to test this one must be prepared to encounter very large statistical fluctuations in the amount of reaction taking place in a given time" [45]*

And he also noted that this phenomenon should be studied more closely to find the "importance of such fluctuations for cell physiology". To study these effects in small systems required an enormous leap in technological improvements, because measuring the signals originating from a single molecule in among millions of other molecules is challenging. A first step was taken in the early 60's, when a technique was developed to stochastically encapsulate enzymes (Galactose) with substrates in small oil droplets. The enzyme converts the substrate into a fluorescent molecule, and this way it could be established that some droplets would contain only a single enzyme [162]. However, the signal produced by a single enzymatic reaction event was too small to be detected. Three decades later, researchers managed to directly measure the activity of a single enzyme with a sensitive microscope which collects the signal from a very small volume [110] and found that its activity fluctuates in time, the statistics of which revealed that enzymes undergo slow conformational changes that leads to concomitantly slow changes in the reaction rate. Hence the hypothesis is that since molecules behave stochastically, if a process depends only on a small number of reaction events, one expects to see stochastic effects at the system output level.

Before further discussing the consequences of molecular noise for biological processes in the following sections, I illustrate here with examples an important issue concerning measuring variability and measuring stochastic effects. While measuring variability is conceptually not difficult, it is much harder to establish that this variability is due to stochastic effects. Indeed, it could be that the process is itself completely deterministic but the initial conditions are variable and not known to the observer, just like the outcome of flipping a coin is completely deterministic but can be known only if one knows the initial parameters of the flipping [83, 115]. I mention two examples of output variability in a deterministic process, a simple one and a more complex one. The first is an oscillator, for example the cell cycle. Suppose each cell cycles at the same frequency, but the phases of each individual oscillations are not synchronised. If the response of each cell depends on its state in the cell cycle, the response of each cell can be variable. This has been shown experimentally in a population of bacteria responding to a salt shock, which induces a stress response. Because this response is cell-cycle dependent, and if it is non-linear, this leads to large diversity in responses within the population with a complex dependence on stimulus history

[116]. This simple example illustrates that observing cell-to-cell variation does not suffice to establish that the response of cells is stochastic. The second example of variability-without-stochasticity is chaotic dynamics. Perhaps one would think that observing erratic time series, with apparent sudden changes in activity, proves that a process is stochastic. It has been known for a while that simple discrete recursive relationships, that may look as innocent as $x_{n+1} = r x_n(x_n - 1)$ can generate exotic behaviour if the system moves into chaotic regime (if $r \gtrsim 3.57$). In a chaotic regime, small changes in the initial conditions generate a completely different outcome and the time series may look stochastic ([118, 199] and see Fig. 1.2).This is a strong contrast to non-chaotic systems in which small changes in the initial conditions generate proportionally small change in outcome. Dynamics of chaotic physical systems are deterministic in the sense that one can predict the outcome of the next event given knowledge of the present (Fig. 1.2c), yet demonstrate large variability because there will always exist finite differences in initial conditions, at the least due to thermal fluctuations. Such chaotic dynamics have been demonstrated experimentally within living cells. It was recently found that when observing the time it takes for cultured mammalian cells to divide does not correlate between mother and daughter cells and appears to be random, but shows correlation between grandmother and daughters indicating that there are deterministic factors transferred from mother to daughter cells [167]. Observing variability between cells or erratic time series is not sufficient to conclude that the underlying process is stochastic (Fig. 1.2). Importantly, both examples still require some source of noise to explain the breaking of symmetry between initial conditions between cells (e.g. to explain that the cell cycles are not synchronised), but this noise source can be a perturbation from outside of the cell and does not require any noise source internal to the cellular processes.

Now that we have discussed some possible origins of non-genetic variability, including but not limited to probabilistic processes in the cell, we proceed to zoom in on some biological processes which generate or propagate variability. First, the production of genes which leads to variability in protein levels of a cell (§1.1.1), then the consequences of molecular-level variability to more complex cellular phenotypes (§1.1.2), and finally we discuss a class of noise that is different from stochastic gene expression, namely stochastic effects in protein interaction networks (§1.1.3).

1.1.1 Stochastic gene expression

The chemical reactions at the heart of biology are concerned with replicating the genetic information and converting the information stored on genes into proteins. Since the copy numbers of genes are inherently low (typically one or two copies per cell), and because of the universal importance and shared design of gene expression across all domains of life (enshrined as “The central dogma" of

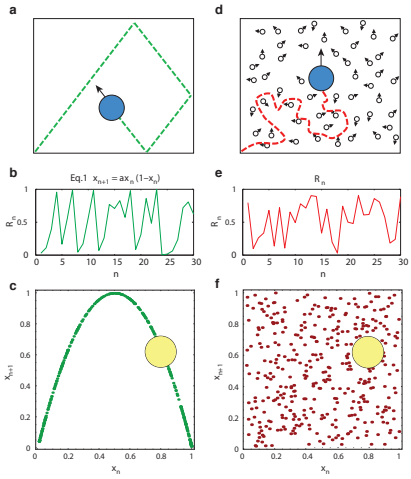

Figure 1.2: Similarity between time series obtained from a deterministic and stochastic process. **(a)** A small object's movement in an empty box. Prediction of its future location requires the knowledge of only its current location and velocity, thus the object's movement is deterministic, in contrast to the stochastic motion observed in e when the box is filled with a large number of colliding molecules. **(b)** The logistic map ($x_{n+1} = r x_n(x_n - 1)$, using r=3.99) as an illustration of a deterministic process resulting in seemingly stochastic output in time. **(c)**, Same kind of data as in (b) but then plotting recursively, each point is associated with coordinates (x_n, x_{n+1}), revealing the simple and low-dimensional relationship between sequential events. **(d)**, Same small object as in (a) but the box is filled with a very large number of colliding molecules. Now the motion is governed by a very large number of variables thus, the object's movement is considered stochastic.**(e)** Uncorrelated random numbers time series. **(f)** Plotting the same kind of data as in (e) recursively does not reveal a simple and low-dimensional relationship between subsequent points. Image reused from [167] with permission from Springer Nature.

molecular biology [41]) stochastic effects in the expression of genes has become the most thoroughly studied molecular source of biological variability. For many years there was no experimental evidence for stochastic gene expression because no general methods existed to measure the protein production in a single cell. This was changed rapidly in the late 1990's when a breakthrough in light microscopy revolutionised biology. While light microscopy has allowed us to study life under the lens since the 17th century, the ability to study specific biological processes was practically limited by a lack of contrast between different biological components. The discovery of proteins produced by certain marine animals that have fluorescent properties, combined with genetic engineering techniques that allow those proteins to be used as highly specific fluorescent labels or reporters in

a variety of organisms, lead to a breakthrough in the achievable imaging contrast [211]. Fluorescent proteins used as labels not only show the location of that particular protein in the cell, revealing important clues about its function, but also quantifying the amount of expressed protein at the single-cell level. Upon observing the fluorescence in a population of genetically identical bacteria, it was discovered that the amount of fluorescence varied greatly from cell to cell [55, 56].

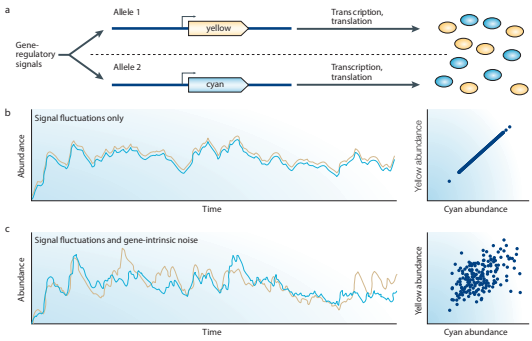

Figure 1.3: Intrinsic and extrinsic noise in stochastic gene expression. **(a)** Two genes encoding yellow and cyan fluorescent proteins, which only differ in a few amino acids, are expressed from identical promoters, and are influenced identically by upstream processes. **(b)** The abundances of the two expressed proteins are perfectly correlated when stochasticity in the biochemical steps that is intrinsic to the process of gene expression (gene-intrinsic noise) is absent and the effects of intracellular heterogeneity are negligible (left panel). A scatter plot of protein abundance that was obtained from a "snapshot" of a cell population contains points that are only on the diagonal (right panel). **(c)** Asynchronous protein abundances in the presence of gene-intrinsic noise are shown (left panel). Because the biochemical steps in the expression of the two genes are independent, gene-intrinsic noise causes the number of expressed proteins to differ, giving rise to a scatter plot that contains off-diagonal points (right panel). Evaluating the differences in expressed protein abundance within individual cells, and averaging these differences across a sufficiently large cell population can therefore provide a measure of the absolute magnitude of gene-intrinsic noise. Image reused from [79] with permission from Springer Nature, based on data in [55]

The observation that a population of cells with identical genomes and under identical environmental conditions exhibits such variability hinted at a stochastic process within the cell. However, another possibility is that gene expression is deterministic and only propagates variability in the input parameters. For example, the expression of genes could be oscillating (for example with the cell cycle) with the phases of the oscillator unsynchronized. A key experiment in this field observed the fluorescence from two different fluorescent proteins, CFP (Blue)

and YFP (Yellow/green) [55]. These fluorescent molecules differ only by a few amino acid residues, which means their difference in sequence does not affect expression characteristics significantly, while shifting the emission spectrum such that they can be detected separately. In a dual reporter experiment, one can also plot at a given time the fluorescence intensities of YFP versus that of CFP, which is proportional to the amount of CFP and YFP molecules in a single cell. In such a plot, one can distinguish variability along the diagonal and orthogonal to the diagonal (Fig. 1.3). Any source of variability that affects both genes, such as cell cycle, the availability of cellular resources, will cause correlated variability that spreads along the diagonal. If there is also a noise source that affects both genes independently, this would increase variability in direction orthogonal to the diagonal. And since *yfp* and *cfp* are so similar in sequence, it is reasonable to assume that these genes would be affected identically by any extrinsic noise source. Hence the observation that there is in fact a significant off-diagonal component in the variability, strongly indicates that the expression of each single gene is subject to variability that is uncorrelated with that of other genes. Observation of stochastic gene expression has not been limited to bacteria, but has been also measured in yeast [16], animal cells [154] and artificial cell-sized lipid vesicles [139]. This has made stochasticity in gene expression a well established concept [79, 156, 160].

Stochastic production of proteins has been directly observed by counting the number of new molecules that is produced over time [27, 70, 235]. Before these observations, gene expression was commonly thought of as a process with constant transcription and translation rates, and as a result one expects the protein levels across cells to follow a Poisson distribution, in which the variance is identical to the mean [195, 209]. The relative noise of gene expression of a protein p with expression level N_p and variance σ_p^2, often quantified in the coefficient of variance $CV = \sigma_p / N_p$ then scales with $1/\sqrt{N_p}$. This contribution would drop below a few percent and therefore be negligible (at least in most cellular processes) if the number of proteins exceeds $\approx$1000. The fact that even at such high expression levels much greater noise was observed, indicates that the distribution is in fact not Poissonian, and this has been explained due to the “burstiness" of the transcription process observed in the molecular counting experiments mentioned above. A simple mechanistic model for bursty gene expression considers that a gene can be in two states, an active and silent state. When activated, it produces a large amount of mRNA molecules (a transcriptional ‘burst’) and when silent no mRNA molecules are produced. Production can be modulated by changing the bursting frequency, rather than the transcription rates per se.

Two questions naturally arise from the observation that there are stochastic effects in gene expression: how large are such fluctuations for each gene, and over what timescale are they correlated? The noise amplitudes are discussed first. Noise amplitudes or noise levels (η) are usually quantified in terms of the

standard deviation over the mean. It is hard to predict what the noise amplitude of a particular gene is, even if the average expression level is known. This is because of three reasons. First, the idea of burstiness has some important consequences. As mentioned above, a poisson distribution only has a single parameter - its mean- and hence to know the expression level is to know the variance. However, the bursty model leads instead to a gamma distribution [66] which is characterized by two parameters, that can be related to the translation and transcription strengths. The same expression level can have large noise (weak transcription strong translation) or low noise (strong translation weak transcription). Importantly, this means there is no one-to-one relation between expression level and noise. Second, within a network of molecular interactions, noise arising from copy-number fluctuations in a low abundance component may propagate to cause also in large fluctuations in highly expressed components [147]. While protein levels are readily measured with fluorescent probes, measuring the dynamics of gene regulatory networks [53] with multiple components is more challenging because the number of species one can monitor is limited. Nevertheless, probing network components with fluorescent reporters has shown interesting results in gene regulation networks, such as noise-induced qualitative phenomena such as bacterial stress response [107] competence [200] and cellular differentiation [155]. A third reason why noise levels are hard to predict a priori is because there is another source of noise, different but hard to distinguish from expression noise, namely noise from protein partitioning at cell division [76]. At each cell division, proteins become randomly distributed between the mother and daughter cells leading to differences in the protein levels of genetically identical cells. While this effect is in principle small at high expression levels, it has been shown experimentally that the partitioning of cell-pole associated efflux pumps create long-lived diversity between bacteria [15]. If proteins form large aggregates, for example chemoreceptor arrays (see §1.2.2 below), partitioning noise may add a significant contribution to the observed cell-to-cell variation in copy numbers, even at high expression levels.

Although there is no one-to-one correlation between protein expression level and expression level variability, an experimental study with many (but not all) genes in *E. coli* did find some trends in the relation between expression and noise levels. For very low expression levels noise scaled with the inverse square root of the number of molecules (as predicted by Poisson statistics), for higher expression levels the noise reaches a noise floor of 30 %, which is interpreted as an extrinsic noise floor [202]. However, this interpretation seems questionable given that another study could measure extrinsic noise levels as low as 5 % [55].

The typical correlation timescales of gene expression have received much less attention compared to the amplitudes. Since the lifetime of proteins is much longer than the cell cycle, and since most proteins are not actively degraded, the protein concentration is primarily determined by the balance of production and dilution due to cell growth. Since production and destruction rates must be equal

(on average) at steady state the timescale of the gene expression variability is on the order of the cell division time [52, 89], and manifests itself as differences between cells of protein levels that are stable over the cell's lifetime.

1.1.2 From molecular noise to phenotypic diversity

While variability in protein copy numbers due to stochastic gene expression is an interesting finding, it is important to consider how this variability in copy numbers affects cellular decisions and behavior. Each protein is part of a network of chemical interactions, and usually the function of such network does not depend only on which kind of proteins are present, but also their numbers. Suppose we could write for a particular steady-state cellular parameter a, and function F that maps the number of all relevant proteins ($\vec{p}$) to this parameter a

$$a = F[\vec{p}(t)] \tag{1.1}$$

But without explicitly formulating F, we know that the parameter's sensitivity dF/dp_i is the dependence of a on protein p_i. If this derivative is nonzero, this means that variability in a protein p_i causes variability in parameter a, but how much will depend on the specific network that is described by F. Hence the variability in a parameter is propagated by the network to the level of phenotypes, which is commonly referred to as noise propagation. The functional form of F is determined by the network design, and hence to properly understand how variability in protein copy numbers propagates to cellular behavior we need to understand the network itself. Of course, the function F might be incredibly complicated and might remain unknown in many cases, and there is no guarantee that there is a one-to-one mapping.

While many regulatory networks involve the regulations of genes, many signaling systems process signals by means of post-tanslational modifications such as methylation or phosphorylation of particular proteins or protein complexes. This allows these systems to operate on a much shorter timescale compared to gene regulatory processes. In such systems fluorescent copy number reporters cannot be used to infer the network's state. Because the dynamics of such systems are much harder to study, the effect of noise and network topology on signaling systems has received attention from a theoretical perspective [90], but to date little work has been done on experimental noise level comparisons of network topologies in protein interaction networks.

For meaningful statements about the influence of biological networks or circuits one requires to experimentally contrast high-noise architectures with low-noise. This is challenging because one needs to change the architecture of the network such that the network still functions properly and only the variation of the bahavior changes, while the average behavior remains the same. Therefore,

systematic comparisons of network topologies are rare.

Below, I discuss three important concepts that are important in understanding the relation of variability in behavior and molecular noise. First, molecular variability is abundant and may be detrimental for cells. Hence biological circuits (the function F) need to be designed in such a way to be invariant or robust against molecular variability. (§1.1.2.1). This implies that networks have evolved to protect certain critical functions from changes in gene expression, and generally networks have evolved towards a situation where the network reduces noise. The second idea is that there is signifiant cost involved in suppressing molecular fluctuations and therefore detrimental noise can in some cases not be fully suppressed (§1.1.2.2). The third concept is that networks are evolved to exploit the molecular variability to generate diversity in particular cellular parameters, and that this diversity is useful (§1.1.2.3). Of course, all of these three concepts are may apply to the same cellular parameter.

1.1.2.1 Robustness

An important concept when discussing cellular regulatory networks is robustness [87]. This means that the output of a network is stable despite variation in physical and biological parameters. Biological processes operate in a fluctuating environment at both the microscopic (molecular fluctuations) as well as the macroscopic level (day-night cycle, weather). Hence any biological system must possess some degree of robustness against variation, but in some systems this is more critical than others. In many developmental processes a high degree of robustness is required. For example, after a (possibly stochastic) cell fate decision, in many cases the cell should stay committed to its cell type [92]. In the case of signal transduction, the output needs to be sensitive to variation in the input parameter to transmit information, but ideally completely insensitive to changes in any other parameters.

Sensitivity to variability in the output of one particular system does not necessarily imply the overall behavior is also sensitive. Complex cellular phenotypes often depend on the output of multiple subsystems. In the case of the bacterial sensing and response to chemical gradients, it has been shown that while individual subsystems of the signaling circuit are not robust to changes in temperature, the overall swimming behavior remains robust [140]. Hence statements about robustness without much context need to be interpreted with caution.

There are many examples of robustness in network behavior, mainly from a theoretical perspective. For feedback systems responsible for network phenomena such as sensory adaptation it has been shown that a system in which network dynamics only depends on the activity of the network yields robust adaptation [3, 10]. Also bifunctional enzymes, which are able to perform opposing operations on the same substrate, have been shown to create robustness to copy numbers and ATP

concentration in bacterial two-component signaling systems [184]. Robustness to copy number variability due to gene expression noise has been shown theoretically in bacterial chemosensing, in which many output parameters of the system do not depend on absolute numbers but always on the ratio of two pairs of enzymes [90]. This makes the system robust agains correlated expression variability (extrinsic noise), while sensitive to uncorrelated variability (intrinsic noise). The operon architecture of the chemotaxis signalling pathway, which makes the expression of the transcriptionally coupled, is thought to be an important aspect of the network since this reduces the uncorrelated (intrinsic) noise between the expression of two enzymes by expressing them from mRNA molecule. However, a alternative study showed that on the level of the entire genome the effect of gene clustering on operons is much smaller compared to just protein expression levels [105].

How general are the noise attenuating properties of a network motif? Feedback mechanisms are often invoked to explain robustness, but the same network motif may increase or decrease robustness depending on its operating regime and parameters. For example, negative feedback motifs are generally associated with reducing variability. However, negative feedback can, in some circumstances, generate oscillations or fluctuations. Positive feedback loops can either generate variability by amplifying small fluctuations, but two coupled positive feedback systems can produce a bistable system which is generally a stable network motif. In turn, a bistable system can also increase variability if the system operates very close to the transition point between the two states. Hence it is impossible to describe the noise modifying properties of a network motif without any knowlegde of its parameters.

1.1.2.2 Cost of fluctuation suppressions

Why would any system that has evolved long enough lack robustness, even if the created variability is detrimental? Recently, it has also become clear that there is an additional constraint on the robustness of biological systems, namely the costs to reduce variability. For example, decreasing copy number fluctuations of by increasing protein copy numbers can become a costly affair since the noise is reduced only by the square root of the number of molecules. Suppressing fluctuations with feedback loops requires the feedback signal to be produced many more times, and hence an optimal noise reduction system can only reduce the noise with the fourth root of the number of control molecules [99]. The fact that there is significant cost involved in suppressing fluctuations does not argue against the existence of negative feedback in biological systems, but it does show that there is a trade-off between suppressing variability and resource spending. In an example of sensory adaptation of bacterial chemosensing, in which a signalling system after prolonged stimulation returns precisely to its prestimulus value (which is a dissipative system), it has been predicted theoretically that perfect adaptation to

large chemoeffector stimuli requires infinite energy [168]. Hence, in some cases noise is technically detrimental for the cell but it is not critical enough to justify the energy expenditure to further minimize the variability.

1.1.2.3 Diversity as a bet-hedging strategy

Especially in the case of microbes, it is a well established idea that under some circumstances it is beneficial to generate diversity within a genetically identical population [1, 44, 222]. For frequent environmental changes it is usually best to sense and respond to the environment, but for infrequent but nevertheless drastic changes it might be more efficient to stochastically switch between phenotypes because it releases the burden of spending resources on sensing and dicision making [93]. For example, to have a fraction of non-growing cells within a population has been shown to be very useful in increasing the communities resilience against stress and antibiotics [46] because faster growing cells are generally more vulnerable to antibiotic treatment. Phenotypic diversity may also facilitate evolution through fitness valleys [155].

There are several mechanisms to create diversity, and one of them is noise from molecular processes such as gene expression. A classic example of noise induced bed-hedging is cellular competence in *B. subtilis*. While the uptake of DNA may have important advantages, it also makes the cell vulnerable to invaders. Hence it makes sense to only enable a small fraction of the population with the ability to uptake DNA. It was found that the necessary and sufficient condition for competence, expression of the ComK transcription factor, is functioning in a simple bistable network with high and negligible expression levels of ComK. It was found that the intrinsic noise in the expression of *comK* allele may cause the expression of a cell to switch between one of the two stable states [200]. Another example in *B. subtilis* is the exploitation of gene expression noise to generate pulsed activity in the stress response network [107].

Bed-hedging might also be useful in conditions where the environmental constraints are diverse and lead to certain fundamental trade-offs in optimizing fitness. This means there is not a single phenotype that is optimized for all of this diverse set of constraints (‘generalist’). There may be phenotypes that perform well in one environment but poorly in others (‘specialists’). There are some examples from the context of bacterial motility where this is important. For example, a numerical study has identified a trade-off between the ability to climb shallow and steep chemical gradients [65]. Without variability, the population would do very well in one circumstance but perform poorly in the other and vice versa. However, stochastic gene expression can be exploited to generate diversity in genotypes. In some environments, it may be beneficial to generate a mixture of different specialists instead of a homogeneous population of generalists.

1.1.3 Stochastic protein-protein interactions

Gene expression is only one class of biochemical processes that show stochastic dynamics, but the interaction between gene products can also be stochastic. There is no reason to assume the reactions involved in gene expression are special in any chemical sense, it is only that in gene expression low number fluctuations are expected because of each gene there are typically one (or two) copies. Generally the number of reaction events in many other processes is much larger, and a deterministic description is sufficient. However, in many processes in biology, and especially signaling, proteins operate in macromolecular complexes, which not only reduces the effective number of units but also causes nonlinear behavior, including signal amplification, that may enhance the fluctuations in one part of the network.

However, protein-protein interactions are much harder to measure directly. One strategy to measure the interactions is to measure the output or input molecule of a process (for example by measuring the input of radioactively labeled substrate molecules) but such measurements average over many cells and the effects of fluctuations are lost. Another strategy is to measure interactions directly, for example with a FRET probe, which is the strategy outlined in this thesis, provided this method is applied to single cells instead of populations. Stochastic effects in biochemical reactions have been measured only *in vitro*, such as the aforementioned single enzyme activity experiments. Yet there have been no measurements of stochastic dynamics within a protein interaction network *in vivo*, with the exception of microtubule growth dynamics [179].

How does any non-genetic temporal noise affect behavior? While gene expression noise in bacteria generally manifests itself as stable cell-to-cell variation, with temporal changes on the order of the cell cycle, noise in protein-protein interactions affects cellular physiology on much smaller timescales. For processes taking place on such timescales, such as signaling, noise will have a profound impact on the functioning of the network and downstream processes. For equilibrium processes, in which no energy is consumed, the response timescale and steady-state fluctuations in the system are deeply related, which is described in the fluctuation-dissipation theorem. In the simple example of a bead in a bath of colliding particles (Fig. 1.2d) the friction force on the particle is determined by the colliding particles and these friction forces will counteract any external force that tries to displace the bead. While this relation in principle is restricted to equilibrium systems, it has been shown experimentally in bacterial swimming behavior that the recovery to a stimulus scales linearly with the steady-state noise level, e.g. low noise means fast recovery [143], generalizing the established fluctuation dissipation relation to a fluctuation response theorem for non-equilibrium systems but with defined steady-state [152].

Importantly, even in case biochemical noise does not propagate to behavior

measuring fluctuations may still be very useful. Like measuring gene expression noise can be useful to understand gene regulation, in which different regulatory circuits may be only discrimminated by their expression variation [131], measuring biochemical noise can be used to infer properties of protein networks. Similarly, the widely applied Fluorescent Correlation Microscopy [FCS] technique can measure protein concentration and effective protein sizes in single cells from fluctuations within a small volume due to molecules behaving as Brownian particles [36, 114] but these fluctuations themselves do not have large impact on cellular physiology.

In summary, we have seen that biology is variable and part of this variability can be explained by stochastic models. The best studied example is gene expression, which leads to cell-to-cell variation of gene copy numbers in an isogenic population. Since these proteins operate in large networks this cell-to-cell variation can lead to different cellular phenotypes. While there have been some experimental studies in gene regulation networks, there are still many open questions remaining on the relation between network topology and cell-to-cell variation. Especially, the consequences of such noise for protein interaction networks without gene regulation is much less clear. Furthermore, the reactions between the proteins are also stochastic and could also lead to additional variability, which has been hypothesized but never directly measured. Below, we discuss an example of a highly characterized protein interaction network which can operate in the absence of dynamic gene regulation, namely the chemotaxis network in *E. coli*.

1.2 Chemotaxis in *E. coli*

1.2.1 Modulating a biased random walk based on sensory input

Chemotaxis refers to the ability of self-propelled organisms to measure and respond to their chemical environment. Chemotaxis in *E. coli* and closely related species is among the most widely studied biological phenomena, and has been serving as a textbook example for signal transduction for decades. The importance of bacterial chemotaxis as a model system for signal transduction has been colloquially compared to the hydrogen atom in quantum physics. Therefore, there are excellent reviews on the chemotaxis system [12, 144, 194, 213, 224] and we will limit ourselves to the basics in *E. coli* and the closely related network of *Salmonella*. (The networks of *V. cholerae, B. subtillis, Rhodobacter, Caulobacter and Pseudomonas*, also have have been investigated in some detail [19, 151, 157, 166]). Many bacterial species, including *E. coli*, possess several long flagellae which they can rotate to generate a propulsive force. If all flagella rotate in the same direction (usually defined as counter-clockwise), the cell propels

itself forward in relatively straight paths. When one of these flagella starts rotating in the opposite direction, the flagella bundle gets disrupted and as a result the bacterium tumbles. After the tumble ends, the next run follows which is generally in a different direction than the run direction before the tumble. In the absence of a ligand stimulus, this executes a three-dimensional random walk. When favourable chemical stimuli are present, this random walk can be biased by extending (shortening) runs if the cells experience a positive (negative) temporal gradient of attractant (Fig. 1.4a). To do so, cells sense temporal gradients in extracellular ligand concentration while retaining an approximately constant swimming speed. Hence measuring a temporal gradient allows the bacterium to effectively measure a spatial gradient of the ligand. Sensing ligands suppresses tumbles, while the absence of ligand promotes tumbles. Hence on average the direction of motion will be towards food, and away from repellents. The chemotaxis network that

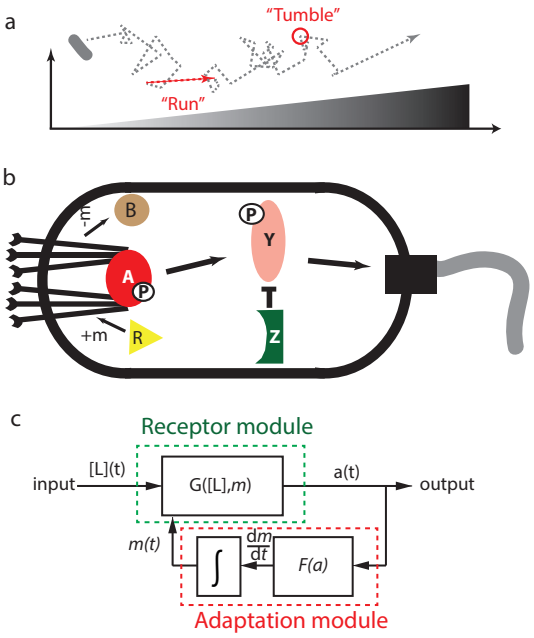

Figure 1.4: Bacterial chemotaxis. **(a)** Chemotaxis pathway enables climbing of chemical gradients by biasing its run-and-tumble random walk. It suppresses tumbles when climbing up a favourable gradient. **(b)** Schematic depiction of the molecular interactions within chemotaxis pathway in *E. coli*. **(c)** Modular architecture of chemotaxis pathway. Image courtesy Tom Shimizu [183]

controls the behavior is a network in which the information is processed by interactions between proteins only (Fig. 1.4b). Transmembrane chemoreceptors

bind ligand, which results in a conformatonal change that corresponds to an active and inactive state. This in turn controls the activity of a kinase, CheA. The kinase autophosphorylates when active, and transfers its phosphate group to the response regulator CheY. Meanwhile, CheZ dephosphorylates CheY. CheY-P binds to the base of the flagellar motor, which increases the chance of running clockwise, which initiates a tumble. Ligand binding to the receptors causes the kinase becomes inactive, consequently the phosphorylation of CheY ceases and the CheY-P level decreases to zero, which suppresses tumbles. To measure temporal gradients cells need not only to measure the instantaneous concentration of ligand as well as using memory to compare the measured value with the recent past. The mechanism of memory storage uses covalent modifications of the chemoreceptors, mediated by the enzymes CheR and CheB, that respond to changes in activity of the chemoreceptors. CheR methylates the modification residues of inactive chemoreceptors, while CheB demethylates active chemoreceptors. Methylation to a chemoreceptor decreases the receptor sensitivity, effectively counteracting ligand binding of receptors, while demethylation enhances the sensitivity.

This mechanism of methylation and demethylation leads to sensory adaptation. When a stimulus is applied continuously, the kinase activity responds and shuts down, but the activity then gradually recovers to its prestimulus level. Sensory adaptation is a key network motif in many signaling systems including human vision [112, 132, 153]. For the bacterial chemotaxis system, it provides the basis for the fact that bacteria respond identically to different absolute stimulus sizes, if the fold-change of the stimulus compared to the background is the same [98].

1.2.2 Structure and function of chemoreceptor arrays

It has been well established that chemoreceptors, together with kinases and scaffolding molecules, form clusters on the cell membrane. These clusters are important many aspects of the signal processing, such as signal amplification, integrating multiple signals and sensory adaptation. Light microscopy studies found that many cells have one or two large chemoreceptor clusters (Fig. 1.5a), usually located close to the cell pole, with an occasional large lateral cluster [210] and many small ones [71]. Although the function of the individual components was established by the mid-90's [62], the molecular structure of the assembly is a more recent discovery [144], and did especially benefit from developments in light and electron and microscopy [24, 71].

The structural organization of such an array, as observed from the top, is a repeated hexagonal lattice (Fig. 1.5b-c), which was shown by electron-microscopy to be a property of chemosensory arrays in many other bacterial species [25, 26]. Observed from the sides the structure is sandwich-like, with the inner membrane as an upper layer, the lattice of CheA and CheW underneath and the chemoreceptors connecting the two layers (Fig 1.5d. Interestingly, a course-

grained prediction of the side view based solely on the structure of the individual components turned out to resemble the eventually measured structure [182]). A core unit of the hexagonal array consists of a CheA dimer, a CheW molecule and six chemoreceptor monomers, ordered in a trimer of homodimers. The *E. coli* chemotaxis network operates with five chemoreceptor species, of which the serine-sensing Tsr and aspartate sensing Tar are the most abundant, and homodimers can form trimers with other chemoreceptor species. This way the chemosensory arrays can integrate the input of several chemoreceptors into a single output variable. The kinase activity of a core unit has been shown to respond, with low cooperativity, to ligand stimuli *in vitro* [104] and *in vivo* [149]. Highly cooperative responses, important for signal amplification, only occur when core units can link to form larger arrays [149].

The smallest functional chemoreceptor unit is a homodimer molecule (Fig. 1.5e). It has a long ($\sim$ 30 nm) and elongated structure of which the binding domain of the chemoreceptor is located in the periplasm, but most of the chemoreceptor is located within the inner membrane. The conformational state of the chemoreceptor is determined by ligand binding in the binding pocket as well as the modification sites in the sensory adaptation domain. The receptor tip is located at the CheA-CheW base plate and is important for transmitting the active or inactive state to the kinase. In addition to binding of the adaptation enzymes CheR and CheB to the modification sites, they can also (with a distinct binding site [231]) bind to a pentapeptide region (NWEFT sequence motif) located at a flexible tether attached to the main structure of the chemoreceptors. When bound to the tether, the adaptation enzymes can modify not only multiple modification sites of a chemoreceptor, but also of neighboring receptors in the array [100, 103], which is thought to ensure the sensory adaptation to stimuli is complete [59, 150].

1.2.3 Quantitative models of pathway activity

There are many quantitative models of the bacterial chemotaxis pathway [213]. The separation of timescales between activity changes due to ligand (fast) and to adaptation (slow) allows to treat these two aspects of the system as different modules of the pathway (Fig 1.4c). This allows to describe the system with two equations, one for each module [215]:

$$\begin{aligned} a &= G([L], m) \\ \frac{dm}{dt} &= F(a) \end{aligned} \tag{1.2}$$

the model includes three parameters, the ligand concentration $[L]$, the activity a, and the adaptation (or methylation) state m. Given a certain $[L]$ and m, the system responds as described by the ligand sensing module G. Given this change

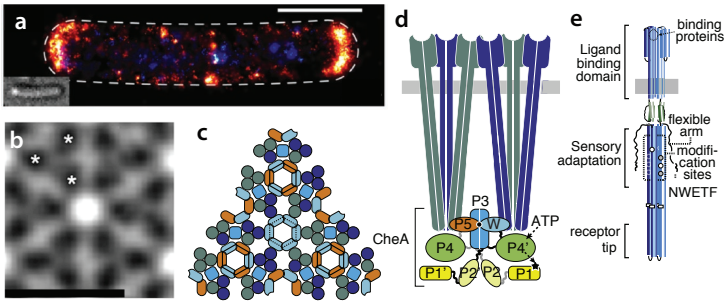

Figure 1.5: Chemoreceptor array structure at cellular and molecular level **(a)** Chemoreceptor clusters in a single cell visualized by PALM imaging of labeled chemoreceptors. Tar receptors measured with TIR PALM (blue), which only measures receptors on the bottom membrane, are shown separately from Tar receptors measured with EPI PALM (red). Scale bar 1 μM. Inset shows a differential interference contrast image of the same cell. Image taken from [71]. **(b)** Top view of chemoreceptor array structure, sub-tomogram EM averages. Stars indicate the position of a single receptor dimer. Scale bar 12 nm. Image taken from [25]. **(c)** Schematic depiction of chemoreceptor array architecture, top view, showing chemoreceptors (blue and green circles), CheA domains (P3, blue and P5, orange) and cheW (light blue). **(d)** Chemoreceptor array and CheA structure, side view. Shown are six transmembrane receptor dimers, a CheA dimer and one CheW molecule. Colors as in (c), **(e)** Chemoreceptor dimer and with signalling domains, modification sites and tether indicated. Panels c-e reused from [144] with permission from Elsevier.

in activity, the methylation state m is changed as described by the function F. We briefly discuss F and G separately below.

Ligand sensing

For the function G a simple two-state non-dissipative model has been highly successful. This means the chemoreceptor is either active ('on') or inactive ('off'). At the molecular scale, this allowed for the application of the methods of statistical physics, and hence one can write the activity as a function of only the free energy difference Δf between the active and inactive state.

$$G = \frac{1}{1+\exp\left[\Delta f\right]} \tag{1.3}$$

The model needs to reflect the observation that chemoreceptors within the array influence each others activity [193]. Typically, Ising-type models, originally formulated to describe ferromagnetism, have been used to model such systems of interacting subunits [50, 77, 180]. The limit case of an Ising model with strongly

coupled teams of fixed size N is the MWC model [129], in which the complete chemoreceptor team is either active or inactive. The energy has contributions from ligand binding and methylation and equals $\Delta f = N(f_L + f_m)$. The second term f_m was constrained by experimental data to be linear decreasing function of m [183]. If the receptor-ligand binding is a non-dissipative (equilibrium) process, the binding and unbinding of ligand obeys detailed balance and the energy becomes $f_L = \ln(1 + [L]/K_I) - \ln(1 + [L]/K_A)$, which is a function only of the ligand concentration $[L]$ and the binding constants of the active and inactive chemoreceptors, respectively K_I and K_A. Hence the chemoreceptor can respond to ligand concentrations between K_I and K_A, and G has approximately sigmoidal shape (Fig. 1.6).

Sensory adaptation

For the methylation function F a large number of models has been proposed (see references below), but in many cases they share the assumption is that CheR binds only to inactive receptors and CheB only to active receptors [10]. For simplicity, we assume the reaction rates to be linear, and in such a situation we can write for the methylation rate

$$F(a) = \frac{dm}{dt} = k_R[\mathrm{R}](1 - a) - k_B[\mathrm{B}]a \tag{1.4}$$

in which a is the activity of the chemosensory array, [R] and [B] are the concentrations of respectively CheR and CheB, each with a rate constant $k_{R,B}$. For such a model it is easy to show that for steady-state one obtains an activity a_0 of

$$a_0 = \frac{k_R[\mathrm{R}]}{k_R[\mathrm{R}] + k_B[\mathrm{B}]} \tag{1.5}$$

Importantly, this expression does not depend on the ligand concentration, hence in time the ligand responds perfectly a_0. Changing the rate terms, $k_R[\mathrm{R}]$ and $k_B[\mathrm{B}]$, to something more complicated than simple linear terms, will not change this adaptation property, provided these terms do not depend on the ligand concentration.

With such a simple model one can explain the response dynamics in response to arbitrary ligand input stimuli, in which the basic assumption is a separation of timescales between a fast response of the ligand sensing and much slower adaptation kinetics [122]. The simplest case is the addition and removal of step stimuli of attractant. In the absence of any ligand the activity will be at its steady-state level (Fig. 1.6, triangles). In wildtype cells, this equals approximately 1/3 and is determined by the expression level ratio of the adaptation enzymes. The ligand sensing function G_{initial} describes the initial fast response magnitude to

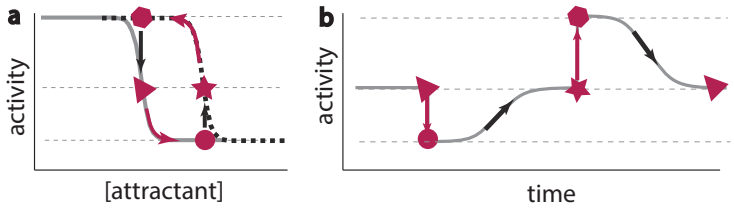

Figure 1.6: Ligand sensing and adaptation. **(a)** Sensing and adaptation in ligand-activity space. Adding a saturating stimulus decreases the activity from baseline (triangle) to zero (circle) as described by the ligand sensing domain. Adaptation reduces the sensitivity of the chemoreceptors and effectively shifts the dose response curve (dashed line), and the activity recovers to its prestimulus value (star). Removing the same stimulus again increases the activity (polygon). Adaptation enhances the sensitivity and shifts the dose response curve to the baseline value (triangle). **(b)** Sensing and adaptation in time. The symbols in the time series correspond to the positions on the dose response curve shown in panel (a).

the stimulus (Fig. 1.6, solid grey line). A saturating stimulus will decrease the activity to zero (Fig. 1.6, circles). Then the adaptation system starts to slowly methylate the chemoreceptors (increasing m), which shifts the function G_{initial} to become less sensitive (Fig. 1.6, dashed line). After some time of methylation the activity starts to recover until it is back at its steady-state level (Fig. 1.6, stars). When removing the stimulus, the adapted function G_{adapted} describes the activity as a function of ligand and the activity reaches a maximum (Fig. 1.6, hexagon). Then demethylation brings the dose response curve back to its initial status, and consequently the kinase activity back at its steady-state level.

There are many possible alternatives to and refinements of this simple model mentioned above, that each try to capture some phenomena not well described by the simple linear description of the adaptation kinetics. This can be done by applying different biochemical concepts to the model of the adaptation system, such as including Michaelis-Menten kinetics to account for possible saturation of the enzyme capacity [57], or the fact that there seems to be an asymmetry in the responses kinetics of the responses mediated by CheR and CheB [35]. It is also possible to include the fact that in wildtype cells there are more than one receptor species [97]. Also, some models include the possibility that CheR and CheB can branchiate through the chemosensory arrays [59, 100], or the fact that the methylation and demethylation reactions require energy and hence the rates will slow down when approaching a_0 [168] and the fact that the number of methylation sites is limited and therefore adaptation may be incomplete [136]. Also, it has been shown that CheB can be phosphorylated like CheY, which increases its demethylation activity. The purpose of this additional feedback loop is still poorly

understood, and is discussed in Ch. 3 of this thesis.

1.2.4 Individuality in *E. coli* chemotaxis

While many signaling parameters for the quantitative models described above have been characterized in population-averaged measurements [183, 193], cellular individuality is also a long standing tradition in the field of bacterial chemotaxis [13, 172]. In fact, a pioneering study by Spudich and Koshland in the 70's [195] on bacterial individuality was concerned with bacterial chemotaxis and actually proposed that stochastic processes could lead to variation in protein copy numbers in the cell, long before single-cell expression levels could be measured. They used cells tethered by their flagella to a glass coverslip and observed the rotation of the bacterium. The rotation direction (clockwise or counterclockwise) indicates wether the cell is performing a run or a tumble, and adding chemoattractants changes the tumble rate of the cells. They were surprised to learn that the recovery of the tumble rate after ligand addition due to sensory adaptation varied greatly from cell to cell. The differences in adaptation times between individuals were large (50%) and these differences persisted over multiple generations, it was found that this behavioral individuality could not be explained by changes to the genome (by random mutations) or differences in cell cycle. Hence they hypothesized that this non-genetic individuality originates from low number fluctuations of proteins in single cells. After their discovery, two other studies have also found large variability in adaptation times [14, 127] and also the steady-state tumbling bias was found to vary from cell to cell [225]. Furthermore, it has been established experimentally that some behavioral parameters within a single cell vary in time [91].

What makes *E. coli* chemotaxis such a good model system for relating molecular noise to behavioral variability is the possibility to make quantitative measurements of the cellular phenotype and a high level of understanding of the molecular mechanisms. When combined with genetic protein labeling, the behavior can then be directly compared with protein copy numbers, as is done recently [49]. Another experimental convenience is that the network is decoupled from gene expression. Unlike many other two-component systems, the response regulator (CheY) is not a transcription factor. Hence in cells in which gene expression is disabled the chemotaxis pathway still functions properly. The bacterial strain RP437, wildtype for chemotaxis experiments [145] is an auxotroph, which means that if the cells are placed in a medium without particular amino acids, gene production and growth will cease. Another contributing factor that adds to the experimental convenience is that the chemotaxis pathway is relatively isolated from not only gene expression.

1.3 Förster Resonance Energy Transfer

Förster Resonance Energy Transfer [FRET]* is the energy transfer from one fluorophore (the donor) to another (the acceptor). The energy transfer depends on several properties of the fluorophores, and one important property is the spectral overlap between the emission spectrum of the donor and the excitation spectrum of the acceptor, although the energy transfer is actually nonradiative (e.g. there is no photon exchanged between donor and acceptor) and proceeds by dipole-dipole interactions. In the absence of FRET, excited donor molecules relax to their ground state by emitting a photon which can be detected. However, in FRET an excited donor molecule transfers its energy to the acceptor molecule and does not emit light, while the acceptor does emit a photon. Since the acceptor emission wavelength generally longer than the donor emission wavelength, the emitted light of the acceptor and donor can be measured separately and the ratio of acceptor over donor fluorescence emission can be used to compute the FRET.

The energy transfer is highly sensitive on the distance between the donor and acceptor (inversely proportional to the sixth order) and usually lies in the nanometer range. Therefore, many applications of FRET in biology are intramolecular FRET, and exploit the distance dependence by labelling the same molecule at different positions. FRET can be used as a molecular ruler, which measures the distance between two probes located at different positions. A FRET-labeled molecule can also be used as a sensor, if the molecule labels undergoes a conformational change as a function of environmental conditions, such as cellular crowding [18], or pH [61] or the presence of a messenger molecule in the cell [33]. In intermolecular FRET, the fluorescent probes are on different molecules, and when these two labeled molecules form a complex FRET occurs, and the chance of a random FRET event is very small. In such an assay, the FRET is a measure of the interaction between two fluorophores *in vivo*. This way, FRET measurements can determine how much interaction occurs between the two labeled molecules, and also how these interactions are spatially distributed within the cell.

The fluorescent probe can be either a small (synthetic or organic) dye or a fluorescent protein. While dyes are small and usually bright, which makes them good potentially probes, but it is hard to transfer them into the cell. Although labeled proteins have been successfully transferred into the cell by means of electrophoresis (including labeled chemotaxis protein CheY [47]), this (and other transfection techniques) are invasive and the procedure has to be used repeatedly since it is not possible to store the cells. Fusions to fluorescent protein fusions are much less invasive and after the genetic modification has been does not require any special work. A commonly used FRET pair in biology are variants of GFP.

*Sometimes called Fluorescence Resonance Energy Transfer. Since the nonradiative energy transfer does not involve fluorescence this name is technically inaccurate, but also has its uses since there are other possible ways to excite the donor fluorophore such as bioluminsence RET [BRET].

To date, most studies have used YFP and CFP as FRET pairs.

Within the bacterial chemotaxis system there are many pairs of protein that can be measured with FRET [84]. FRET has also been used in showing that the glucose import system interacts with the chemotaxis kinase CheA [135]. In the case of chemoreceptors, FRET with a protein fusion has been used to observe the energy transfer between two identical fluorophores. This does not cause a spectral change in the emitted light, but exploits the fact that while in regular fluorophore excitation and emission the anisotropy of polarized light remains relatively conserved, while the anisotropy after FRET is lost, and (changes in) the average distance between chemoreceptors can be determined [220]. To measure the activity of the chemosensory arrays, an important parameter, perhaps the most obvious choice would be to try fusions to CheA. However, functional CheA fusions have only become available very recently (J.S. Parkinson, personal communication). The most successful application of FRET measures the kinase activity using CheY (fused to YFP) and CheZ (fused to CFP) to measure the kinase activity has been most widely applied on the population level, and has since its introduction this method has lead to over 30 published research articles from six different laboratories.

The interaction between CheY and CheZ essentially measures the dephosphorylation rate between CheY and CheZ (Fig. 1.7a). The CheY phosphorylation/dephosphorylation cycle has a fast typical timescale (100ms), which means that for any times longer than this timescale the CheZ-mediated dephosphorylation rate of CheY equals the CheA-mediated phosphorylation rate of CheY. While the CheZ activity is constant, the activity of CheA is modulated through the interactions within the chemosensory array. When the array is active, the kinase autophosphorylates (slow) and transfers the phosphate group to CheY (fast). If all kinases are active, the phosphorylation rate of CheY is maximal and limited by the amount of kinases, but if only a fraction of the kinases is active the phosphorylation rate (and FRET level) is reduced. Hence FRET can be used to monitor changes in the kinase activity [192], which are in turn induced by changes in ligand and/or methylation.

In population FRET measurements of wildtype *E. coli* cells (in which all CheY and CheZ's are replaced with fluorescent protein fusions) the response of the kinase activity can be measured in response to the addition and removal of attractant and repellent ([192], Fig. 1.7b). Upon the addition of attractant the ratio of emitted light YFP/CFP decreases which is an indication of the FRET level (and consequently the kinase activity). Due to the activity of adaptation enzymes, the kinase activity recovers and upon removal of the attractant stimulus, the cells experience a negative temporal gradient and the activity increases before decreasing fast to the same steady-state level as before the addition of the stimulus. The response to the addition of repellent is qualitatively similar to the removal of attractant and vice versa. In the absence of the adaptation enzymes CheR

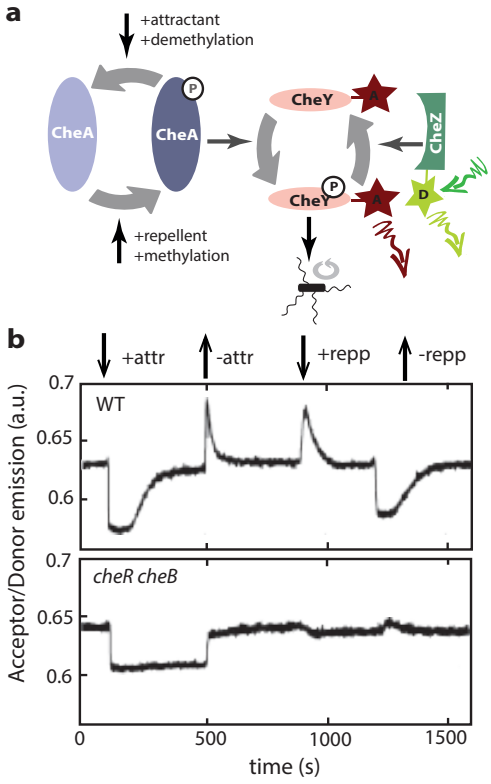

Figure 1.7: FRET assay for measuring intracellular FRET **(a)** . FRET measures the balance of CheY-CheZ phosphorylation-dephosphorylation cycle. Kinase CheA autophosphorylates when active and transfers the phosphate to CheY. Attractant stimulation or demethylation of the chemoreceptors inactivates the kinase, while receptor demethylation and attractant removal restores activity. When phosphorylated, CheY may bind to the flagellar motor base to influence the switching behavior. Meanwhile, CheY is dephosphorylated by CheZ. The CheZ-CheY interaction brings the fluorophores fused to CheZ and CheY in close proximity which enables energy transfer (FRET) between the fluorophores. In case phosphorylation of CheY ceases, FRET decreases. **(b)** Example (population) CheY-CheZ FRET experiment with CFP and YFP as FRET pair of cells responding to the addition and removal of attractant and repellent stimuli. Data from [192]. (top) FRET time series of WT cells (VS104) expressing CheY-YFP and CheZ-CFP responding to the addition and removal of attractant (30 µM MeAsp) and repellent (100 µM $NiCl_2$). (bottom) FRET time series of adaptation-deficient cells (*cheR cheB*,VS149) responding to the addition and removal of attractant (1.5 mM MeAsp) and repellent (100 µM $NiCl_2$).

and CheB, the kinase activity also decreases upon addition of attractant, but no adaptation is observed and the activity level returns to the prestimulus value upon removal of the attractant stimulus. The change of activity of nonadapting cells to the addition and removal of repellent is minimal, indicating that in the absence of any stimulation the kinases are all in the active state and the activity cannot be increased any further by the repellent. The response to the addition and removal of chemoattractant measured in population-averaged FRET experiments can be well understood quantitatively (compare Fig. 1.6 and Fig. 1.7b), but any information about variation across the population or fluctuations within cells is lost. Single-cell FRET using CheZ and CheY has been applied at the single cell level to study the spatial inhomogeneities of the FRET inside *E. coli* [219]. By imaging the fluorescence originating from the acceptor and donor of single cells, it was found that most FRET occurs close to the cell pole in the proximity of the chemosensory array. However, to date no single-cell FRET activity time series (such as shown in Fig. 1.7b) have been measured.

1.4 This Thesis

In this thesis, an investigation of the individuality of bacteria is described, which includes measurements of the variety of signalling parameters between cells in isogenic populations, as well as fluctuations of signalling activity over time within a single cell. Virtually all the experimental data presented in this thesis are measured with a intermolecular FRET technique to measure *in vivo* signaling dynamics. While measurements of signaling dynamics with this technique over extended times was only used for ensemble-averaged experiments, we developed a protocol to enable such measurements of individual bacteria. This protocol, as well as the efforts to optimize it in terms of signal-to-noise ratio, is described in Chapter 2.

In Chapter 3, we describe diversity in signalling parameters within an isogenic population of *E. coli* measured with single-cell FRET. We find that many network parameters of the chemotaxis pathway such as ligand sensing and sensory adaptation are different between cells, which is most likely a reflection of variation in copy numbers of chemotaxis proteins due to stochastic gene expression. We find that the network can either attenuate or create variability in signalling parameters and show experimental evidence for both cases. On the one hand, we show that variability in dose-response parameters due to variable chemoreceptor species ratio is large and the noise levels clearly exceed the lower bounds expected for the expression of high-copy number enzymes. On the other hand, using experiments and a simple quantitative model to show that the CheB phosphorylation feedback loop, with hitherto uncertain function, serves to attenuate the variability in the steady-state activity level of single-cells. Our results show the importance of

the network topology in understanding the relation between molecular noise and phenotypic diversity in signaling and behavior.

Stochastic effects in gene expression have important consequences for cellular physiology and have been widely studied. However, the interaction of the gene products, for example chemotaxis proteins, can also be stochastic, but has been studied much less. As a result of fluctuations in protein-protein interactions, the network activity of a single cell can be variable in time, even in the absence of changes in gene expression. While the existence of such fluctuations were hypothesised based on experiments of bacterial flagellar motor behavior and theoretical predictions, fluctuations were never directly observed at the level of signaling. In Chapter 4 we describe the first direct measurements of temporal variability in the network activity, due to the slow methylation/demethylation activities of the adaptation enzymes CheR and CheB. Unexpectedly, we also found cells lacking adaptation enzymes to exhibit fluctuations in activity levels, which is described in Chapter 5. Interestingly, these fluctuations under some circumstances occurred in the form of discrete two-state switching behavior of chemoreceptor array activity. The observation of two-state switching behavior is remarkable given the size of the chemosensory array ($\sim 10^3$) components and has only been observed in much smaller systems.

The contrast between single-cell and ensemble-averaged experiments is important for all work described in this thesis, but is especially emphasized in Chapter 6. There, we describe two examples of responses, dose response curves and activity decay, in which the same population-averaged response may have completely different underlying single-cell responses. We show the power of single-cell FRET by measuring the response of single cells.

2

Measuring FRET in single bacteria

This chapter describes and compares different measurement protocols for single-cell FRET, designed to measure signaling properties of the *E. coli* chemotaxis network. Starting from established *in vivo* FRET protocols for ensemble-averaged experiments, different fluorescent proteins, expression levels and cell immobilization protocols were compared with the aim of maximizing of signal-to-noise ratio [SNR]. We found considerable differences between different protocols and achieved a maximum average SNR of 10 using a mRFP1-YFP FRET pair. Unexpectedly, we found that cells attached with self-adhesive (“sticky") flagella show substantially increased SNR levels, likely because of enhanced secretion of the anti-sigma factor FlgM, which would lead in turn to upregulation of chemotaxis signaling proteins.

The single-cell FRET measurement and analysis protocol described in this chapter has been used and was included in the following publication: J.M. Keegstra, K. Kamino, F. Anquez, M.D. Lazova, T. Emonet and T.S. Shimizu. “Phenotypic diversity and temporal variability in a bacterial signaling network revealed by single-cell FRET" *eLife* **6**: e27455, 2017 [81]

2.1 Introduction

There are many reasons why single-cell experiments are desired over population-averaged experiments. First, one might be interested in the cell-to-cell variation of particular parameters, such as the signaling parameters studied in this thesis. Another reason is to extract information on the temporal variation of a parameter that is uncorrelated across cells, due to, for example, stochastic molecular processes. The third reason is that whenever cellular responses involve nonlinear input-output relations, the average response of the population may be very different from the typical cellular response, and extracting signaling parameters from population-averaged measurements may under- or over-estimate those parameters.

The bacterial chemotaxis network has been studied both in single-cell experiments as well as in ensemble averaged experiments. The single-cell experiments are generally based on measuring the output of the chemotaxis pathway, namely rotation direction of the flagella. These experiments are generally low throughput and permit either the measurement only of a single cell per experiment (in case of tethered- or trapped-cell experiments, in which cells are attached to a glass surface [185] or immobilized using an optical trap [126]) or short in duration because cells swim outside the field of view (in the case of most tracking experiments, which follow the trajectories of swimming cells [204, 225]). Extracting insights from such experiments often requires aggregating statistics across multiple experiments, which may contribute additional experimental variability. Furthermore, inferring the dynamics of upstream signaling through the flagellar motor is complicated by two problems. Due to the highly random dynamics of the flagellar motor (a stochastic two-state switch [8]) and recently discovered sensory adaptation at the motor level [237], resolving the upstream signaling dynamics requires far more statistics (to average over the switching noise of the motor) and additional control experiments (to rule out or correct for effects of motor adaptation). FRET microscopy has been very useful in studying the intracellular signal processing of the chemotaxis pathway. However, previously reported FRET measurements of signaling dynamics involved integrating fluorescence emitted by hundreds of cells, and effect of fluctuations and cell-to-cell variation were lost. Hence we aimed to extend *in vivo* FRET such that we can measure signaling dynamics of many single cells simultaneously, over durations long enough to extract a variety of signaling parameters.

FRET has been most frequently applied to probe the interaction between the response regulator CheY and phosphatase CheZ, fused to acceptor and donor fluorescent proteins, respectively [192]. This FRET pair has been instrumental in characterizing input-output relations, or transfer functions, of chemotaxis signaling in population averaged experiments [183, 193]. In typical population FRET experiments, the fluorescent excitation is attenuated to a weak level, to minimize bleaching and phototoxicity, integrating the emission across hundreds

of cells attenuates the relative magnitude of photon shot noise to yield a good signal-to-noise ratio [SNR] over experimental durations of more than an hour [96]. However, obtaining FRET signals that exceed noise levels from single cells over extended times is much more challenging, because FRET signals are inherently weak (at most 5-20 % of the total emission). While the instantaneous SNR can easily be enhanced by irradiating at stronger excitation light intensities, this also enhances bleaching of the FRET fluorophores and phototoxicity, which will limit the duration of the experiment. Hence the only single-cell application of CheY-CheZ FRET to date [219], provided insights regarding spatial heterogeneities of signaling activity within the cell, but these experiments were very limited in duration. Hence improving the SNR for *in vivo* FRET measurement of signaling dynamics over extended times demands further optimizations beyond increasing light levels, and we have investigated the influence of several aspects of the measurement protocol to this end.

2.2 Developing a protocol for single-cell FRET over extended times

2.2.1 General FRET protocol description

Föster Resonance Energy Transfer [FRET] microscopy was performed as previously reported by Sourjik, Vaknin and collegues [190, 219], observing the ratiometric changes in fluorescent emission between two fluorophores fused to CheY and CheZ. The FRET signal is proportional to the activity of the chemosensory arrays and the change in activity can be monitored during addition and removal of chemoattacrants ([192], Fig. 2.1a).

The experimental protocol consists of several steps (Fig. 2.1b). In brief: cells are grown to mid-exponential phase and then placed in a medium in which growth and protein expression are halted. Cells are immobilized on a coverslip and placed under a microscope to obtain fluorescent images. The images are analyzed offline to obtain single-cell fluorescent time series, out of which the FRET timeseries are computed. The details of the experimental protocol shown in separate text boxes in this chapter and in the subsequent sections, we describe our efforts in developing and optimizing the protocol starting from the established protocol for population FRET [192].

To ensure that meaningful quantitative comparisons could be made with population-level results, of which there is a large body of previously published data [58, 96, 140, 146, 183, 193], cell growth was performed as described previously (Cell Growth and Harvesting Protocol Box [192]). A biological replicate or independent FRET experiment was defined as a measurement from separately grown cultures, each grown on a different day. Day-to-day variation in such FRET

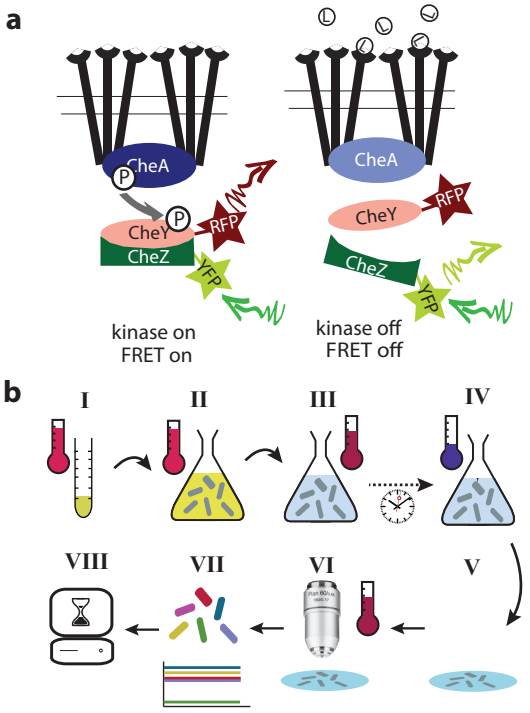

Figure 2.1: Single-cell FRET assay and workflow. **(a)** Schematic of CheY-CheZ FRET assay. In absence of ligand stimuli, receptors are activating CheA. When active, CheA phosphorylates CheY, increasing interaction between CheY and phosphatase CheZ and thereby increasing FRET through the labeled fluorophores. Ligand-receptor binding shuts down the kinase, which ceases phosphate transfer and FRET levels decrease. **(b)** . FRET experiment workflow. (I) From saturated culture grown overnight in rich medium (TB), (II) cells are inoculated 1/100 in TB at 33.5C and harvested in mid-exponential phase (OD ≈ 0.45). (III) In some cases cells are left at room temperature to allow for acceptor maturation, before (IV) storing the cells at 4C. (V) The cells are immobilized on a coverslip and placed in a flow cell for (VI) microscopy measurement at room temperature during which motility buffer (supplemented with attractant) is flushed through (VII) The resulting fluorescent images are segmented and corrected for bleaching. (VIII) Fluorescent time series are further analyzed using scripts.

experiments may yield differences that arise from subtle differences in growth [58] and hence properly controlling each step of this protocol, in particular the harvesting OD, is important for reducing day-to-day variability [190].

I.-IV. Cell growth and harvesting protocol
Cells were grown to OD=0.45-0.5 in 10 mL Tryptone Broth (TB) in 100 mL culture flasks placed in a rotary shaker incubator (33.5 C, 275 rpm) from a saturated overnight culture (2 mL TB in Falcon tubes, 275 rpm) made from a freezer stock at 30C, both with 100 μg/mL ampicillin and 34 μg/mL chloramphenicol and appropriate inducers in the day culture only. For the FRET experiments we used Motility Media (MotM, 10 mM potassium phosphate, 0.1 mM EDTA, 1 μM L?methionine, 10 mM lactic acid, pH 7 [181]), in which cells do not grow and protein expression is absent due to auxotrophic property of parent strain RP437. Cells were washed in 50 mL MotM, and then stored at 4C 0.5-6 h before experiment. In the dose-response experiments (chapters 3 and 6) and the temporal fluctuation measurements (chapters 4 and 5), cells were stored after harvesting for one to three hours at room temperature to allow for further red fluorescence maturation.

2.2.2 Selecting a FRET pair with superior signal-to-noise ratio

In our FRET experiments, the ratio of fluorescent emission of both acceptor (A) and donor (D) fluorophores are recorded and the FRET can be computed from their ratio (§2.2.5). As a figure of merit to compare different protocols we use the signal-to-noise ratio [SNR] of the FRET experiment (Fig. 2.2a). This is defined as the maximal change in acceptor-to-donor ratio ($R \equiv A/D$) due to FRET ($\Delta R_{\max}$) compared to the standard deviation of the fluctuations in this ratio signal (dR):

$$\mathrm{SNR} = \frac{\Delta R_{\max}}{dR} \tag{2.1}$$

The FRET signal is in many cases proportional to changes in the ratio R (as discussed in a more complete analysis below, §2.2.5). We measure $\Delta R_{\max}$ by stimulating with a saturating stimulus, which has been shown using acceptor photobleaching to decimate the FRET signal [192] and consequently R decreases to R_0, the A/D ratio in the absence of FRET. For experimental convenience in optimizing the FRET protocol, we test the FRET response in cells in which the sensory adaptation is disabled. Such cells have a steady-state activity level that is maximal when no ligand stimulus is applied, ensuring that $\Delta R_{\max}$ yields the maximum possible signal. Since the amount of light collected in FRET experiments is generally small, we assume that the noise dR is dominated by shot noise in the acceptor and donor fluorescence emission (evidence of this is

provided below, Fig. 2.5) and hence fluctuations about the baseline level of R are approximated well as temporally uncorrelated white noise (In chapter 4, it is shown that for non-adapting (CheRB-) cells the power spectrum is indeed approximately flat).

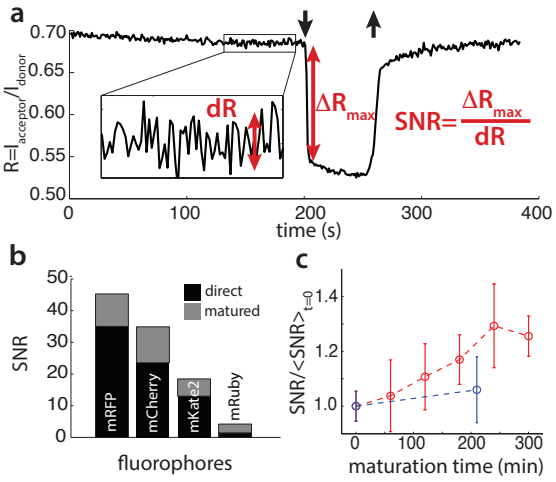

Figure 2.2: Comparing different FRET acceptors. **(a)** Population-averaged FRET experiment with *CheRB-* cells. The ratio R of the acceptor over donor emission is monitored when adding and removing (black arrows) a 500 µM L-serine stimulus. Signal-to-noise ratio is defined as the change in ratio upon stimulation (ΔR_{max}) over the baseline fluctuations in R in the absence of stimulation (dR). **(b)** Comparison of signal-to-noise ratio for different acceptor fluorophores. **(c)** Effect of maturation time (protocol step III) on SNR for maturation of mRFP at room temperature (red) and maturation at 4C (blue) with YFP as donor. Both curves are normalized to the SNR at zero maturation time. Error bars represent s.e.m. with at least 3 independent experiments per condition.

Arguably the most important choice in any FRET assay is the pair of fluorophore labels used as FRET donor and acceptor. Here, we describe how we expect the SNR of the experiment to depend on various fluorophore parameters. If the noise dR originates from low light levels, brighter fluorophores (defined as the product of the quantum yield Q and extinction coefficient ϵ) will decrease the noise at the same excitation energy. To understand how the FRET ratio signal ΔR depends on the fluorophore properties, we consider the FRET efficiency (E_{FRET}) between a donor and acceptor at radius r with Förster Radius R_f.

$$E_{\mathrm{FRET}} = \frac{1}{1 + (r/R_f)^6} \tag{2.2}$$

When CheY and CheZ bind they form a complex and bring the two fluorophores at an average distance $r = r_{\text{bind}}$. This distance is not known precisely, but is typically in the nanometer range [190]. If we assume that the choice of fluorophores do not appreciably affect r_{bind}, one way to improve the FRET signal is to try to increase the Förster radius R_f. This constant depends on the parameters of the donor and acceptor fluorophores and can be described as [94]

$$R_f = [q\kappa^2 Q_D n^{-4} J(\lambda)]^{1/6} \tag{2.3}$$

with q a constant prefactor and n the refractive index of the medium. The function $J(\lambda) = \int F_D(\lambda)\epsilon_A(\lambda)\lambda^4 d\lambda$ depends on the spectral overlap between the normalized donor emission spectrum $F_D(\lambda)$ and acceptor excitation spectrum $\epsilon_A(\lambda)$. Q_D represent the quantum efficiency of the donor. The orientation-dependent factor κ between the two fluorophores, is like the distance r_{bind} not known a priori but we assume the different fluorophores have the same angle distributions (for a freely orienting donor and acceptor this term equals 2/3, but we note that as part of a binding complex the fluorophores likely will not be able to freely rotate). From the expression for the Förster radius we see that a theoretically good FRET pair has a large spectral overlap with high acceptor extinction coefficient and a high donor quantum yield. If the FRET donor and acceptor fluorophores are fused to different molecules, the complex formed between those molecules should bring the fluorophores into close proximity and ideally also at a favorable angle.

Table 2.1: List of potential FRET donors with properties obtained from Fluorescent Protein database (http://www.fpvis.org/FP.html). $\lambda_{ex(em)}$: optimal excitation (emission) wavelength in nm. τ_B: bleaching timescale. $\epsilon_A^{\max}$: Extinction coefficient (mM cm^{-1}). Q_D: Quantum efficiency. τ_M: maturation timescale at 37C. N.D. : not determined.

Protein	λ_{ex}	λ_{em}	$\epsilon_D^{\max}$	Q_D	τ_B(s)	τ_M(m)	Source
mNeonGreen	506	517	116	0.80	158	10	[175]
Clover	505	515	111	0.76	50	30	[95]
YPet	517	530	104	0.77	60	10	[137]
YFP	513	527	83	0.61	60	9	[128]

The established chemotaxis FRET pair of CheZ-CFP and CheY-YFP may seem like a natural starting point, since they have been used not only in many population FRET experiments [140, 146, 192, 193], but also in a pioneering single-cell FRET study [219]. However, the short-wavelength (near UV) irradiation required for exciting the donor CFP of this FRET pair is phototoxic to *E. coli* and induce a repellent chemotactic response, so is not ideal for extended measurements with single-cell FRET, which demands high excitation intensities to overcome proton

shot noise. Hence we examined alternative possible FRET pairs, with an excitation wavelength that is longer than 500 nm. There exist many such protein candidates (reviewed in refs. [40, 176]) of which some promising donor candidates were identified (Table 2.1). Preliminary tests with a Clover/mRuby 2 FRET pair yielded a very low SNR, hence we began our tests with YFP fusion to CheZ, since it differs by only a single point mutation from the CheZ-CFP fusion successfully employed in the established CFP/YFP FRET pair. We compared the properties of potential acceptor molecules which could operate with YFP as a donor. Red fluorescent proteins are generally not as bright as those in the green/yellow part of the spectrum, and are often not monomeric. We selected four different monomeric red fluorophores: mRFP1, mCherry, mKate2 and mRuby 2, shown in Table 2.2, to be tested experimentally.

Table 2.2: List of potential FRET acceptors with properties obtained from Fluorescent Protein database (http://www.fpvis.org/FP.html). $\lambda_{ex/em}$: optimal excitation (emission) wavelength in nm. τ_B: bleaching timescale. $\epsilon_A^{\max}$: Extinction coefficient (mM cm^{-1}). Q_A: Quantum efficiency. τ_M: maturation timescale at 37C. $J(\lambda)$: Spectral overlap (10^{10} nm^4 M^{-1} cm^{-1})). N.D. : not determined.

Protein	λ_{ex}	λ_{em}	$\epsilon_A^{\max}$	Q_A	τ_B (s)	τ_M(min)	$J(\lambda)$	Source
mRuby2	559	600	113	0.38	123	150	520	[95]
mCherry	587	610	72	0.22	96	40	288	[174]
mKate2	588	633	62	0.40	84	20	211	[178]
mRFP1	584	607	42	0.27	N.D.	60	176	[28]

We compared different constructs and sample preparation protocols on SNR, quantified by population-level FRET experiments that measure the response of a CheRB- strain (VS149). Cells were immobilized on a coverslip and the fluorescent emission was monitored while adding and removing a 500 µM L-serine stimulus (which saturates the response [193]). We computed the SNR from the magnitude of the response to the stimulus ($\Delta R_{\max}$) and the standard deviation of the baseline (dR) over a 25s time window before the stimulus (Fig. 2.2a). For the expression of the FRET protein fusions we used a plasmid-based expression system (a list of plasmids is shown in Table 2.4) with an inducible promotor. Surprisingly, we found that the fluorophore mRFP1 performed best (Fig. 2.2b) while its expected FRET efficiency, which should be proportional to $J(\lambda)$ assuming identical κ and r_{bind} for all four FRET pairs, was the lowests (Table 2.2). Red fluorescent proteins generally require additional time after synthesis to become fluorescent, through a set of chemical reactions collectively referred to as maturation [176]. The presence of unmatured donor or acceptor fluorophores decreases the FRET amplitude (and hence SNR) because they decrease the fraction of the bound fusion protein pairs

that can undergo FRET. We compared the increase in FRET signal amplitude after incubating the cells in motility buffer, in which no new fluorescent proteins are produced, up to ~5 hours. When incubated at room temperature, the cells demonstrated an increased SNR, whereas the increase in SNR was much smaller for cells stored at 4C. For mRFP1, room-temperature incubation increased the SNR with ≈ 25 % (Fig. 2.2c). The other tested FRET pairs demonstrated also an increased FRET response amplitudes after maturation, but this did not change the ranking of the acceptors, and therefore we decided to continue with mRFP1 as the acceptor fluorophore for our single-cell FRET experiments.

Having selected a donor and acceptor fluorophore pair, we checked if their fusions to CheY and CheZ could support normal function in chemotactic signalling. A robust way of testing chemotaxis performance provided by the soft agar motility plate assay, in which the growth of a colony of bacteria depletes resources and induces a gradient of nutrients. The cells sense this gradient, and their run-and-tumble random walk becomes biased to climb the gradient, leading to chemotactic migration outward from the point of inoculation. In such an assay, we found that in a strain in which the FRET pair fusions are expressed from two different plasmids, chemotactic migration rates very close to that of the wild-type level could be achieved (Fig. 2.3), while in a tandem construct, both fusions are expressed from the same mRNA transcript from a single plasmid, the migration efficiency was less (Fig. 2.3b). Because the expression levels in a two-plasmid expression level can be tuned separately, we reasoned that the difference in chemotactic performance was due to a difference in the expression level ratio between CheY and CheZ. Because CheZ catalyzes the dephosphorylation of CheY-P, the CheY/CheZ ratio is expected to influence the intracellular CheY-P concentration, which in turn governs the biased random walk by bacteria in the soft agar. Based on comparisons of fluorescence intensity levels between these strains with separate and tandem expression, we estimated that the CheZ/CheY expression was greater by five fold in the tandem expression strain.

While the expression level ratio in tandem constructs is not as easily modified compared to expression from two different plasmids, a possibility is to up- or down regulate expression levels by increasing or decreasing the non-coding sequence to which the ribosome binds. Using an online ribosome binding site [RBS] calculator [163, 164], we constructed two tandem constructs with modified RBS, one in which the efficiency of the ribosome was designed to be down-regulated five fold, and one in which the CheY expression was up-regulated five fold. Also, in both constructs a A206K mutation was made in the *yfp* allele to avoid reported dimerization of the YFP fluorophores. These RBS-modified constructs performed better on soft agar compared to a tandem construct without modified RBS's (Fig. 2.3b). Next, we compared the FRET response of the three constructs. We found that all three strains behaved similarly in terms of signal-to-noise (Fig. 2.3c).

Our initial FRET studies were performed with the pSJAB12 plasmid. Sub-

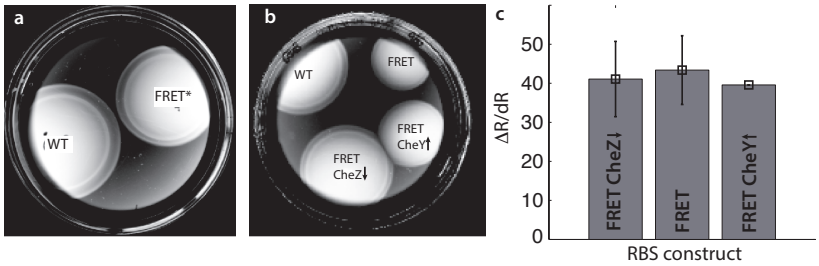

Figure 2.3: Influence of FRET fluorophore expression ratio on chemotactic performance and FRET signal **(a)** . Motility in soft-agar of WT (RP437) versus FRET strain (*cheYZ*, VS104) with CheZ-YFP and CheY-mRFP1 expressed from two different plasmids (pVS52/149) induced with 0.01 % arabinose and 50 μM IPTG. **(b)** Motility in soft-agar of WT (RP437) versus FRET strains (*cheYZ*,VS104) with CheZ-YFP and CheY-mRFP1 expressed in tandem without RBS modification (pSJAB12), with increased CheY RBS efficiency (pSJAB109) and decreased CheZ RBS efficiency (pSJAB106), all induced with 50 μM IPTG. The wildtype strain carries two empty plasmids. Soft-agar plates (0.26 % agar in TB) were supplemented with same antibiotics concentrations as used in flask cultures for FRET experiments. **(c)** SNR obtained from FRET experiments with the strains used in panel (b). Error bars are s.d. of at least 2 independent experiments.

sequent studies used pSJAB106 because of its good performance on soft-agar plates and enforced monomerity in YFP. However, we note that lack of chemotactic functionality of FRET pair fusions is certainly not direct evidence for a poor FRET pair. The FRET pair measures only the upstream signaling activity in the chemoreceptor arrays, and improper chemotaxis may result from many different defects in downstream processes. However, proper chemotaxis of the FRET fusions shows that the FRET pair does not negatively interfere with the chemoreceptor arrays. Also, it opens the opportunity to study signaling properties (with FRET) and swimming behaviour (using a tracking method) in the same strain, and perhaps even the same cells.

2.2.3 From population-averaged to single-cell fluorescence intensity time series

We have described how we selected a FRET pair and expression system to be used in our single-cell FRET studies, but used population FRET in comparing the SNR. In a population FRET experiment the fluorescent emission of both acceptor and donor fluorophores are collected from a dense layer of cells attached to a coverslip, so that both donor and acceptor signal levels are effectively integrated over $\sim 10^3$ cells. To obtain the FRET signal from individual cells, single-cell fluorescence

time series need to be constructed from microscopy camera images. To be able to resolve single-cells, the density of cells needs to be greatly reduced. As described below, there are several ways to immobilize the cells on a coverslip for imaging within a flow cell to obtain sparse attachment (Cell Attachment Protocol Box) and we compare three of these attachment methods below (§2.2.4). Fluorescent images were recorded by an epi-fluorescent microscope and the emission from donor and acceptor are split by a dichroic mirror and projected side-by-side on a single camera chip (Fig. 2.4a-b, Microscopy Protocol Box). We changed the continuous illumination (used in population FRET) to a stroboscopic illumination protocol, in which the sample is illuminated for a short time (usually on the order of 10 ms) with high intensity (approximately 500 fold more intense than population FRET illumination) at regular intervals (0.2-1 Hz). The total energy of light the cells experience per unit time (exposure time times intensity) is usually less than five fold larger than the energy experienced in a typical population FRET experiment. After image acquisition, we use an offline image segmentation protocol to find the cells (Image Analysis Protocol Box) and extract the single cell fluorescence intensities for each cell in each frame (Fig. 2.4c).

V. Cell attachment protocols. Cells were attaced to ethanol cleaned 12 mm round coverslips (BioWorld, No. 1.5) using one of the following methods:
Poly-L-Lysine attachment is performed as described previously [190]. 30-50 μL of PLL 0.1 % (Sigma) is applied to a coverslip for 15-30 minutes, washed twice with MotM and then the cells are applied (OD 0.05-0.2) and allowed to attach for up to 15 minutes.
Self-adhesive (sticky) flagella. The sticky flagella mutant (FliC*) was expressed from the native chromosomal position of FliC or a pKG116 plasmid induced with 2 μM Sodium Salicylate (NaSal).10-20 μL of cells (OD 0.4-0.6) were applied at the coverslip and allowed to attach for 15 minutes.
Anti-FliC antibody Attachment is performed as described previously [190]. Antibodies were column purified (Using Protein A sepharose beads, Amersham Biosciences) from rabbit blood serum and pre-absorbed to FliC- cells (HCB137, gifts from Howard Berg). After dialysis in Motility buffer overnight using 10kDa membrane cassettes (Thermo Scientific), the cells were alequotted in 10 μL samples with an approximate final concentration of 0.1 mg/mL of antibody and stored at -80 C. The entire purification process takes place at 4 C. For each experiment, 10 μL of cells (OD 0.4) were applied to the coverslip and 1 μL of antibody was diluted five fold and applied to the cell suspension.

Single-cell fluorescence intensities showed a decay over time (Fig. 2.4c), which is usually interpreted as irreversible bleaching of fluorophores. To quantitatively compare the FRET signal over time, calculated from those fluorescent time series, the decay needs to be corrected. While the underlying photochemistry is not known precisely and might be very complex involving

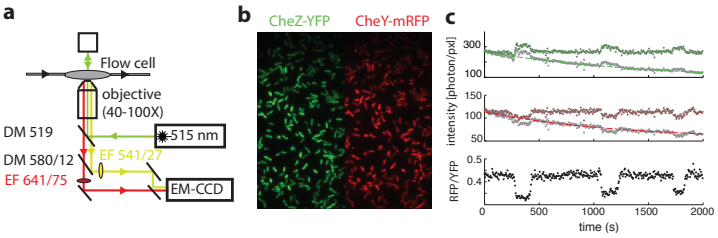

Figure 2.4: Single-cell FRET imaging and segmentation. **(a)** Schematic depiction of optical path to measure FRET with mRFP1 and YFP. **(b)** False-color images of donor (CheZ-YFP) and acceptor (CheY-mRFP1) fluorescence, channels projected on the same EM-CCD camera chip **(b)** Example time series fluorescence from a single cell (CheRB-,VS149/pVS149/52). The corrected data (colored) is shown together with the raw data (grey), with a fit to the raw data of a single exponential function with offset overlaid for donor (top, green) and acceptor channel (middle, red). From the corrected fluorescence intensities the ratio RFP/YFP is calculated (bottom).

transitions between potentially many microscopic fluorophore states [119], we approach the correction of the decay phenomenologically and find a function that describes the decay well and use this function to correct for the decay by division. Depending on the length of the time series, a linear function with offset (for short experiments), single exponential with offset (intermediate duration) or double exponential function without offset (long experiments) are used.

VI. Microscopy Protocol.
Fluorescent images of the cells were obtained with a magnification of 40-100x (Nikon instruments). For excitation of YFP, we either used 514 nm laser excitation set to 30 mW for 2 ms or an LED system (CoolLED, UK) with an approximate exposure time of 40 ms to approximate the same illumination intensity per frame. The sample was illuminated stroboscopically with a frequency between 1 and 0.2 Hz. RPF excitation was performed by 2ms exposure of 60 mW 568 nm laser or equivalent with LED to measure acceptor levels independently from FRET. Excitation light was sent through a 519 nm dichroic mirror (Semrock, USA). Epifluorescent emission was led into an Optosplit (Cairn Research, UK) with a second dichroic mirror (580 nm) and two emission filters (527/42 nm and 641/75 nm, Semrock, USA) to project the RFP and YFP emission side by side on an EM-CCD (Princeton Instruments, USA) with multiplication gain 100. All devices were controlled through custom-written software.

In analogy to population FRET, we computed the intermediate ratio $R_i \equiv A_{0,i}/D_{0,i}$ for each cell i, and subtracted $R_{0,i}$ to align the zero offset of all time

series (Fig. 2.5a). What is clear from the single-cell series of R_i is that, unlike a population FRET experiment, there is not a single SNR per experiment, but each cell has a SNR_i determined by the noise level dR_i, and response ΔR_i. What is clear from the ensemble of single-cell time series R_i(t) is that, by contrast to population FRET experiments, there is not a single SNR per experiment, but each cell has its own SNR value, determined by the noise level dR_i and full-scale response ΔR_i. Strikingly, some cells have quite SNR while there are also many cells in which the signal barely exceeds the noise floor (Fig. 2.5a). Hence a goal for optimizing FRET at the single-cell level is to not only aim for a high average SNR, ⟨SNR⟩, but also a low fraction of cells in which the signal is drowned in the noise. The noise level dR/R_0 clearly decreased with increasing donor emission intensity measured at the onset of the experiment (D_0, Fig. 2.5b) and we observed that the noise in the ratio scales approximately linearly with $1/\sqrt{D_0}$ (Fig. 2.5b, inset), consistent with our assumption that the experimental noise is dominated by shot noise.

VII. Image Analysis Protocol.
Single cells were selected by image segmentation on the donor emission with appropriate filter steps to remove clusters of cells or cells improperly attached to the coverslip. At the position of each cell a rectangular ROI is defined in which all fluorescence intensity is integrated. For experiments in which the concentration of donor molecules may influence the FRET signal, the experiments on the CheB mutants, segmentation was done separately for each frame to determine the cell shape and then linking these segmented images with a tracking algorithm [42], afterwards, fluorescence intensities are normalized for the cell size (mask surface area) in segmentation and cells with low acceptor intensities were excluded from the analysis. The ROI for the donor intensity were subsequently used to obtain the acceptor intensity per cell, both in photon-count per pixel. Fluorescence intensities were corrected for bleaching by fitting a linear, single exponential or double exponential function to the fluorescence decay, separately for both donor and acceptor. Cells in which the intensity decay cannot accurately be corrected were excluded from the analysis.

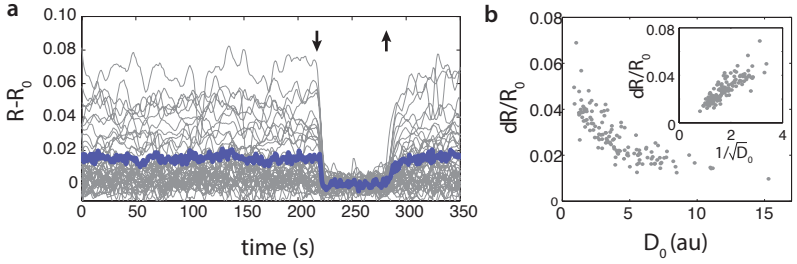

Figure 2.5: Single cell FRET experiment shows variability in steady-state ratio R is limited by shot noise. **(a)** Example single-cell ratiometric FRET timeseries. The change in ratio $R(t) - R_0$, low pas filtered with a moving average filter with a window of 5 seconds, is shown for 45 single cells (grey) together with the population average (blue). **(b)** Fluctuations dR/R_0 in the ratio measured over a 25s window versus the donor fluorescence intensity D_0 for 129 single-cell from three independent FRET experiments. Inset: dR/R_0 against $1/\sqrt{D_0}$ is approximately linear, confirming that short-time fluctuations are dominated by shot noise. Arbitrary units on all axis.

2.2.4 Influence of attachment method on SNR

Having described the main image aquisition and processing pipeline, we now further discuss a way to optimize single-cell FRET time series to obtain a high SNR for as many cells as possible (e.g. ideally a high ⟨SNR⟩ with low variation from cell to cell). As mentioned above, FRET microscopy on chemotactic bacteria requires immobilization of cells to enable stable measure the fluorescence measurements over timescales relevant for signaling, for which different methods exist. Population FRET experiments (and many other bacterial live-cell imaging studies) have used the positively charged polymer Poly-L-Lysine [PLL] to attach cells to a coverslip. However, there is an increasing body of evidence showing that PLL is not ideal for live cell imaging. It has been shown to interfere with growth and cell division by disrupting the Min oscillation system [38], as well as membrane potential [198]. Given that our experiment the cells are neither growing nor dividing, the consequences for our signalling experiments might be not as severe as in studies of cellular growth, but since the mechanisms of the damage are not well understood, we nevertheless cannot exclude the possibility that using PLL will lead to artifacts in signaling measurements. Relevantly, it was found recently that attachment to PLL-treated coverslips reduces the *in vivo* mobility of *E. coli* chemoreceptor arrays (J. Solari, personal communication), indicating that at least some aspects of chemotaxis signaling physiology could be affected by PLL treatment. Could alternative attachment strategies improve the FRET assay? A convenient way to attach motile *E. coli*cells to surfaces is by means of

self-adhesive ('sticky') flagella, which are caused by a genetic modification of the flagellin protein FliC (FliC*) that renders the flagellar filaments adhesive to glass [169]. This attachment method has been applied in flagella rotation experiments in which the cells are tethered to glass by a single flagellum and rotate by means of their flagellar motors [169, 226]. Whereas in a number of bacterial species the flagellar motor is used as a mechanosensor to find and attach to surfaces [11], chemotactic signaling should be unaffected by surface attachment via flagella because in *E. coli* feedback from flagellar motors into the chemotaxis signaling system was found to be absent [181]. We found that in our flow cell with sufficient expression of FliC*, cells attach stably. In some cases the attachment is weak enough that a subset of cells are aligned by the flow in the flow cell, and there is often a fraction of cells (~ 10-20 %) that remains spinning as in a tethered-cell assay, which may complicate fluorescence imaging.

We compared the response of cells attached by PLL with cells expressing sticky FliC filaments from a pKG116 plasmid in *fliC* background. Surprisingly, we saw a large increase in the SNR when attaching with sticky flagella, resulting in a higher average SNR and a much smaller fraction of cells with a low SNR (Fig. 2.6a). We also constructed a strain in which the native chromosomal allele *fliC* is replaced with *fliC**. This yielded a somewhat lower SNR compared to plasmid expression (Fig. 2.6b), but still significantly higher compared to cells attached with PLL (Fig. 2.6c).

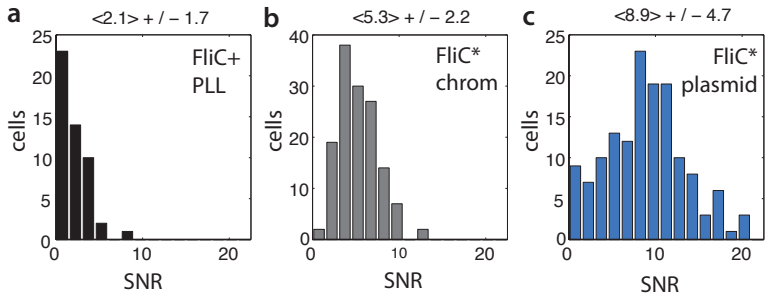

Figure 2.6: Increase of FRET signal-to-noise ratio by means of self-adhesive flagella. The average SNR ± one standard deviation for each condition is shown above each histogram. **(a)** SNR obtained from a single cell FRET experiment on 55 cells with CheRB- background (VS149), attached with PLL. **(b)** SNR obtained from two single cell FRET experiments on in total 129 cells with CheRB- FliC* background (TSS1845), attached with sticky flagella. **(c)** SNR obtained from three single cell FRET experiments on 143 cells with CheRB- FliC* background (VS115/pRZ1), attached with sticky flagella.

What could cause the difference in the FRET SNR between cells attached by PLL and FliC*? The expression level of all motility proteins is determined by

a regulation system consisting of three classes of genes [31, 32]. Activating the master regulator (class I), consisting of the early genes *flhC* and *flhD*, activates middle genes (class II), which together assemble the base of the flagellar motor. The late genes (class III), including all chemotaxis genes as well as *fliC*, are controlled by the RNA polymerase recruiting factor (sigma-factor) σ_{28}. This transcription factor is repressed by the anti-sigma factor *flgM*. When the basal body of the flagellar motor is completed, FlgM is secreted from the cell and hence class III operons start to be expressed upon completion of the flagellar base. Because secretion of FlgM occurs through the assembled flagellar filament, it could be that mutations in FliC affect the secretion of FlgM, thereby up-regulating the chemotaxis proteins. To test this hypothesis, we measured cells attached with PLL in a FliC- background (Fig. 2.7a), in which the secretion of FlgM should by maximized. The results show that *fliC* mutants have increased SNR compared with the same attachment method. While still having a lower signal-to-noise ratio compared to FliC* attachment (Fig. 2.7c), the SNR did increase approximately two fold compared to PLL attachment with FliC+ background (Fig. 2.7a). As an alternative to PLL, we also tested attachment with a different chemical (3-Aminopropyl)triethoxysilane [APTES]) that has been used for live cell imaging studies [161], like PLL adheres cells by creating a charged layer on the glass but is believed to be less disruptive to bacterial physiology. While APTES also showed increased signal-to-noise compared to flagella attachment (Fig. 2.7b), in this particular experiment it did perform better than PLL. We did not pursue the APTES attachment since the attachment was not very strong, but this attachment method has potential to be further optimized.

For some experiments, chromosomal engineering is too costly or too difficult, and plasmid-based expression of FliC* is not possible since the number of plasmids is limited. Another flagellar-based attachment method uses antibodies against the flagellar filament protein FliC. Antibodies adhere well to glass and antibodies that target part of the flagella or hook have been used in tethering experiments [185], as well as a pioneering single-cell FRET imaging study [219]. An advantage of antibodies compared to PLL is that it is much easier to obtain sparse attachment with very few unsegmentable (i.e. clustered) cells compared to PLL attachment, and each individual cell remains attached firmly. We purified polyclonal anti-FliC-antibodies from rabbit serum and used these to attach cells to a coverslip. We attached cells expressing Tsr as the sole chemoreceptor from a plasmid (the other plasmid being required for the FRET pair), with sticky flagella from the chromosome as well as with anti-FliC antibodies (Fig. 2.8). We find that the SNR between the strains is comparable, but slightly higher in the case of FliC* attachment. The response amplitude in these cells can be controlled by changing the induction level of the chemoreceptor expression (Fig. 2.8c). We note that plasmid based expression can also give rise to variability in response amplitudes due to day-to-day variability in expression of chemoreceptor, variability across

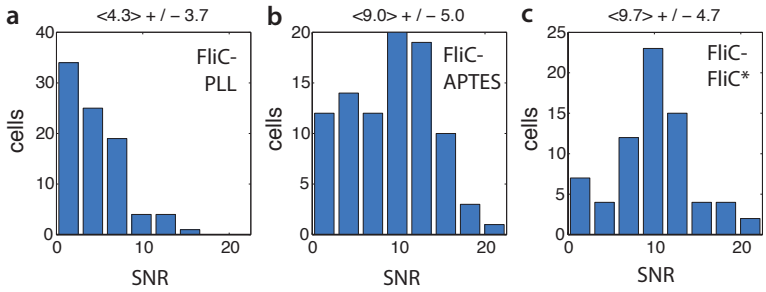

Figure 2.7: Influence of PLL on cellular signal-to-noise ratio in single-cell FRET experiments The average SNR ± one standard deviation for each condition is shown above each histogram.**(a)** SNR obtained from a single cell FRET experiment on 89 cells with CheRB- background (VS115), attached with PLL. **(b)** SNR obtained from a single cell FRET experiment on 94 cells with CheRB- background (VS115), attached with APTES. **(c)** SNR obtained from a single cell FRET experiment on 71 cells with CheRB- FliC* background (VS115), attached with sticky flagella (FliC* from pRZ1).

cells within a population due to plasmid copy number variation.

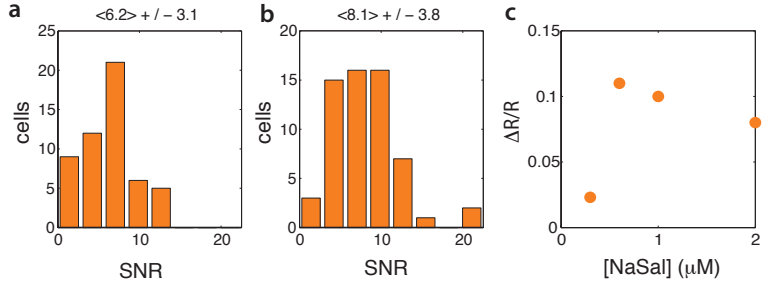

Figure 2.8: Single-cell FRET experiments with cells expressing only one chemoreceptor species (Tsr, induced with 0.6 μM NaSal.). The average SNR ± one standard deviation for each condition is shown above each histogram. **(a)** SNR obtained from a single cell FRET experiment (UU2567/pPA114) on 56 cells attached with anti-FliC antibody. **(b)** SNR obtained from a single cell FRET experiment (UU1964/pPA114) on 60 cells attached with FliC* from the chromosome. **(c)** Influence of receptor expression level on FRET response. Shown is the FRET response obtained from population-averaged FRET (ΔR) as a function of induction level, each point representing a single population FRET experiment.

2.2.5 FRET analysis

As mentioned above, changes in the acceptor-to-donor ratio (ΔR) provides a convenient and robust indicator of changes in FRET. While this is usually a good approximation for the FRET level, a more concrete relation between FRET and the fluorescence intensities can be derived [192]. As mentioned above, we observe changes in the ratio $R = A/D$, in which A and D are the fluorescence intensities of the acceptor and donor. In previous population-averaged FRET experiments the fluorescence changes due to FRET per donor molecule ($\Delta D/D_0$) was identified as a quantity proportional to FRET, and computed from R as [190, 192]:

$$\frac{\Delta D}{D_0} = \frac{\Delta R}{\alpha + R_0 + \Delta R} \tag{2.4}$$

in which R_0 is the ratio in absence of FRET, $\alpha = |\Delta A/\Delta D|$ is a constant that depends on the experimental system (in our case $\alpha = 0.30$) and the change in ratio due to energy transfer ΔR. ΔR and R_0 are readily obtained through observing the ratio just after adding and removing saturated attractant stimuli. This definition of the FRET signal is convenient for population FRET because it is insensitive to the density of attached cells, which can vary considerably from experiment to experiment. However, in single-cell FRET this expression may generate additional variability in FRET due to variable donor levels from cell to cell. Hence it is more convenient to define the FRET levels in terms of the absolute change in donor level ΔD, since this reflects the number of resonance energy transfer pairs

$$\mathrm{FRET}(t) = \Delta D = D_0 \frac{\Delta R}{\alpha + R_0 + \Delta R} \tag{2.5}$$

Note that this expression is invariant for leakage from donor to acceptor. Suppose a fraction of donor signal γ leaks through the donor channel, the contributions of R_0 and α would cancel. Note that this does not hold for leakage from acceptor into the donor channel, but since the acceptor intensities are much weaker compared to the donor channel (factor ~ 10) this contribution is not considered.

We measured the response of non-adapting cells with wildtype chemoreceptor complement (VS149, CheRB-) to multiple identical serine input stimuli and calculated the FRET signal per cell (Fig. 2.9). We observed that the amplitude between cells varies greatly, but within the same cell the variability between the three stimulus sizes is much less, showing that variability of response amplitudes is determined by cellular parameters that do not change in time. To further understand what kind of differences may cause this variability, we need to understand how the FRET signal reveals information about the information transfer in the pathway. Since FRET occurs only when CheY-P and CheZ interact, the FRET level is proportional to the concentration of complex [Yp-Z]. If we assume the CheY-P dephosphorylation by CheZ follows Michaelis-Menten kinetics we

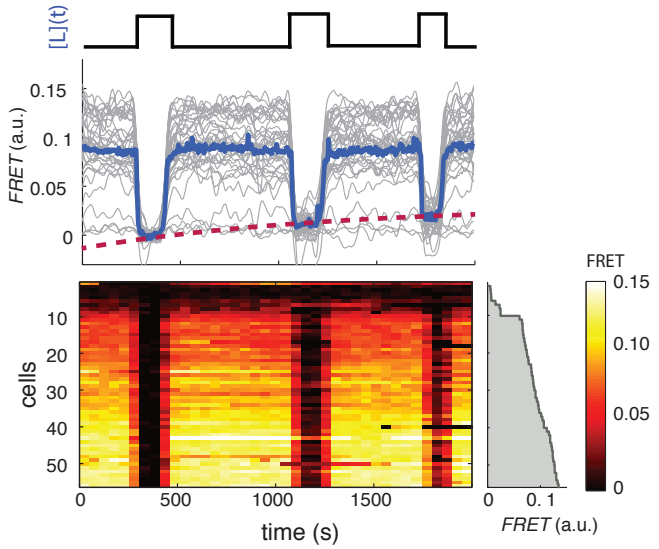

Figure 2.9: Step-response experiment on adaptation-deficient cells (CheRB-FliC+; VS149/pVS149/52). (Top) Ligand time series $[L](t)$ indicates the applied temporal protocol for addition and removal of 500 μM L-Serine. (Middle) FRET responses of 56 cells (gray) with the ensemble-averaged time series (blue) overlaid. Single-cell time series were lowpass filtered with a 25s moving-average filter. (Bottom) Heatmap representation of the FRET response time series, with each row representing a single cell, and successive columns representing the 10s time bins in which the color-indicated average FRET level was computed. Rows were sorted by the steady-state FRET level, defined here as the FRET level just before the first stimulus. The gray curve to the right of the heatmap indicates the steady-state FRET level for each cell

can describe the [Yp-Z] concentration in terms of the activity of the kinase CheA. For this, we assume the system is in steady-state for timescales much larger than CheY phosphorylation-dephosphorylation cycle (≈ 100 ms). In that case, the destruction rate should equal the rate of CheA phosphorylation and hence the FRET signal is proportional to the activity per kinase a and the amount of CheA in the kinase-receptor complex [140, 192]:

$$\text{FRET} \propto [\text{Yp-Z}] = a\frac{k_A}{k_Z}[\text{CheA}] \approx a\frac{k_A}{k_Z}[\text{CheA}]_\text{T} \tag{2.6}$$

This last step is only valid if we further assume CheA autophosphorylation being the rate-limiting step. This is the case only if sufficient amounts of CheZ and CheY present in the cell. When measuring the total FRET amplitude as

a function of donor intensity, which in these measurements is a good proxy for CheZ concentration, we indeed observe an increase in the maximum FRET response for low concentrations of CheZ, while saturating for higher values (Fig. 2.10). In this regime, the FRET level is not dependent on the CheY and CheZ concentrations. When studying cell-to-cell variation in absolute FRET

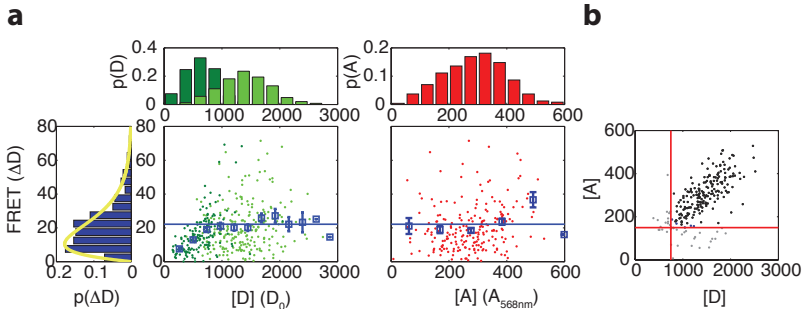

Figure 2.10: Relation between maximum FRET response and expression levels of donor and acceptor fluorophores. **a)** (Left) Scatter plot with donor intensity (D_0, green) versus FRET response to 500 μM MeAsp (ΔD) and (right) acceptor intensity (A, red, measured by direct excitation) with marginal distributions for A, D and ΔD in VS104/pSJAB12. For the donor intensity we measured at low induction (10 µM IPTG, dark green) and high induction (100 µM IPTG, light green). The acceptor intensities were only measured at high induction. In the scatter plots the mean FRET response is plotted with the error bars (blue), the horizontal line indicating the average for the binned data as described in panel (b). The yellow curve is a fit to a gamma distribution with corresponding values and 95% confidence intervals of $k = 2.0 \pm 0.4$ and $\theta = 10.2 \pm 2.5$. All fluorescent intensities are measured in photons/pixel, are divided by cell size (area) and corrected for inhomogeneous illumination. All histograms are normalized to the number of cells. **b)** Gating of the data. Scatter plot of donor intensity versus acceptor intensity. All data with fluorescent intensities (in photons/pixel) lower than D=750 or A=175 are excluded from the analysis since the FRET response depends on donor and acceptor intensity levels below these levels. The distribution of the FRET response (extreme left) is only for the gated data.

levels, e.g. in which the response is not divided by its maximum FRET level, it is essential to operate in the kinase-limited regime since otherwise variation in FRET amplitudes may be caused by variable FRET protein fusion expression. For such experiments, cells that lie outside of the kinase limited regime can be simply excluded by imposing threshold values for the donor and acceptor fluorescent intensities (Fig. 2.10b). Also note that when absolute FRET levels are computed, the fluorophore intensities need to be corrected for inhomogeneous illumination.

Given the relation between donor intensity and FRET response, it might seem the best strategy to measure at the highest concentration of donor possible. However, the SNR should eventually decrease at high donor intensities. This can

be understood as follows: for high D the signal ΔD stays constant (Fig. 2.10) and while the relative noise dD/D_0 decreases with $1/\sqrt{D_0}$, the absolute noise dD still increases with D. Also, analysis of time series becomes challenging if the signal ΔD becomes comparable to decrease in D because of bleaching. Therefore, the ideal donor expression level is not much higher than the value at which ΔD starts to be come independent from D_0.

2.2.6 Influence of fluorophore bleaching on FRET signal

In the experiment with CheRB- cells (Fig 2.12), the responses to the three identical ligand stimuli yield gradually decreases, while the baseline is corrected properly by dividing out the decay in fluorescence (similarly as shown in Fig. 2.4c). Could this gradual increase be explained by bleaching? Using the expression for the FRET response as a function of the fluorescence intensities, we can check how the signal is affected by bleaching:

$$\Delta R = R - R_0 = \frac{\gamma_A A + \gamma_A \gamma_D \Delta A}{\gamma_D D - \gamma_A \gamma_D \Delta D} - \frac{\gamma_A A}{\gamma_D D} \tag{2.7}$$

in which the γ(t) values denote the intact fraction of acceptor and donor fluorophores. Note that the factors ΔA and ΔD scale with both the acceptor and donor γ factors because for for FRET to occur, both the acceptor and donor molecule need to be intact. Normally, the intact fraction of fluorophores are obtained routinely (under the assumption that $D_0 >> \Delta D$) by fitting a function to the total green and red fluorescent intensities, and dividing each channel with this fraction ($D = D^*/\gamma_D$ and $A = A^*/\gamma_A$, with A^* and D^* the measured donor intensity) yields a bleaching correction which corrects the baseline of the ratio. Hence the bleaching correction described above yields

$$\Delta R = \frac{A^* + \gamma_D \Delta A}{D^* - \gamma_A \Delta D} - \frac{A^*}{D^*} \tag{2.8}$$

and we see that although the baseline might be corrected, there is a residual change in FRET that is not corrected for. In the fluorescence time series of individual cells, the response in the acceptor channel clearly decreases over time, but the response in the donor channel does not (Fig. 2.11). This implies that the donor is bleaching, but the acceptor is not. And the decrease in acceptor signal is accurately described by the fraction of intact donor molecules $\gamma_D(t)$ (Fig. 2.11, blue dashed line). If this is correct, this could simplify the expression for ΔR.

But how could the statement that acceptor bleaching is absent be true since the fluorescence in the acceptor channel clearly decays? Here we should take into account that some light in the acceptor channel is due to leakage of donor emission. Based on spectra of YFP and our filter sets this equals approximately

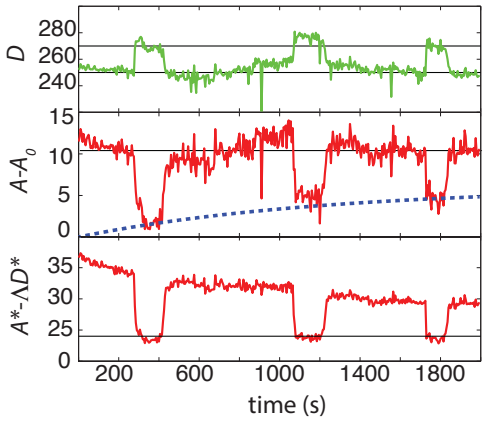

Figure 2.11: Donor bleaching causes decay in FRET level. All intensities are in photons/pixel. Example cell from experiment shown in Fig. 2.9. (Top) Donor fluorescence corrected for bleaching $D*$. Black lines are guide to the eye. (Middle) Acceptor fluorescence corrected for bleaching $A* - A_{max}$. Blue dashed line describes $[1-\gamma_D]A_{max}$. (Bottom) Acceptor fluorescence intensity calculated by correcting for donor channel leakage $A - \Lambda D$, with Λ=0.17, but no correction for bleaching. Black line is guide to the eye.

16 % and we found 15-18 % by measuring fluorescence with a strain that only expresses YFP (data not shown). After subtracting this fraction of the donor signal from the acceptor signal, it is clear that the acceptor intensity relaxes to the same value at each stimulus, but the baseline is indeed decreasing. Hence while the FRET level during ligand stimulation seemed to be *increasing*, it was in fact the steady-state level that was *decreasing*.

An easy way to correct for the effect of decreasing FRET amplitudes, is by describing the change in ratio after the initial bleaching correction is performed (e.g. after dividing out the fluorescence decay obtained through a fit). The ratio should change according to

$$R_{\text{drift}} = \frac{A + [1-\gamma_D(t)]\Delta A_{sat}}{D_0} \tag{2.9}$$

and substitute this for R in equation 2.4. This expression describes the decrease of the FRET response (or the apparent increase of FRET baseline) on the population level quite well (Fig. 2.9, red dashed line). However, while the first bleaching correction is independent of the SNR of each cell, this second correction becomes worse if the change in acceptor intensity ΔA_{sat} on the level of the noise dA and introduces a new experimental noise source. While this bleaching correction can

be applied in some cases and should be a focus for further improvements, we rather chose to work under conditions in which loss of FRET due to bleaching is below 15 %. Note that bleaching rates are fluorophore specific and hence the above assumption of only donor acceptance may not hold when using different measurement conditions.

2.2.7 Extracting parameters of signaling dynamics from FRET timeseries

How can we use FRET time series of single cells to learn about chemotactic signaling? As we have seen, the FRET signal can be used to measure the activity of receptor-kinase complex. In many cases the most relevant parameter is the normalized FRET response. The FRET level reaches maximum if all kinases are active ($a \approx 1$). In case of CheRB+ cells, this is the case when removing a saturating amount of attractant after adaptation [192]. For CheRB- cells the baseline activity is close to 1 [22, 183, 192]. Hence the normalized FRET, $\mathrm{FRET}(t)/\mathrm{FRET}_{\mathrm{max}}$ represents the activity per kinase $a(t)$ and is the relevant parameter for many quantitative models for chemoreceptor activity [213].

$$a(t) = \frac{\mathrm{FRET(t)}}{\mathrm{FRET}_{max}} \tag{2.10}$$

and from $a(t)$ the steady-state activity a_0 can be determined by averaging $a(t)$ over baseline values before adding attractant stimuli.

As an example, we consider a FRET experiment on CheRB+ cells (Fig. 2.12), in which the baseline a_0 is lowered from approximately 1 in CheRB- cells to 0.2-0.3 and the system shows a response to both attractant and repellent stimuli, and after the addition and removal responses a slow recovery of the network activity can be observed. While the population-averaged curve agrees well with previous population-averaged experiments, each cell now shows a different response. From such single-cell time series one can easily obtain the value of steady-state parameters (such as a_0) by averaging over a time window. This works best when comparing FRET signals between short time intervals, such as the addition of ligand. Note that comparing absolute levels at very different parts of the time series (such as the adaptation precision) may cause baseline drift or incomplete bleaching correction to be the dominant source of noise, of which it is much harder to see how this influences the distribution. Measurements of dynamic properties can be performed by ether fitting a function to a segment of the time series or by time averaging and a low-pass filtering protocol. For determining the adaptation time, we chose the latter. Because there is a clear separation of timescales between the experimental noise timescale, set by the acquisition frequency, and dynamic properties can be extracted (Fig. 2.12). However, for such

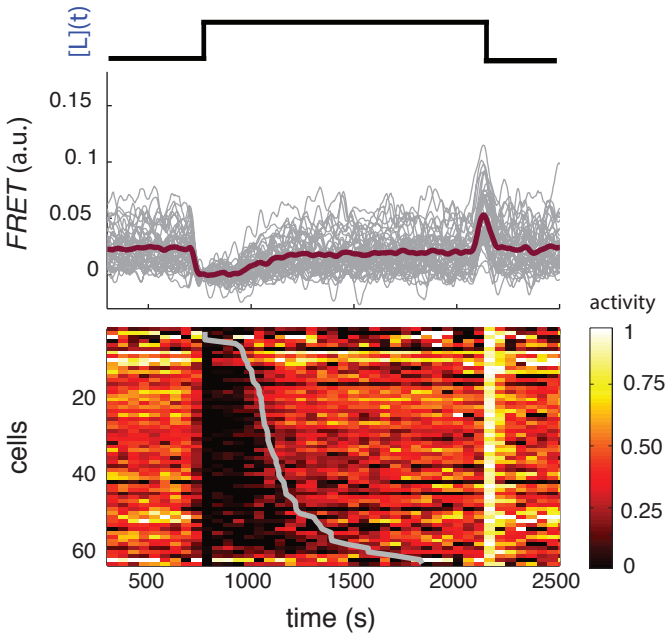

Figure 2.12: Step-response experiment on wildtype cells (CheRB+ FliC+; VS104/pVS149/52) attached with poly-L-lysine. (Top) The ligand time series $[L](t)$ indicates the applied temporal protocol for addition and removal of 500 µM MeAsp. (Middle) FRET response of 61 cells (gray) with the ensemble-averaged time series (dark red) overlaid. Single-cell time series were lowpass filtered with a 25s moving-average filter. (Bottom) Heatmap representation of the normalized FRET response time series, with each row representing a single cell, and successive columns representing the 10s time bins in which the color-indicated activity was computed from the FRET time series. Activity was computed by normalizing FRET to the total response amplitude (Max-Min for each time series). Rows are sorted by the corresponding cell's recovery time (light blue curve), defined as the time at which the activity recovered to 50 % of the pre-stimulus activity.

a non-linear process one needs to carefully consider how the fitting algorithm performs under noisy conditions.

To verify that observed distributions in signaling parameters do reflect biological variation between cells and do not originate from experimental error, it is good practice to check if the extracted signaling parameters do correlate with experimental parameters such as FRET reporter expression levels or light intensity. As an example, we investigated parameters of the adaptation system extracted from a FRET experiment on CheRB+ cells (In an experiment similar to the one shown in Fig. 2.12, but attached with self-adhesive flagella and shown in the following chapter, Fig. 3.1) and their correlation with donor intensity. Since these signaling parameters could be extracted from the normalized FRET time series (activity units, Eqn. 2.10) the time series were not corrected for inhomogeneous illumination. We found no significant correlations between experimental and signaling parameters (Fig. 2.13).

2.3 Summary

We have developed a FRET protocol that is optimized for single-cell measurements over extended times with high SNR. The phase space of optimization is large and the search described here was by no means exhaustive. We have compared different fluorescent proteins, and found that of the considered candidates YFP and mRFP make the best FRET pair. This is surprising considering this FRET pair is one of the worst as predicted from the fluorophore properties (A decade ago, one review paper even considered mRFP1 to be 'obsolete' [176]). This implies that the distance and/or angle of the two fluorophores while part of the CheY-CheZ complex do differ considerably between the FRET pairs. We cannot exclude that the mRFP1 and YFP FRET pair can be further improved, but unfortunately, there is no good way to predict these quantities *a priori*. One way to change the relative orientation and distance is by changing the linker distance between the acceptor/donor and CheY/CheZ (all experiments described use a 5G linker). Measurements of FRET efficiency in other systems often do not translate easily to other experimental conditions, and many fluorophores have been optimized to work in mammalian cells at 37C. Hence while it is good to stay vigilant for new fluorophore developments, it is also advised to take reported fluorophore parameters with a grain of salt.

We have compared different attachment protocols and found that attachment with self-adhesive flagella performs best in terms of SNR. While the attachment protocol itself is arguably the easiest of the options we have explored and does barely require any laboratory consumables, it requires considerable investment in chromosomal engineering for each strain that needs to be measured, and one may have to use a plasmid for the expression of FliC*. The latter can be challenging

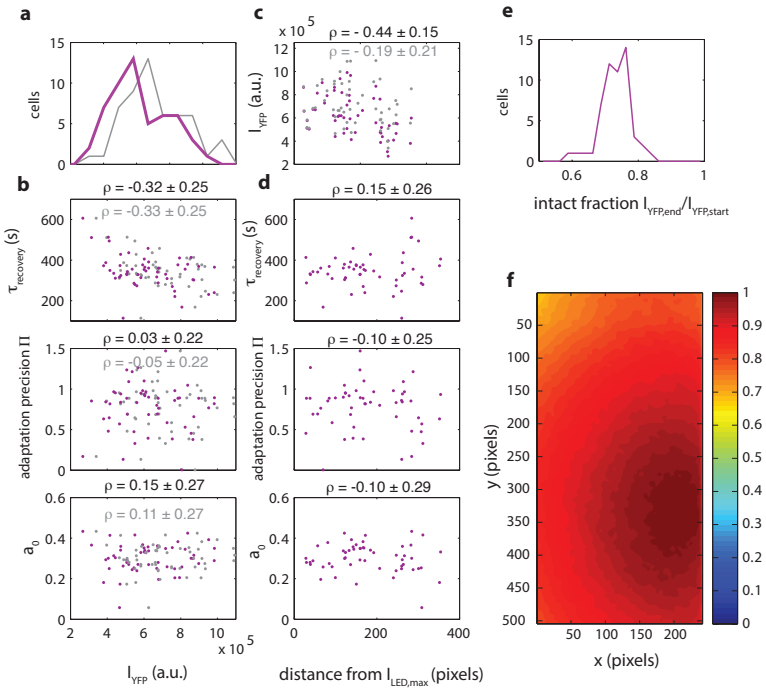

Figure 2.13: Observed diversity in signaling parameters cannot be explained by variation in experimental parameters. **(a)** Histogram of fluorescence intensities of the donor at the start of a FRET experiment as measured (purple, CV =0.38) and corrected for inhomogeneous illumination (grey, CV =0.33). **(b)** Scatter plots of donor intensity versus adaptation timescale (top panel), adaptation precision (middle panel) and steady-state activity (bottom panel). For each scatter, the data points (red) are shown together with the intensities corrected for inhomogeneous illumination (grey). Above each plot the Pearson correlation coefficient is shown with 95 % confidence interval obtained from bootstrap resampling. **(c)** Scatter plot of euclidean distance (in pixels) of each cell to sample position with highest illumination intensity versus the donor intensity. Illumination correction changes a negative dependence of cellular intensity to distance ($\rho = -0.44 \pm 0.15$) to insignificant dependence ($\rho = -0.19 \pm 0.21$). **(d)** Scatter plots of euclidean distance (in pixels) of each cell to sample position with highest illumination intensity versus adaptation timescale (top panel), adaptation precision (middle panel) and steady-state activity (bottom panel). Above each plot the correlation coefficient is shown with 95 % confidence interval obtained by bootstrap resampling. **(e)** Histogram of the intact fraction (1-decay) of donor fluorescence intensity at the end of the FRET experiment. **(f)** Illumination profile measured by illuminating a ≈ 100 µm thick sample with fluorescein.

since cells generally do not support more than two plasmids. Also, the established attachment method of PLL can be used, but the increasing amount of evidence for negative effects on cellular physiology makes that this procedure should be used with caution. A good alternative is the use of anti-FliC antibody, but the disadvantage is that the preparation of them is costly and antibody harvesting in living animals is invasive. The disadvantage is that one cannot measure in FliC- background, which has been shown to be responsible for increased SNR, most likely because of increased secretion of FlgM. This hypothesis could be confirmed by measuring FRET levels in *flgM* background. If correct, it means that measurements with this type of attachment have different protein levels (although the protein stoichiometry is conserved [171]) than RP437. While motor experiments with tethered cells have successfully used sticky flagella attachment methods, one could argue that changed expression levels compared to other attachment methods makes the *fliC** genotype less representative of the wildtype genotype. However, a recent study showed that the *flgM* activity is quite plastic under evolutionary timescales [138] and can change the phenotype within a spectrum ranging from between a strongly motile phenotype at the expense of cell growth, a fast growing phenotypes with less chemotactic ability. While complete deletion of flgM is the most extreme phenotype, it does show that upregulation of all chemotaxis proteins is something cells can do routinely when confronted with an environment that is highly selective on chemotactic properties.

Fluorophore maturation and photostability are two other factors that are useful in assessing a potential FRET pair. As we have seen, a fraction of acceptors at the time of harvesting is not active and, in the case of mRFP1, requires several hours after harvesting to mature. A faster acceptor maturation time would result in more fluorophores available for FRET which will decrease the noise and increase the signal. By excitation light the donor emission also reduces because of bleaching. While the main part of this decay can be corrected by fitting a curve to the baseline, a further decay in FRET is harder to correct because the correction depends on the SNR of cells. This effect can be minimized if the photostability of the donor is improved.

In the following chapters, we describe how single-cell FRET has been used to characterize the chemotaxis pathway. Chapters 3 focusses on cell-to-cell variation in signaling parameters, and reveals that a previously uncharacterized feedback loop serves to attenuate cell-to-cell variability in the steady-state activity levels. While the fluctuations in FRET time series shown in this chapter are dominated by shot noise, it is also possible to study biological temporal fluctuations, as long as the timescale of the noise source is slower than the acquisition frequency and the amplitude is sufficiently high. Examples of such studies are described in chapters 4 and 5. In chapter 6 we study the relation between single-cell and population dose response curves using single-cell FRET, and show that the same population-averaged response function can have very different underlying single-

cell behavior.

Acknowledgements

We thank Yuki Esser and Fotios Avgidis for FRET experiments on maturation time and attachment methods. All cloning activities are performed by Yuki Esser, Simone Boskamp and Zuzana Rychnavska.

2.4 Strains and Plasmids

All strains used are descendants of *E. coli* K-12 HCB33 (RP437) [145]. Growth conditions were kept uniform by transforming all strains with two plasmids. All strains and plasmids are listed in Tables 2.3 and 2.4.

The FRET acceptor-donor pair (CheY-mRFP and CheZ-YFP) is expressed in tandem from a IPTG inducible pTrc99A plasmid: pSJAB12, pSJAB106 or pSJAB109, with respective induction levels of 100 and 50 μM IPTG. The differences between pSJAB12 and pSJAB106/109 are i) the presence of a noncoding spacer in pSJAB106/109 to modify the ribosome binding site of CheZ (pSJAB106) and CheZ (pSJAB109) [164], such that the CheZ/CheY ratio is reduced approximately 3 fold, and ii) a A206K mutation in YFP to enforce monomerity. We have also used pVS52 (CheZ-YFP) and pVS149 (CheY-mRFP1) to express the fusions from separate plasmids with induction levels of 50 uM IPTG and 0.01 % arabinose, respectively. We transformed the FRET plasmids in adaptation-proficient strain (VS104) to yield CheRB+ and adaptation- (VS149) to get CheRB-. For attachment with sticky flagella from pZR1 we used the equivalent strains in *fliC* background (VS115 and TSS58).

Table 2.3: Strains used in this study. All strains are descendants of E. coli K-12 HCB33 (RP437). In all FRET experiments, strains carry two plasmids and confer resistance to chloramphenicol and ampicillin.

Strain	Source	Relevant Genotype	plasmid 1	plasmid 2
VS115	Sourjik	ΔYZ ΔFliC	pSJAB106	pZR1
VS104	[192]	ΔCheYZ	pVS52	pVS149
VS104		ΔCheYZ	pSJAB12	pBAD33
VS104		ΔCheYZ	pSJAB106	pBAD33
TSS58	*this work*	ΔRBYZ ΔFliC	pSJAB106	pZR1
VS149	[193]	ΔRBYZ	pVS52	pVS149
VS149		ΔCheRBYZ	pSJAB12	pBAD33
VS149		ΔCheRBYZ	pSJAB106	pBAD33
VS124	[35]	ΔCheBYZ	pSJAB12	pVS112
VS124		ΔCheBYZ	pSJAB12	pVS97
VS124		ΔCheBYZ	pSJAB12	pVS91
VS148	[193]	ΔRBYZ Δ(Tsr,Tap)	pVS52	pVS149
SB1	[97]	$Tar^{[QQQQ]}$ ΔRBYZ Tsr Tap	pVS52	pVS149
VS179	[181]	ΔBYZ Δ(Tsr,Tap)	pVS52	pVS149
VS140	Sourjik	ΔBYZ Δ(Tsr)	pSJAB106	pVS112
UU2567	[88]	ΔCheRBYZ,ΔMCP†	pSJAB106	pPA114 Tsr
TSS1964	*this work*	ΔCheRBYZ,ΔMCP FliC*	pSJAB106	pPA114 Tsr
TSS1964	*this work*	ΔCheRBYZ,ΔMCP FliC*	pSJAB106	pVS120
UU2614	Parkinson	CheB Δ(4-345)	pTrc99a	pVS91,97,112
UU2933	Parkinson	CheA-V551A in UU2567	pSJAB106	pPA114 Tsr
UU2933		CheW-X3‡ in UU2567	pSJAB106	pPA114 Tsr
TSS744	*this work*	ΔCheRB	pTrc99a	pSJAB37,147-149
TSS1845	*this work*	ΔCheRBYZ FliC*	pSJAB106	pSJAB149

† all five chemoreceptor genes *tar tsr tap trg aer* deleted
*: expresses sticky FliC element [169]
‡: CheW-X3 allele, expresses CheW R117D,E121R,F122S

Table 2.4: Plasmids used in this study.

Name	Product	System	Source
pVS52	CheZ-5G-YFP	pBAD33	[192]
pVS149	CheY-5G-mRFP1	pTrc99a	[192]
pSJAB6	CheY-5G-mCherry	pTrc99a	This work
pSJAB135	CheY-5G-mRuby2	pTrc99a	This work
pSJAB136	CheY-5G-mKate2	pTrc99a	This work
pSJAB12	CheZ-5G-YFP / CheY-5G-mRFP1	PTrc99a	This work
pSJAB106	CheZ-5G-YFP† / CheY-5G-mRFP1	PTrc99a	This work
pSJAB109	CheZ-5G-YFP† / CheY-5G-mRFP1	PTrc99a	This work
pVS91	CheB[1]	pTrc99a	[106]
pVS97	CheB-D56E [2]	pBAD33	[35]
pVS112	CheBc [3]	pBAD33	V. Sourjik
pSJAB 122	CheBc-GS4G-mVenus	pBAD33	This work
pSJAB 123	CheB(D56E)-GS4G-mVenus	pBAD33	This work
pSJAB 124	CheB-GS4G-mVenus	pBAD33	This work
pZR 1	FliC*	pKG116	This work
pPA114 Tsr	Tsr	pPA114	[4]
pPA114 F396Y	Tsr F396Y	pPA114	[4]
pPA114 F396W	Tsr F396W [QEEEE]	pPA114	[4]
PVS120	Tar [QEEE]	pLC113	[193]
pSJAB37	CheR / CheB	pBAD33	This work
pSJAB147	CheR / CheB (native RBS)‡	pBAD33	This work
pSJAB148	CheR / CheB (native RBS)‡	pKG116	This work
pSJAB149	CheR / CheB	pKG116	This work

†: YFP contains A206K mutation to enforce monomerity and includes engineered RBS sequence.
‡: Includes native sequence of 100 bases upstream of CheR
1: expresses WT CheB
2: carries a point mutation D56E in CheB
3: expresses only residues 147-349 of CheB, preceded by a start codon (Met)
*: expresses sticky FliC element [169]

3

Generation and attenuation of phenotypic diversity in bacterial chemotaxis

In this chapter, we present *in vivo* measurements of intracellular signaling dynamics in individual bacteria over extended times using single-cell FRET. These experiments reveal the influence of network design on the distribution of phenotypes of the *Escherichia coli* chemotaxis pathway, a canonical signalling network. In isogenic populations simultaneously experiencing identical stimuli, we found considerable diversity in adaptation times. In mutants deficient in adaptation, strong cell-to-cell variation is observed not only in the steady-state network output, but also in the sensitivity and gain of response to identical ligand stimuli. The pattern of covariation of the latter two parameters can be explained by variation of only a single parameter: the expression-level ratio between the two major chemoreceptors Tar and Tsr. We found, using mutant strains with altered network topologies, that variability in the steady-state network activity is reduced by the phosphorylation feedback loop of the adaptation system mediated by the methylesterase CheB. Without this feedback loop, which is dispensable for precise adaptation, the diversity in the steady-state activity phenotype is strongly augmented and demonstrates likely detrimental bimodality, polarizing the population towards extreme behaviors of smooth swimming and incessant tumbling. These results demonstrate how gene expression variability can influence the design of protein signaling networks.

This chapter is part of the publication: J.M. Keegstra, K. Kamino, F. Anquez, M.D. Lazova, T. Emonet and T.S. Shimizu. “Phenotypic diversity and temporal variability in a bacterial signaling network revealed by single-cell FRET" *eLife* **6**: e27455, 2017 [81]

3.1 Introduction

Cellular physiology is deeply shaped by molecular fluctuations, resulting in phenotypic diversity and temporal variability that can be both detrimental and beneficial [73, 93, 99, 158]. One of the most important and well-studied sources of intracellular fluctuations is stochastic gene expression [53, 55, 156], which can generate substantial cell-to-cell variation in protein levels within isogenic populations under invariant environmental conditions. Such heterogeneity in protein counts are readily measurable by fluorescent-protein reporters [55, 142] , but mechanistically tracing the consequences of such molecular noise to the level of complex cellular phenotypes such as signaling and motility remains a significant challenge, due to the multitude of interactions between gene products. In this chapter, we study how gene expression noise propagates through the protein signaling network.

The chemotaxis network controls the motile behavior of *E. coli*, a run-and-tumble random walk that is biased by the signaling network to achieve net migrations toward favorable directions. The molecular mechanisms underlying this pathway have been studied extensively (for recent reviews, see refs. [37, 144, 213, 224], and §1.2). In brief, transmembrane chemoreceptors bind to ligand molecules, inhibiting the autophosphorylation of a central kinase, CheA. When active, CheA transfers its phosphate to CheY to form CheY-P. Meanwhile, the phosphatase CheZ dephosphorylates CheY-P to limit the signal lifetime. CheY-P binds to a flagellar motor, which in turn increases the chance of the motor to turn clockwise, leading to a tumble. An adaptation module consisting of the enzymes CheR and CheB implements negative integral feedback by tuning the sensitivity of the chemoreceptors via reversible covalent modifications that restore the kinase activity (and CheY-P level).

In bacteria, gene-expression noise tends to manifest itself as stable cell-to-cell differences in phenotypes that persist over the cell's generation time, because typical protein lifetimes are longer than the cell cycle [101]. The architecture of signaling networks can have a profound influence on their sensitivity to such noise-induced differences in protein levels, and it has been shown that the design of the *E. coli* chemotaxis network confers robustness of a number of signaling parameters, such as precision of adaptation, against variability in gene expression [10, 90]. On the other hand, cell-to-cell differences in behavior can also be advantageous for isogenic populations under uncertain and/or time-varying environments, and it has been argued that the manner in which the chemotaxis network filters gene expression noise to shape phenotype distributions could be under selective pressure [65, 225].

While many of the signaling parameters of the system have been characterized successfully by an *in vivo* FRET technique [183, 192, 193], those measurements integrated signals over hundreds of cells and hence differences between cells were

effectively averaged out. By exploring a range of fluorescent proteins as FRET pairs, and improving measurement protocols, we have developed a robust method for FRET measurements of chemotactic signaling dynamics in single bacteria over extended times, which reveal extensive cell-to-cell variation. In a typical experiment, we are able to obtain dozens of (up to ~100) single-cell FRET time series simultaneously, to efficiently collect statistics of such phenotypic diversity.

3.2 Single-cell FRET reveals strong variation in signaling parameters

To measure variability in intracellular signaling, we adapted a FRET assay for chemotaxis widely used for population-level measurements with fluorescent fusions to CheY and its phosphatase CheZ [190, 192]. On timescales longer than the relaxation of CheY's phosphorylation/dephosphorylation cycle, the FRET level reflects the phosphorylation rate of CheY by the CheA kinase, thus providing an efficient *in vivo* measurement of the network activity (see Figs. 1.7 and 2.1). Instead of the conventional CFP/YFP FRET pair we used the fluorophores YFP and mRFP1 to avoid excitation with blue light, which induces considerably stronger photoxicity and also perturbs the chemotaxis system as a repellent stimulus [205, 206, 230]. Fusions of these fluorophores to CheZ and CheY still yield a fully functional phenotype [228], when observing chemotaxis on soft agar (see Fig. 2.3)

For wildtype cells (Fig. 3.1) we found that the ensemble mean of single-cell FRET responses, $\langle \mathrm{FRET} \rangle(t)$, agrees well with previous population-level measurements [192]. Upon prolonged stimulation with a saturating dose of attractant α-methylaspartate (MeAsp), $\langle \mathrm{FRET} \rangle(t)$ rapidly fell to zero before gradually returning to the pre-stimulus level due to adaptation. Upon removal of attractant, $\langle \mathrm{FRET} \rangle(t)$ rapidly increased to a maximum before returning to the pre-stimulus baseline. Single-cell FRET time series, $\mathrm{FRET}_i(t)$, had qualitatively similar profiles, but the kinetics of adaptation and response amplitudes demonstrate differences from cell to cell. For each cell, $\mathrm{FRET}_i(t)$ is limited by the autophosphorylation rate of CheA and hence is proportional to $a_i[\mathrm{CheA}]_{\mathrm{T},i}$ (provided [CheY] and [CheZ] are sufficiently high, see §2.2.5), in which a_i is the activity per kinase ($0 \le a_i \le 1$) and $[\mathrm{CheA}]_{\mathrm{T},i}$ the total concentration of receptor-kinase complex of the i-th cell. The FRET level of each cell is thus bounded at a value $\mathrm{FRET}_{i,\max}$ which occurs when its kinases are fully active ($a_i = 1$), and can be measured by the removal of a sufficiently large stimulus after adaptation (as in the experiment of Fig. 3.1). Hence from $\mathrm{FRET}_i(t)$ the activity per kinase $a_i(t)$ can be readily determined by normalizing each FRET time series by its maximum response $a_i(t) = \mathrm{FRET}_i(t)/\mathrm{FRET}_{i,\max}$ (Fig. 3.1b). The steady-state activity $a_{0,i}$, defined as the time-average of $a_i(t)$ before the addition of attractant,

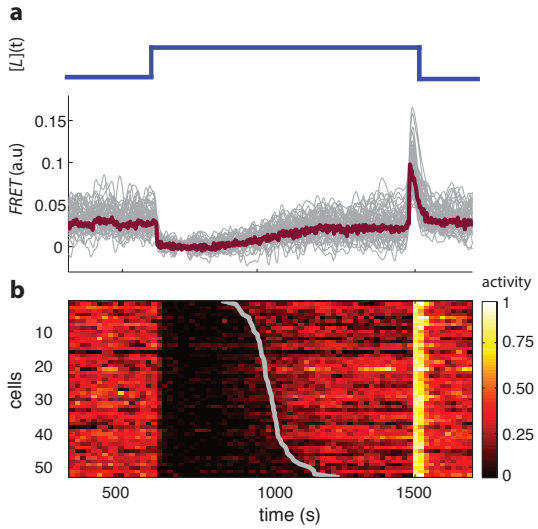

Figure 3.1: Step-response experiment on wildtype cells (CheRB+; VS115) reveals diversity in sensory adaptation. (Top) The ligand time series $[L](t)$ indicates the applied temporal protocol for addition and removal of 500 µM MeAsp. (Bottom) FRET response of 54 cells (grey) with the ensemble-averaged time series (dark red) overlaid from a representative single experiment. Single-cell time series were lowpass filtered with a 14s moving-average filter. **(b)** Heatmap representation of the normalized FRET response time series, with each row representing a single cell, and successive columns representing the 10s time bins in which the color-indicated activity was computed from the FRET time series. Activity was computed by normalizing FRET to the total response amplitude (Max-Min for each time series). Rows are sorted by the corresponding cell's recovery time (grey curve), defined as the time at which the activity recovered to 50 % of the activity level after adaptation (see panel e).

was found to vary from cell-to-cell with a coefficient of variation $CV(a_0) = 0.23$ (Fig. 3.2a). The network activity controls the flagellar motor rotation, and hence this is consistent with the observation that cells in an isogenic population exhibit a broad range of steady-state tumble frequencies [49, 195].

The adaptation precision is defined as its post-adaptational activity level divided by the pre-stimulus level ($\Pi = a_{\text{adapted},i} / a_{0,i}$), hence a precision of 1 refers to perfect adaptation. The adaptation kinetics are quantified by the recovery time τ_{recovery}, the time required for each cell to recover to 50% of its post-adaptation activity level ($a_{\text{adapted},i}$). When observing the distributions of these parameters we noted that the cell-to-cell variation is high in the precision Π (Fig. 3.2b, CV=0.40) but the average precision (0.79) agrees well with population measurements [136].

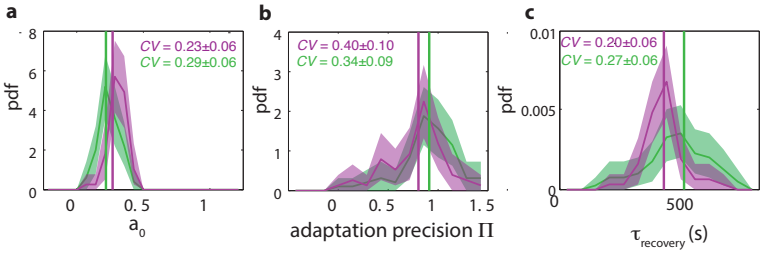

Figure 3.2: Adaptation system shows cell-to-cell variation. Cells obtained from two independent experiments (one shown in Fig.3.1, purple, and another in green). **(a)** Steady-state activity a_0 of the cells from the population. Also shown are the mean steady-state activity (vertical lines). **(b)** Adaptation precision Π obtained from the FRET data. An adaptation precision of 1 denotes perfect adaptation. Also shown are the mean precision levels (vertical lines). All colored shaded areas represent 95 % confidence intervals obtained through bootstrap resampling. **(c)** Recovery time of cells defined as time to reach 50% of the post-adaptational activity level.

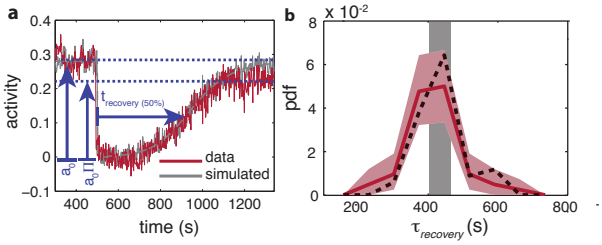

Figure 3.3: Influence of experimental noise on estimating recovery times. (a) Simulated time series are calculated by integrating the linearized MWC model with adaptation kinetics [215] with parameters chosen to closely approximate the population averaged response (grey-dashed line). To the simulated time series of each cell, gaussian white noise ($\mu = 0; \sigma = 0.15$, 55 cells) is added to approximate the noise level of the experiment. Also shown are the baseline and recovery levels (blue dashed lines) of the experimental population.**(b)** Comparison of distributions from experimental data and simulation. Data consists of cells with recovery times defined as time to reach 50% of the post-adaptational activity level (red, 54 cells) or 50% of pre-stimulus activity (black dashed, 44 cells with precision >0.5) and simulated effect of experimental noise for a population with identical recovery times (grey bar, width 2 s.d. from simulated time series in panel a).

The variation is also substantial in τ_{recovery} (Fig. 3.2c, CV=0.20) considering that the underlying kinetics of receptor methylation (catalyzed by CheR) involve thousands of events per cell, but falls within the range of ~20-50% from previous reports in which single-cell recovery times were estimated from motor-rotation or swimming-behavior measurements [14, 127, 195]. The time required to recover from a saturating amount of attractant is determined not only by the stimulus size, but also the methylation rate of receptor modification sites catalyzed by CheR and the number of such sites that need to be methylated. Variability in the recovery time is thus likely to reflect cell-to-cell variation in the ratio between the expression level of CheR and that of the chemoreceptor species responding to ligand (Tar for the experiment in Fig. 3.1).

The diversity we observed here in adaptation precision, recovery time and steady-state activity are reproducible across experimental days (Fig. 3.2), was not explained by variation in salient experimental parameters (see Fig. 2.13a-f), and, on average, agrees well with previous population-level FRET experiments and single-cell flagellar-based experiments (see above). We thus conclude that single-cell FRET allows efficient measurement of signaling dynamics within individual bacteria to reveal variability in a wide variety of signaling parameters.

3.3 Modulation of ligand response diversity during population growth

The chemoreceptor clusters in *E. coli* are the central processing units of the chemotaxis network and are responsible for signal integration and amplification. The sensory output of the cluster, the activity of the kinase CheA, is activated by a mixture of chemoreceptors. Cooperative interactions within the receptor-kinase complex leads to amplifications of small input stimuli and weighting different input signals. It has been shown that the composition of the receptor-kinase complexes can affect both the amplification as well as the weighting of different input signals [4, 80, 193], but how the amplification and integration varies across a population has not been characterized. To bridge the gap between collective behavior and its underlying single-cell motility it is essential to determine the variability of these important signaling parameters, as well as the origin of the variability. Also, current estimates of the apparent gain in the response (defined as the fractional change in output divided by fractional change in input) are based on population-averaged measurements which may may not reflect single-cell cooperativity levels. In population averaged measurements, the largest gain is observed in adaptation-deficient (CheRB-) cells [193], in which the receptor population is homogeneous with respect to their adaptational modification state and hence in these cells variability in ligand sensing can be studied separately from variability induced by the adaptation enzymes.

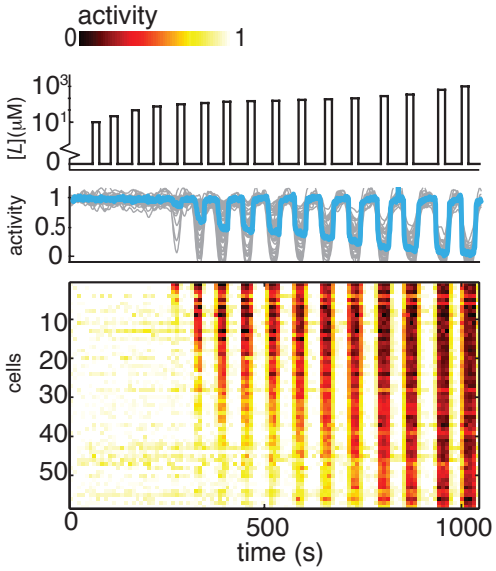

Figure 3.4: Response diversity measured by a single-cell dose-response experiment on adaptation deficient (CheRB-; TSS58) cells with a wildtype complement of receptors. (Top) Temporal protocol of stimulation $[L](t)$ by the attractant L-serine. (Middle) The ensemble-averaged FRET response of the population (blue) and single cells (gray) in signaling activity of 59 cells from a single experiment, normalized to the full-scale FRET response amplitude. (Bottom) Heatmap representation of the single-cell FRET timeseries, with the rows sorted by the sensitivity K of the corresponding cell obtained from Hill-curve fits.

We probed the ligand sensitivity of CheRB- cells (TSS58) at the single-cell level by FRET dose-response measurements in which step stimuli of successively larger amplitudes were applied over time (Fig. 3.4). Considerable variability in the response to the attractant L-serine were observed across the population of immobilized cells simultaneously experiencing the same stimulus, with response magnitudes often ranging from virtually zero to full response (Fig. 3.4). The resulting dose-response data could be well described by a Hill curve of the form $[1 + ([L]/K)^H]^{-1}$, where the parameters $(1/K)$ and H are defined as the sensitivity and steepness, respectively, of the response of each cell. The family of dose response curves constructed from this ensemble of fit parameters reveals considerable variability from cell to cell in the shape of the response curve (Fig. 3.5 and 3.6).

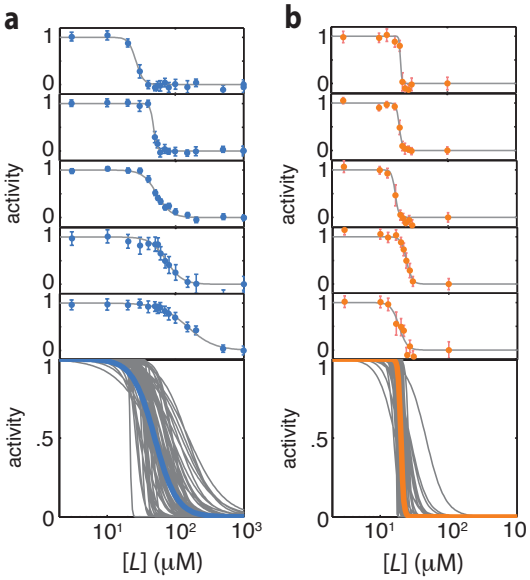

Figure 3.5: Diversity in dose response curves depends on the number of chemoreceptor species. **(a)** Ensemble of Hill-curve fits (gray) to single-cell dose-response data from a single experiment on CheRB- cells with a wildtype complement of receptors (TSS58). Fits for five example cells from the ensemble are shown above together with data points (error bars: ± 2 s.e.m. over 19 frames). The blue curve overlaid on the ensemble was obtained by applying the same analysis to the population-averaged time series shown in panel (a), yielding fit values K=50±3 μM and H=2.7±0.5. **(b)** As in panel (a), but with CheRB- cells expressing only the serine receptor Tsr (UU2567/pPA114). The orange curve was obtained from fits to the population average, yielding K=20.0±0.3 μM and H=22±8.

What could be the cause of the diversity in ligand response in the absence of adaptation-induced heterogeneity? We reasoned that expression-level variability of the five chemoreceptor species of *E. coli*, which are known to form mixed clusters with cooperative interactions [4, 193], could endow isogenic populations with sensory diversity. In line with this idea, CheRB- cells expressing only a single chemoreceptor species (Tsr) demonstrated not only higher cooperativity, but also attenuated variability in the dose-response profile from cell to cell (Fig. 3.5a-b), showing that the composition of the receptor population is important not only to tune the average ligand response of a population, but also in generating a wide range of sensory phenotypes within an isogenic population.

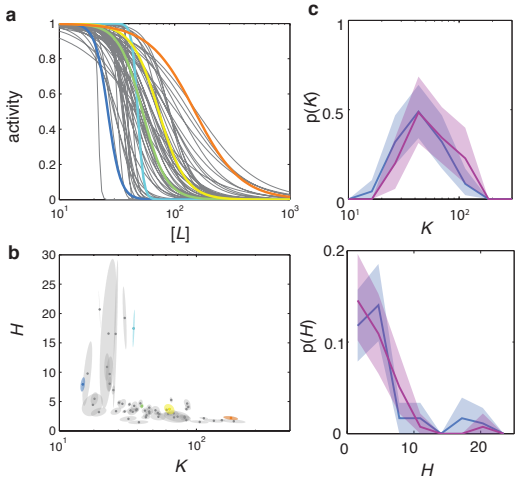

Figure 3.6: Cell-to-cell variability in dose response parameters cannot be explained by fit parameter uncertainty and is reproducible between different experiments. **(a)** Fitted dose response for five representative cells are highlighted in color, within the ensemble for a population of 59 cells from a single experiment (same data as Figure 3.5). **(b)** K and H parameter-fit uncertainty basins, with long and short axes obtained from eigendecomposition of the covariance matrix for each fit, with the highlighted cells corresponding to the same example cells as in panel (a). **(c)** Day-to-day variability in dose-response phenotype distributions. Distribution of parameter K (top) and H (bottom) from a single FRET experiment performed on different days. Together with the data from panels a-b (blue) an additional experiment is shown with 44 out of 45 cells. Shaded areas represent 95% confidence intervals obtained by bootstrap resampling.

It has been shown that expression level of chemoreceptors changes during growth of *E. coli* batch cultures: concomitant with the slowing of growth upon the transition from the exponential phase towards early stationary phase, the relative expression level ratio Tar/Tsr, the two most abundant chemoreceptors, increases from majority Tsr (Tar/Tsr< 1) to majority Tar (Tar/Tsr> 1) [80, 165]. To probe the consequence of such changes for ligand-sensing diversity, we measured single-cell dose response curves in populations harvested at different cell densities during batch growth (Fig. 3.7). The resulting population-averaged responses show a dependence of dose-response parameters on the optical density (O.D.) of the culture, shifting from highly sensitive (low K) and highly cooperative (high H) at low cell densities (OD$\approx$ 0.3) to less sensitive (high K) and less cooperative (low H) at increased cell densities (OD$\approx$ 0.45, and OD $\approx$ 0.6) (Fig. 3.7a and 3.7b, open triangles). This trend is also visible at the level of single cells, but we found the responses to be highly variable under each condition (Fig. 3.7b, filled points).

Remarkably, both K and H varied by over an order of magnitude.

To further test the idea that ligand-response diversity is governed by differences in receptor expression levels, we considered the pattern of covariation between the fitted sensitivity K and cooperativity H in single cells (Fig. 3.7c, blue). In contrast to cells expressing Tsr as the only chemoreceptor, in which the variability in K is only ≈15-20 % (Fig. 3.5b), single cells expressing a wildtype complement of chemoreceptors demonstrated strong variation in K. This variation was negatively correlated with the cooperativity H (Fig. 3.7b). Noting that this overall pattern of covariation agrees well with dose response parameters obtained from population-level FRET experiments in which the Tar/Tsr ratio was experimentally manipulated via plasmid-based expression control (Fig. 3.7b, red circles; data from [193]), we proceeded to quantitatively estimate the diversity in the Tar/Tsr ratio via fits of a multi-species MWC model [85, 123] to single-cell FRET data (see Measuring FRET in single bacteria). The resulting distribution of single-cell Tar/Tsr estimates (Fig. 3.7c) was dominated by Tsr in cells harvested early (OD≈ 0.3) but the relative contribution of Tar increased in cells harvested at later stages of growth (OD≈ 0.45 and OD≈ 0.6). Interestingly, in addition to this increase in the mean of the Tar/Tsr distribution during batch growth, which confirms previous reports that found increased Tar/Tsr ratios at the population level [80, 165], we find that the breadth of the distribution also increases at later stages of growth. Thus, modulation of receptor expression during growth provides a means of tuning not only response sensitivity and cooperativity, but also single-cell diversity in the response of cell populations experiencing identical changes in their common environment.

The large variability in the Tar/Tsr ratio ($CV \approx 0.5$ at O.D.=0.45) is somewhat surprising given that the mean expression level of both receptors are known to be high and of order 10^3-10^4 copies per cell [102]. At such high expression, intrinsic noise in expression levels (i.e. due to the production and degradation process of proteins, expected to scale as the square root of the mean) could be as low as a few percent of the mean, and gene-expression fluctuations are expected to be dominated by extrinsic noise components (i.e. those affecting regulation of gene expression, which do not scale with the mean). Quantitative measurements of gene expression reported in previous studies indicate a high degree of covariation among the expression level of chemotaxis genes, both at the population level under changes in growth conditions [102] and, at the single-cell level across isogenic cells sampled from the same growth culture [90]. Correlated expression-level variation is also expected given the architecture of the flagellar regulon, in which all chemotaxis genes are under the control of a common master regulator [32]. These results indicate that the extrinsic (correlated) component of variation is greater than the intrinsic (uncorrelated) variability. Interestingly, however, a recent study [234] found using single-cell flow-cytometry a high degree of variability in the ratio of Tar/Tsr promotor activities ($CV \approx 0.45$ at O.D.=0.51) comparable to

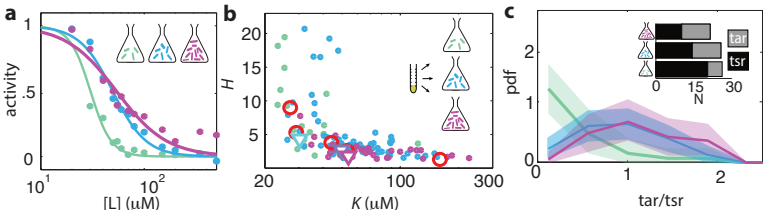

Figure 3.7: Diversity in dose response parameters can be explained by variability in expression ratio of chemoreceptor species. Cells from a single overnight culture were inoculated into three flasks harvested at different times during batch-culture growth to sample the state of the population at three points along the growth curve: at OD_{600}=0.31 (green), 0.45 (blue) and 0.59 (purple). **(a)** Fits to the population-averaged time series. **(b)** Hill-curve sensitivity ($1/K$) and cooperativity H obtained from fits to the single-cell dose-response data, at different harvesting OD's (filled dots) together with the fit values for the population-averaged dose-response data (triangles). Also shown are population-FRET results from [193] in which the average Tar and Tsr levels were tuned using inducible promotors (red circles). Shown are 25 out of 28 cells harvested at OD=0.31, 59 out of 64 cells at OD=0.45, 34 out of 40 cells at OD=0.59. The excluded cells had fits with a mean squared error higher then 0.05. **c)** Histograms of Tar/Tsr ratio obtained by fitting the multi-species MWC model from [123] to single-cell FRET time series. The mean Tar/Tsr ratios (low to high OD) are 0.4, 0.9, and 1.2 with coefficients of variance of respectively 1.1, 0.5, and 0.4. Inset: average cluster size (MWC-model parameter N) of Tar (grey) and Tsr (black) at different harvesting OD's obtained from the fit results in panel b.

the range of ratios extracted from our analysis of dose response data. Given that cell-to-cell variation in the Tar/Tsr ratio is much greater than achievable lower bounds of gene-expression noise in bacteria, it would be interesting to investigate the mechanistic sources of this variability, such as operon organization, promotor stochasticity, and translation-level regulatory structures [65].

Variability in receptor expression could also explain the distribution of adaptation precision we observed in wildtype cells (Fig. 3.2b). In a previous population-level study, it has been shown that adaptation precision depends strongly on the expression-level ratio between the multiple chemoreceptor species, with the highest adaptation precision being achieved when the ligand-binding receptor is a minority within the total receptor population [136]. Thus, the substantial heterogeneity in adaptation precision we observed (CV = 0.40) upon a saturating MeAsp stimulus is consistent with strong variability in the Tar/Tsr ratio.

3.4 CheB phosphorylation feedback attenuates cell-to-cell variation

While bacteria can exploit molecular noise for beneficial diversification, variability can also limit reliable information transfer and degrade sensory performance. In the framework of *E. coli*'s run-and-tumble navigation strategy, chemotactic response to gradients requires that cells maintain a finite tumble bias, the fraction of time a bacterium spends tumbling, and avoids extreme values zero and one. The latter cases would correspond to unresponsive phenotypes that fail to switch between run and tumble states in response to the environmental inputs. One important mechanism that ensures responsiveness to stimuli over a broad range of input levels is sensory adaptation mediated by the methyltransferase/methylesterase pair CheR/CheB. These receptor-modifying enzymes provide negative feedback through the dependence of their catalytic activity on the receptor's signaling state: the rate of methylation (demethylation) by CheR (CheB) is a decreasing (increasing) function of receptor-kinase activity [5, 20]. This dependence of enzyme activity on the substrate conformation provides negative integral feedback that ensures precise adaptation [10] toward the pre-stimulus steady-state activity a_0.

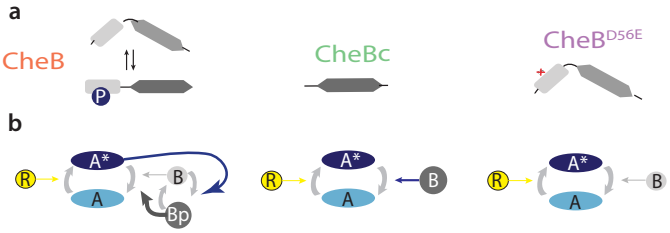

Figure 3.8: CheB mutants defective in phosphorylation have a distinct network topology without additional feedback loop. **a** (Left) CheB consists of two domains connected by a flexible linker. The aspartate at residue 56 within the N-terminal receiver domain can be phosphorylated. (Middle) CheBc lacks the receiver domain with the phosphorylation site. (Right) CheB-D56E carries a point mutation at the phosphorylation site. **(b)** Network topology corresponding to each CheB mutant.

Interestingly, one of the two adaptation enzymes, CheB, can be phosphorylated by CheA, the kinase whose activity CheB controls through its catalytic (demethylation) activity on receptors. Effectively, this adds an additional negative feedback loop to the network, but the role of this phosphorylation-dependent feedback has remained elusive since it has been shown to be dispensable for precise adaptation [3]. Through theoretical analysis, it has been conjectured

that this secondary feedback loop might play a role in attenuating effects of gene-expression noise [90], but experimental verification has been lacking. We therefore sought to investigate the influence of perturbations to this network topology on the variability of chemotactic signaling activity.

CheB consists of two domains connected by a flexible linker (Fig. 3.8). A regulatory domain, with structural similarity to CheY, can be phosphorylated at residue Asp^{56} [48, 197]. A catalytic domain mediates binding to specific residues on chemoreceptor cytoplasmic domains and removes a methyl group added by the counterbalancing activity of CheR. Phosphorylation induces a conformational change and activates CheB (CheB*) [48, 111]. Several mutants of CheB lack phosphorylation feedback while retaining catalytic activity. Here, we focus on two specific mutants: $CheB^{D56E}$, which bears a point mutation at the phosphorylation site, and $CheB_c$, which expresses only the catalytic domain of CheB [3, 197]. Cells expressing these mutants have an altered network topology (Fig. 3.8b) which lacks CheB phosphorylation feedback.

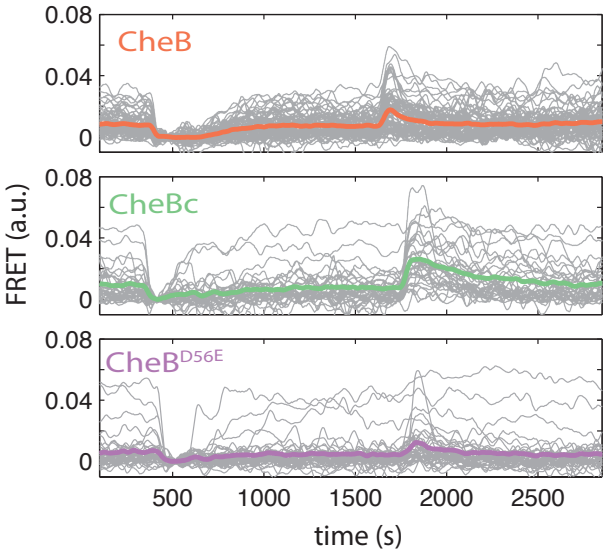

Figure 3.9: CheB mutants defective in phosphorylation show increased variability of steady-state network activity. Example FRET time series for cells expressing $CheB^{WT}$ (top, pink), $CheB^{D56E}$ (bottom, purple), $CheB_c$ (middle, green) in ΔCheB (VS124) background.

To study the influence of network topology on cell-to-cell variation, we expressed different forms of CheB ($CheB^{WT}$, $CheB^{D56E}$, $CheB_c$) from an inducible promoter in a Δ*cheB* strain and measured the response to a saturating amount

of attractant (500 μM MeAsp). The expression levels of each mutant are tuned such that they approximate the wildtype steady state activity level. The response of $CheB^{WT}$ was qualitatively very similar to cells in which CheB is expressed from its native chromosomal position (compare Fig. 3.9 and Fig. 3.1a) despite the fact that plasmid expression breaks the translational coupling with CheR [109]. By contrast, cells expressing either of the two CheB mutants defective in phosphorylation demonstrated increased cell-to-cell variation in the steady-state activity compared to cells expressing $CheB^{WT}$. The increased variability of the CheB phosphorylation-deficient mutants ($CheB^{D56E}$ and $CheB_c$) was manifested not only in a higher coefficient of variation in a_0 (1.07 and 1.10, respectively, and WT 0.7), but also a qualitatively different shape of the distribution of a_0 across the population (Fig. 3.10a). Whereas the distribution demonstrated a single peak in $CheB^{WT}$ cells with phosphorylation feedback, the distribution for the phosphorylation-feedback mutants demonstrated a bimodal shape with peaks close to the extreme values $a_0 = \{0, 1\}$.

We tested whether these strong differences in cell-to-cell variation might be the result of gene expression noise, by comparing expression-level distributions of the CheB mutants. We constructed fluorescent fusions of each *cheB* allele to the yellow fluorescent protein mVenus and quantified the distribution of single-cell fluorescence levels under the same induction conditions as in the FRET experiments (Fig. 3.11). The ratio between the measured expression-levels (CheBc:WT:D56E≈0.7:1:2.5) was compatible with expectations from the hierarchy of reported *in vitro* catalytic rates of CheB ($k_b^{D56E} < k_b^{WT} < k_b^c$) [6, 186, 196], and expression-level variability was very similar between the three strains (CV's of 0.87,0.90 and 0.82; we note that these rather high CV values likely include contributions from plasmid copy number variability). These findings suggest that the differences in cell-to-cell variation observed in FRET are not due to differences between the expression-level distributions of the three *cheB* alleles, but rather to the differences they impose on the signaling network topology.

What feature of the signaling network could generate such broad (and even bimodal) distributions of a_0? A general paradigm for models of adaptation that exhibit precise adaptation is activity-dependent (integral) feedback [10, 233], which in bacterial chemotaxis can be implemented by the activity of the feedback enzymes CheR and CheB being dependent of the conformational state (i.e. activity) of their substrate chemoreceptors. This results in a steady-state activity a_0 that only depends on the [R]/[B] expression-level ratio and not on their absolute abundance. We can view this mapping as a transfer function f between the ratio [R]/[B] and the steady-state activity a_0,

$$a_0 = f([\mathrm{R}]/[\mathrm{B}])$$

Depending on the function f, the input variance $P_{RB}([\mathrm{R}]/[\mathrm{B}])$ may lead to high or

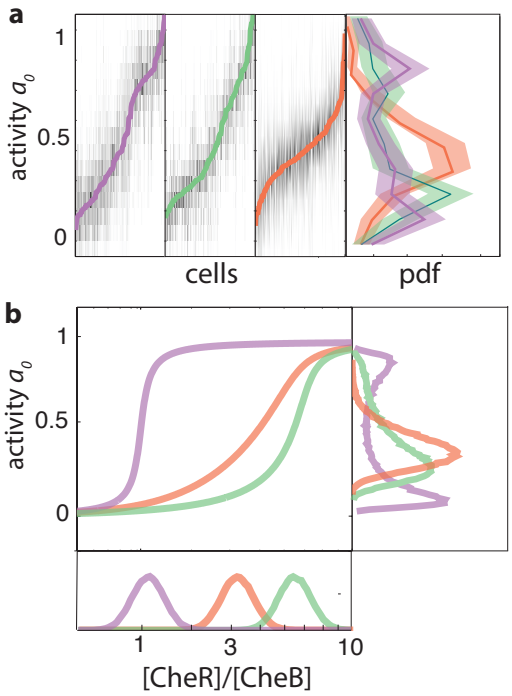

Figure 3.10: The absence of CheB phosphorylation feedback generates bistability in steady-state kinase activity. **(a)** Heatmap representation of histograms of the activity $a(t)$ about the unstimulated steady-state of single cells, from FRET experiments of the type shown in Figure 3.9. Each column represents a single cell, sorted by the steady-state activity a_0 (colored curves) for each CheB mutant expressed in a *cheB* background (VS124, colors as in panel (a)). (right) Normalized histograms (probability density function, pdf) of a_0 for each CheB mutant. Histograms contain results for cells with a signal-to-noise ratio greater than 1 from at least 3 independent FRET experiments, corresponding to 231 out of 280 cells (WT), 169 out of 210 cells (CheBc) and 156 out of 246 cells (D56E). Shaded regions represent bootstrapped 95% confidence intervals. We verified that the bimodality was not due to clipping from FRET-pair saturation, by mapping the dependence of FRET on donor/acceptor expression (Figure 2.10). **(b)** A simple kinetic model of the chemotaxis network illustrates the crucial role of CheB phosphorylation feedback in circumventing detrimental bimodality in a_0. Due to sublinear enzyme kinetics in the adaptation system, the transfer function $a_0 = f([R]/[B])$ mapping the $[R]/[B]$ expression ratio to steady-state network output a_0 can be highly nonlinear (main panel). The shape of this transfer function determines the distribution $P(a_0)$ of steady-state activity (right panel) by transforming the distribution $P([R]/[B])$ of adaptation-enzyme expression ratios (bottom panel). Three variations of the model are shown, corresponding to WT (orange, with phosphorylation feedback), $\text{CheB}^{\text{D56E}}$ (purple, no phosphorylation feedback and low catalytic rate), and CheBc (green, no phosphorylation feedback, high catalytic rate).

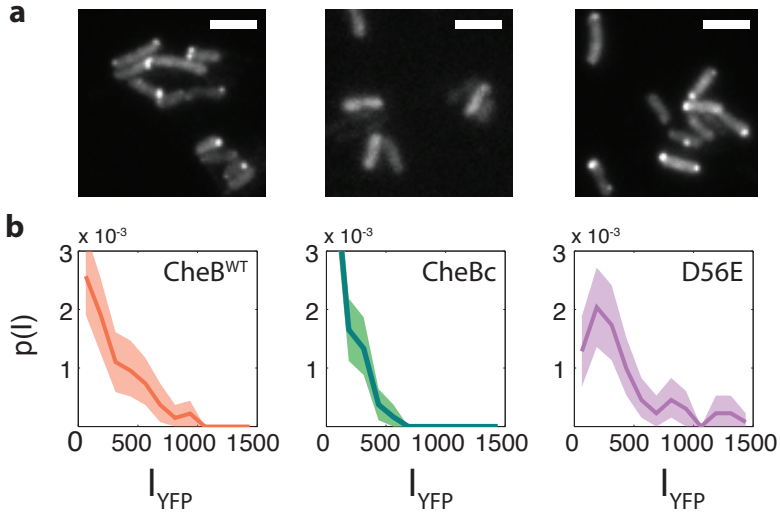

Figure 3.11: Differences in variability of kinase activity between CheB mutants is not caused by CheB expression-level distrubutions. **(a)** Localization of CheB in the cell probed by mVenus fusions to CheB. Clustering was quantified by the fraction of cells clearly showing one or more clusters in the cell. Shown are representative examples of $CheB^{WT}$ (left, 78% clustered), $CheB_c$ (middle, 0%), $CheB^{D56E}$ (right, 72%). Scale bars 2 µm. **(b)** Histograms of fluorescence intensity for single cells in units of photons/pixel. Mean and standard deviation of these distributions for the strains is (from left to right) 272 ± 237 (114 cells), 148 ± 133 (150 cells) and 398 ± 328 (106 cells). This corresponds to a CV of 0.87, 0.90, 0.82 for the three CheB genotypes, respectively. These cellular fluorescence intensities are corrected for inhomogeneous illumination as well as differences in cell area, and thus can be considered proportional to the cellular concentration of the respective *cheB* gene products.

low variance in the distribution $P(a_0)$. This is because the manner in which the transfer function f filters the [R]/[B] distribution,

$$P(a_0) = \frac{P_{RB}(f^{-1}(a_0))}{\left|f'(f^{-1}(a_0))\right|}.$$

Hence a steep function f can impose bimodality in the methylation level, and thereby also in the activity of steady-state CheA activity, a_0, even at quite modest input variances for distributions of the ratio [R]/[B].

Thus, even if expression-level noise for both CheR and CheB are modest, a sensitive transfer function f can effectively amplify the variation in [R]/[B], and if the distribution of the latter ratio, $P_{RB}([\mathrm{R}]/[\mathrm{B}])$ extends below and above

the narrow region over which f is steep, the decreased slope of f (i.e. lower $f'([R]/[B])$) in those flanking regions will tend to increase the weight on both sides of the broad $P(a_0)$ distribution to produce a bimodal profile. On the other hand, if the network topology effectively reduces the steepness of f, the resulting $P(a_0)$ will have a reduced variance for the same input $P_{RB}([R]/[B])$ (Fig. 3.10b). Our results suggest that f is much steeper in the absence of phosphorylation feedback than in its presence.

We find that models with linear or supra-linear dependence of the methylation rate on activity generate a function f that is very shallow (Fig. 3.12), making them unsuitable for explaining the observed bimodal behavior. However, if we assume CheR and CheB follow Michaelis-Menten kinetics in which the dependence of the methylation rates on receptor activity is sub-linear, the dependence of f on [R]/[B] can become very steep. It has been conjectured [10, 57] that *in vivo* the enzymes CheR and CheB operate at or near saturation, an idea supported by population-level FRET measurements of adaptation kinetics [183]. An important consequence of enzyme saturation in such reversible modification cycles is that the steady-state activity of the substrate can become highly sensitive to the expression level ratio of the two enzymes, a phenomenon known as zero-order ultrasensitivity ([69]; see Materials and Methods). Within the chemotaxis system, saturation of both CheR and CheB can thus render the receptor modification level, and in turn, the CheA activity a_0, ultrasensitive to the [R]/[B] concentration ratio [57].

Could the known biochemical differences between the three forms of CheB ($CheB^{WT}$, $CheB^{D56E}$, $CheB_c$) explain the contrasting patterns of a_0 variability observed in our single-cell FRET experiments? In the absence of any feedback, the steepness of $f([R]/[B])$ is solely determined by the low Michaelis-Menten constants $K_{B,R}$, which corresponds to saturated kinetics of the enzymatic activity of CheRB and hence ultransensitivity of the steady-state substrate activity. The expression ratio of CheR/CheB which determines the crossover point (a_0=0.5) is set by the ratio of catalytic rates of CheR and CheB ($k_{r,b}$). Hence the phosphorylation deficient mutants $CheB^{D56E}$ and $CheB_c$ both have steep curves but are shifted along the R/B axis due to very different catalytic rates. However,in the case of phosphorylation feedback, $CheB^{WT}$, the same enzyme can be in two states, each with equal $K_{r,b}$ but one low and one high k_r. Whether CheB is in the one state or the other is determined by the activity-dependent phosphorylation feedback. As a result, the curve of $CheB^{WT}$ is activity dependent ($f(a,[R]/[B])$) and changes with activity by shifting between the two curves corresponding to the extremes of all phosphorylated or all unphosphorylated. Effectively, this makes the resulting curve f less steep [57]. The mean of the distributions P_{RB} are tuned such to get the same mean activity level ($\langle a_0 \rangle$), but the same variance in P_{RB} leads to very wide $P(a_0)$ distributions in absence of phosphorylation, while phosphorylation feedback ensures a much smaller, single-peaked distribution.

It has also been conjectured that the CheB phosphorylation feedback is

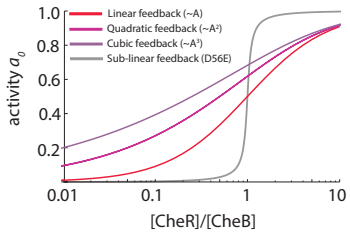

Figure 3.12: Linear and supralinear models of CheB feedback cannot explain bimodality in a_0. As explained in the main text, bimodality in the steady-state receptor-kinase activity a_0 could be explained by a steep transfer function $f([R]/[B])$ mapping the expression-level ratio of adaptation enzymes $[R]/[B]$ to a_0. Shown here are $f([R]/[B])$ for models of the form $dm/dt = g(R,a) - h(B,a)$, in which g and h represent the (de)methylation rates due to CheR and CheB, respectively, and the dependence of g and h on a is (supra)linear (as discussed e.g. by [35]). The steady-state relation $a_0 = f([R]/[B])$ for each case is found by solving $g(R,a) = h(B,a)$ (see Materials and Methods). In all three models the same CheR-dependent methylation is considered, $g(R,a) = k_b[R](1-a)$ and CheR and CheB are assumed to have the same catalytic rates ($k_b = k_r$). In the absence of phosphorylation, the CheB-dependent feedback depends linearly on the receptor-kinase activity ($f(B,a) = k_b[B]a$, red) while CheB phosphorylaton is modeled as quadratic ($f(B,a) = k_b[B]a^2$, light purple) or cubic ($f(B,a) = k_b[B]a^3$, purple) dependence. While phosphorylation feedback clearly decreases the slope of $a_0 = f([R]/[B])$, the steepness of $f([R]/[B])$ is greatly attenuated for these models with (supra)linear feedback, compared to the case with sublinear feedback (Equation 3.6, grey curve). To explain a_0-bimodality with these shallow transfer functions of the (supra)linear models, one would need variability in the expression-level ratio [R]/[B] to span a range much greater than 10^2-fold, which is unlikely given the measured variability in expression level of chemotaxis genes [90, 234].

responsible for the highly nonlinear kinetics of recovery from repellent (or attractant removal) responses [35, 183]. Indeed, in cells expressing CheB_c, the kinetics of recovery from the response to removal of 500 μM MeAsp after adaptation appeared qualitatively different from that in cells expressing wildtype CheB, lacking the characteristic rapid recovery and instead appearing more symmetric with the CheR-mediated recovery upon addition of a saturating dose of attractant (Fig. 3.13). By contrast, $\mathrm{CheB}^{\mathrm{D56E}}$ was found to still possesses a fast component, despite being defective in phosphorylation, albeit also with somewhat slower kinetics than wt. In summary, the clearest difference between wildtype and phosphorylation-defective CheB mutants is found in the variability of the steady-state signal output (i.e. kinase activity).

The bimodal distribution in kinase activity we observed in the phosphorylation-deficient CheB mutants implies that a large fraction of cells have a CheY-P concentration far below or far above the motor's response threhold and hence

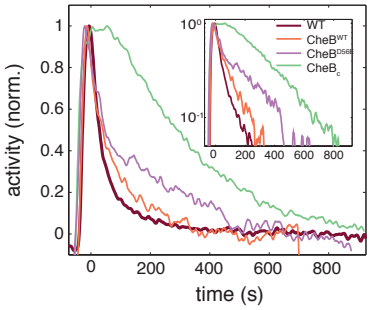

Figure 3.13: Phosphorylation feedback is not a necessary condition for fast removal adaptation dynamics. Population FRET time series of cells expressing $CheB^{WT}$ (orange), $CheB^{D56E}$ (purple) , $CheB_c$ (green) in ΔCheB (VS124) background as well as WT (CheB from native chromosome position, VS104, brown) are shown after removal of 500 μM to which cells have adapted. The strain expressing $CheB^{D56E}$ lacks phosphorylation feedback but has a fast removal response. The population FRET experiment is performed as described previously [192]. The strains and induction levels are the same as in the single-cell FRET experiments on the CheB mutants.

will impair chemotactic responses to environmental gradients. Consistent with this idea, in motility-plate experiments (Fig. 3.14) we found that chemotactic migration on soft-agar plates was severely compromised for both $CheB^{D56E}$ and $CheB_c$ compared to $CheB_{WT}$, indicating that the phosphorylation feedback is important for efficient collective motility.

3.5 Discussion

The single-cell FRET measurements described here allowed us to quantify variability across cells in a population in a variety of signaling parameters of the bacterial chemotaxis system. By imaging many (typically ~ 50) cells simultaneously, we are able to record signaling in individual cells at high throughput, to build up single-cell statistics. Although single-cell experiments have a long history in studies of bacterial chemotaxis [13, 17, 49, 91, 195], nearly all examples to date have relied on measurements of flagellar motor output (in either tethered or swimming cells). A major advantage of the FRET approach is that it provides a direct measurement of intracellular signaling that bypasses the noisy behavior of the flagellar motor (a stochastic two-state switch), thereby enabling accurate and efficient determination of signaling parameters.

The anti-parallel response signature of ratiometric FRET provides a good way to discriminate genuine FRET changes from imaging artifacts. As in population-

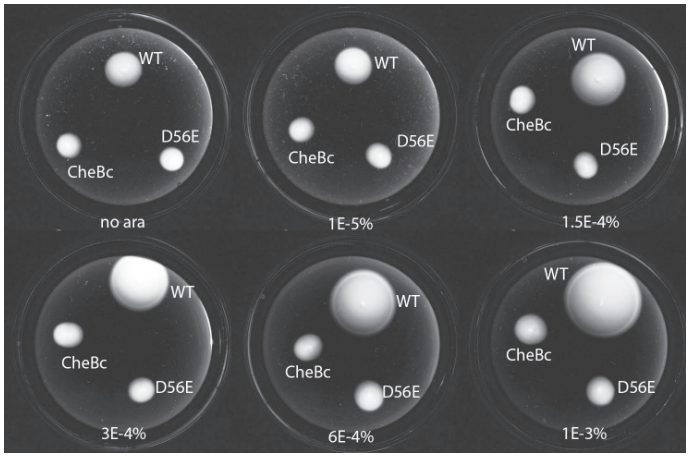

Figure 3.14: Phosphorylation defective mutants show impaired chemotaxis on soft agar. Dark-field images after 14 h of growth and motility on soft agar plates (0.26 % agar in TB with appropriate antibiotics, kept at 33.5 ^{o} C). The different strains express either WT CheB, CheB-D56E and CheBc from an arabinose inducible pBAD plasmid in ΔCheB strain (UU2614). The arabinose concentration is varied from 0 % to 0.001 % as indicated below each plate.

level FRET, single-cell FRET is most easily applied to study large and rapid changes in signaling (e.g. response to step stimuli), but we have shown that with careful correction of drifts in the signal level (primarily due to bleaching, but also including contributions from fluorophore maturation and/or recovery from long-lived dark states), it can be applied effectively to measure more subtle changes in signaling over extended times, including steady-state fluctuations. Care is required in these corrections of long-time fluorescence-intensity drifts because imperfect correction can distort dynamics on timescales comparable to that of the signal drift. We note that our analysis of chemotaxis signaling dynamics presented here is relatively insensitive to such artifacts, given that the longest timescales we observed (~ 400 s for recovery times) are well below the time constants of fluorescence intensity drift (> 1hr under hour experimental conditions), but caution is warranted for future applications to systems with slower dynamics.

3.5.1 From gene-expression noise to diversity in signaling phenotypes

A key feature of bacterial chemotaxis as an experimental system is that one can study *in vivo* signaling and behavior in a manner that is decoupled from gene expression and growth. Being an entirely protein-based signaling network,

chemotaxis signaling responses do not require changes in gene expression, and the relatively short timescales of signaling reactions (subsecond to minutes) are well separated from those of changes in protein counts due to gene expression noise (minutes to hours). The ensemble of single-cell FRET time series measured in each of our experiments thus provide a snapshot of cell-to-cell variation due to stochastic gene expression in a variety of signaling parameters.

Our data revealed high variability in important signaling parameters connected to the adaptation system (Fig. 3.2). In the case of the variability in recovery times (CV=0.20), this is likely due to variability in the CheR/receptor ratio from cell to cell. What consequences might such variability have on chemotactic behavior? A recent theoretical study has established that long (short) adaptation times are better suited for maximizing chemotactic migration rates in shallow (steep) gradients [65]. Thus, variability in adaptation times could partition the population into cells that will be more efficient in running up steep gradients, and others better suited to climbing shallow ones. Interestingly, it was also found that optimal performance at each gradient involves tuning not only the adaptation time, but also other parameters such as swimming speed or tumble bias, leading to the prediction that selective pressures act not only on the distribution of individual parameters, but also on the pattern of covariation among them [65, 225]. Exploring such correlated variation of signaling parameters, both under changes in environmental conditions such as nutrient levels [86] and within identically grown populations, would be a fruitful avenue for future single-cell FRET studies.

In the ligand response of the network, we observed large cell-to-cell variation in the sensitivity ($1/K$) and steepness (H) of dose-response relations, for cells with a wildtype receptor population (Fig. 3.5). Using a mixed-species MWC model [123], we were able to estimate the Tar/Tsr ratio in single cells, which spans a broad range from nearly zero to more than two. This strong variability in the receptor-cluster composition has the potential to dramatically impact behavior. In their natural habitats, cells likely experience a variety chemoeffector gradients simultaneously, each associated with an unknown fitness payoff for chemotactic pursuit. Generating diversity in the chemoreceptor ratio, which has been shown to determine which gradient to climb when challenged with such conflicting possibilities [80], could allow the isogenic population to hedge its bets to maximize net fitness gains. The Tar/Tsr ratio has also been shown to play an important role in setting the preferred temperature for thermotaxis [146, 165, 234]. Variability in Tar/Tsr would allow diversification of the preferred temperature across cells in the population, which will promote spreading of bacteria in environments with temperature gradients. Finally, when chemotactic bacteria colonize an initially nutrient-rich environment, they are known to successively exploit resources by emitting multiple traveling waves of chemotactic bacteria, each of which consumes and chases by chemotaxis a different nutrient component outward from the colony origin [2]. Our observation that the population diversity in receptor ratios, and

hence chemotactic preference, varies concomitantly with population growth could provide a means to tune the population fractions that engage in such excursions into virgin territory, and those that remain for subsequent exploitation of remaining resources. Thus, the diversity in ligand response and preference generated by variability in the Tar/Tsr ratio could have nontrivial consequences in a variety of behavioral contexts encountered by isogenic chemotactic (and thermotactic) populations.

3.5.2 Suppression of gene expression noise by CheB phosphorylation feedback

The role of phosphorylation feedback has been a long standing open question in the field of bacterial chemotaxis signaling, ever since its presumed role in providing precise adaptation was decisively ruled out by [3]. In the ensuing years, a diverse set of hypotheses have been proposed to explain its purpose. Apart from precise adaptation, CheB phosphorylation has been suggested as possibly responsible for the non-linear response of CheB activity to changes in CheA kinase activity [35, 183], ligand sensitivity of wildtype cells [9], and has been implicated theoretically as a possible mechanism to buffer gene-expression noise to suppress detrimental variability in the steady-state kinase activity [57, 90, 150]. Here, we tested the latter hypothesis, by severing the phosphorylation feedback loop as a possible noise-reduction mechanism. Our single-cell FRET data revealed that, not only does CheB phosphorylation feedback strongly attenuate the magnitude of variability in the steady-state kinase activity a_0, it also qualitatively changes the shape of the distribution $P(a_0)$ across cells to convert an otherwise bimodal distribution into a unimodal one (Fig 3.10b). The highly polarized bimodal distribution of steady-state activities in CheB phosphorylation mutants are likely detrimental, as they could drive a_0 of a large fraction of the population too far from the flagellar motor's steep response threshold [36, 236] to effectively control swimming.

By analyzing simplified models of adaptation kinetics, we found that a bimodal $P(a_0)$ could occur in the absence of phosphorylation feedback if the enzyme kinetics of CheR and CheB depend sublinearly on the activity a of their receptor substrates. As a limiting case, when both enzymes work at or near saturation, this model leads to zero-order ultrasensitivity [57, 69], which could act as a strongly non-linear transfer function $f([R]/[B])$ that converts a unimodal distribution $P([R]/[B])$ into a bimodal $P(a_0)$. We note that ultrasensitivity due to sublinear (Michaelis-Menten) enzyme kinetics is by no means the only possible explanation for the observed bimodality in $P(a_0)$. Any mechanism that renders $f([R]/[B])$ a strongly nonlinear (sigmoidal) function could lead to the same effect. The merit of the sublinear kinetic (ultrasensitivity) model is in its simplicity, but it is worth noting that reality is likely to be more complex due to, for example,

effects of spatial organization. It is known that both CheR and CheB interact with chemoreceptors not only at their substrate modification residues, but also with a second binding site on a flexible tether at the receptor C-terminus. Such bivalent interactions with the receptor array could affect the movement of these enzymes across the receptor lattice [100], and such movements could shift the balance between processivity and distributivity of enzyme activity on their substrate receptors [150], which could in turn attenuate or enhance the nonlinearity in the relationship $f([\mathrm{R}]/[\mathrm{B}])$ between the enzyme expression ratio [R]/[B] and the steady-state activity a_0 of their substrate receptors [201].

3.5.3 Concluding remarks

We described a new single-cell FRET technique capable of resolving intracellular signaling dynamics in live bacteria over extended times. Our results highlight how a protein-based signaling network can either generate or attenuate variability, by amplifying or filtering gene expression noise. Gene expression noise is harnessed, on the one hand, to generate diversity in the ligand response of isogenic populations, or attenuated, on the other the hand, in the control of steady-state signal output. Together, these examples show that the network topology and the (often nonlinear) signaling dynamics it implements are crucial in understanding the relation between molecular noise and diversity of phenotypes.

While the influence of molecular noise has been studied extensively in the context of gene regulation networks [30], there has been little attention to the role noise in post-transcriptional interaction networks. Many signaling networks involve protein-level interactions, and the chemotaxis network in *E. coli* presents a limit case in which the system's dynamics does not involve changes in gene expression. The dynamics of protein-interaction networks are often more challenging to measure *in vivo* than that of gene regulation networks, but are important for cellular physiology in bacteria and beyond. They often include network-level phenomena not observed in gene regulatory networks, such as high cooperativity and amplification.

On the one hand, direct experimental comparisons on output diversity between network topologies are rare [142, 148], perhaps because they require a high level of understanding of the network to appropriately engineer the topology at the molecular level. On the other hand, if the regulatory network is unknown, the statistics that describe the diversity in network parameters may reveal the underlying regulatory mechanisms, especially when the distributions of parameters can be compared over time [131, 134]. Systematic investigations of network topologies that focus not only on the average network performance but also on diversity in network performance may yield fruitful results in optimizing the design of artificial networks.

3.6 Materials and Methods

3.6.1 FRET experiments

FRET experiments were performed as described in Chapter 2, which includes a list of the strains and plasmids used in this study (§2.4).

3.6.2 Dose Response Curve Analysis

Normalized FRET responses to different levels of ligand are fit to a hill curve of the form

$$a = \frac{[L]^H}{[L]^H + [K]^H} \tag{3.1}$$

This can be connected to an MWC-type model [129] of receptor cluster activity [215] in the regime $K_I << [L] << K_A$, resulting in the correspondence key

$$H = N$$
$$K = K_I e^{f_m(m)}$$

which relates the Hill slope directly to the cluster size N, and sensitivity K to the methylation energy of the receptor. We plot K on a logarithmic scale to scale linearly with energy.

The parameter estimate uncertainties of K and H are defined by the covariance matrix for each cell i

$$\mathrm{COV}_i = \begin{bmatrix} \sigma_{KK} & \sigma_{HK} \\ \sigma_{KH} & \sigma_{HH} \end{bmatrix}_i \tag{3.2}$$

in which σ denotes the standard error from the fit. For each covariance matrix the corresponding eigenvectors and eigenvalues are determined. The eigenvalues and vectors constitute an ellipsoid which represent error basins in $K - H$ space.

To obtain expression level estimates of different receptor species we use a different MWC model. Following [123], we use as an expression for the normalized response of cells to ligand $[L]$ serine

$$a = \frac{\epsilon_0 \epsilon_S^{N_S} \epsilon_A^{N_A} (1 + C[L]/\tilde{K})^{N_s}}{(1 + [L]/\tilde{K})^{N_s} + \epsilon_0 \epsilon_S^{N_S} \epsilon_A^{N_A} (1 + C[L]/\tilde{K})^{N_s}} \tag{3.3}$$

in which N_A is the number of Tar receptors in the cluster and N_S is the number of Tsr receptors. Parameters ϵ_A, ϵ_S, ϵ_0 are the energies corresponding to binding of ligand to Tar, Tsr and the other three receptors and are the same for each cell, like C and $\tilde{K}$ which describe the disassociation constant for the active state as $K_A = \tilde{K}/C$, while N_A and N_T may vary from cell to cell. This yields the

minimization problem for all 128 cells

$$\min \sum_{i}^{N_{cells}} \sum_{j}^{N_{stim}} (m_{i,j} - a_{i,j})^2 \tag{3.4}$$

in which $m_{i,j}$ the measured FRET response normalized to the response amplitude of cell i to stimulus L_j. This function was minimized using the matlab function fmincon (optimization toolbox). The total number $N_T = N_A + N_S$ is limited to 32. When fitting the model used the energy parameters ϵ from reference [123] where used as initial guess with a maximum of ±5% deviation. This yielded an estimate of N_A and N_S for each cell. Under the assumption that receptor clusters are well-mixed, this yields a Tar/Tsr ratio of N_A/N_S.

Table 3.1: List of global parameters used for model of Mello and Tu. In these fits, $\tilde{K}$ is a free parameter while others are constrained ±5% by published values.

Parameter	Start Value [124]	Final Value
C	0.314	0.29
ϵ_0	0.80	0.84
ϵ_A	1.23	1.29
ϵ_S	1.54	1.61
$\tilde{K}$	–	21.2 μM

3.6.3 Sublinear model of adaptation kinetics with phoshorylation feedback

For our model, we consider CheR and CheB to perform opposite operations on the same substrate. For simplicity, we do not explicitly describe the methylation and demethylation of the receptors explicitly but instead assume that CheR (R) activates the receptor-kinase complex directly (A^*), and that CheB (B) deactivates it (A)

$$A + R \rightarrow A^* + R$$
$$A^* + B \rightarrow A + B$$

In general, the corresponding reaction equation is a function of the methylation of inactive kinases by CheR, and demethylation of active kinases by CheB, described by two functions g and h

$$\frac{da}{dt} = g(v_r, R, a) - h(v_b, a) \tag{3.5}$$

with v_r and v_b being the rates for CheR and CheB, respectively. We now assume that these reactions follow Michaelis-Menten kinetics, following [69] and [57], and the total amount of kinase complexes is constant ($A_T = A^* + A$). Hence the change in activity $a = A^*/A_\mathrm{T}$ has a sublinear dependence on a:

$$\frac{da}{dt} = v_r \frac{1-a}{K_r + 1 - a} - v_b \frac{a}{a + K_b} \tag{3.6}$$

The Michaelis-Menten constants K_b and K_r are in units of A_T and are therefore dimensionless numbers. We are interested in the steady-state level a_0 and its dependence on the kinetic parameters in equation 3.6. This is described by the Goldbeter-Koshland function [217], an exact solution to the system in case [R] and [B] are much smaller than $[\mathrm{A}]_\mathrm{T}$.

$$a_0 = \frac{2 v_r K_r}{(v_b - v_r + v_b K_b + v_r K_r + \sqrt{(v_b - v_r + v_b K_b + v_r K_r)^2 - 4(v_b - v_r) v_r K_r}} \tag{3.7}$$

The shape of this curve is sigmoidal if the Michaelis-Menten constants K_r and K_b are much smaller than one. For CheB phosphorylation, we assume the phosphorylation rate depends linearly on active CheA and write

$$\frac{d[\mathrm{Bp}]}{dt} = k_p[\mathrm{B}]a(v_r, v_b, K_b, K_r) - k_{dp}[\mathrm{Bp}] \tag{3.8}$$

with the corresponding conservation law B_T=B_P+B. For the case for wild-type CheB, with phosphorylation feedback, the rates can be described in terms of catalytic rate times the enzyme (subspecies) concentration

$$\begin{aligned} v_b &= k_b([\mathrm{B}_T] - [\mathrm{Bp}]) + M k_b[\mathrm{Bp}] \\ v_r &= k_r[\mathrm{R}] \end{aligned} \tag{3.9}$$

in which M stands for the ratio of demethylation rates of unphosphorylated and phosphorylated CheB. The fraction of the phosphorylated CheB, $[\mathrm{Bp}]/[\mathrm{B}]_\mathrm{T}$ then determines the effective activity of CheB. Equation 3.8 is solved numerically using Mathematica (Mathematica model source code available online) for [Bp] and the result is substituted in equation 3.7. In the absence of feedback, the activity can be directly calculated from equation 3.7 with the rates being simply

$$\begin{aligned} v_b &= k_b[\mathrm{B}] \\ v_r &= k_r[\mathrm{R}] \end{aligned}$$

We only need to consider the ratio of rate constants k_r and k_b which determines at which expression ratio [CheR]/[CheB] the activity equals 1/2. We assume $k_r = k_b$ for simplicity, since the shape of the curve from Eq. 3.7 is not affected

by the values of k_r and k_b, changing their ratio only shifts the curve along the horizontal axis. Similarly, we only consider the ratio of phosphorylation and dephosphorylation rates. This leaves the system of equations above only has a few parameters: $K_{b,r}$; M; and the ratios k_r/b_b and k_p/k_{dp}. In table 3.2, the parameters used for the calculations are listed.

We first fixed the phosphorylation rates k_p=1/2k_{dp}. This means that the steady-state phosphorylated level of CheB $[B_p]/[B_T]$ at activity $\approx$ 1/3 is around 15 %. This parameter is not constrained by any direct observation, but it is clear the system benefits from a relatively low fraction of phosphorylation, to be able to up and down regulate the levels effectively upon changes in activity.

Generally, we assume CheB-D56E to behave like unphosphorylated CheB. The gain in catalytic rate of activated CheB is estimated to be nearly a 100 fold, but this does not agree with the expression level differences between the different CheB mutants so we made a conservative estimate of 15 (the attenuating effect increases with the gain). CheBc behaves approximately like phosphorylated CheB (albeit with increase of only 7 compared to D56E), qualitatively consistent with measured *in vitro* rates for CheBc and phosphorylated intact CheB [6]. The difference between predicted rates and might be due to the fact that the rate experiments were performed *in vitro*. Michaelis Menten constants used in the model are lower than 1, but how low is not well constrained by data, and estimations do not take into account the possible attenuating effect of phosphorylation. Our experimental data on the distribution of a_0 implies the sigmodial curve is steep in the absence of phosphorylation and hence that K_b and K_r are quite small. The variability in a_0 for CheBc is lower than D56E, implying that the curve is less steep and hence we have chosen are K_r which is not quite as low as D56E.

To simulate gene expression noise, we simulated [CheR]/[CheB] log-normal distributions with $\sigma = 0.18$ for all three strains. The mean of the distribution was chosen to yield an average steady-state network activity (a_0) of 0.4. The resulting distribution of a_0 was calculated using the corresponding Goldbeter-Koshland function for each genotype.

3.6.4 Linear and supralinear models of adaptation kinetics

Instead of assuming a sub-linear (Michaelis-Menten) dependence of CheR- and CheB-catalyzed rates on the receptor-kinase activity a, one may also assume linear, quadratic or cubic dependence of the methylation rates on the activity, as was for example done in [35]. Here, CheR feedback is assumed to be linear ($g = k_r[R](1-a)$), while CheB feedback can be linear ($h = k_b[B]a$), quadratic ($h = k_b[B]a^2$) or cubic ($h = k_b[B]a^3$) in the receptor-kinase activity a. The supralinear (quadratic and cubic) forms of dependence are intended to model the case with CheB phosphorylation, and the linear form the case without CheB phosphorylation. The steady-state activity a_0 can be found by solving $g(v_r, a) =$

Table 3.2: List of parameters used for Goldbeter-Koshland description of CheB phosphorylation feedback.

Parameter	Value	Literature	Source
k_r/k_p	1	0.75	[183]
k_{dp}/k_p	2	$k_p = 0.37\ s^{-1}$	[84]
K_r	0.03	«1	[57]
K_b	0.03	«1	[57]
$K_b(CheBc)$	0.2	«1	
M (WT)	15	100	[6]
M (CheBc)	7	15	[186]

$h(v_b, a)$ and the dependence of a_0 to [R]/[B] (a_0=f([R]/[B])) for these linear and supralinear cases are shown in Fig. 3.12.

4

Direct observation of temporal signaling variability in single bacteria

In this chapter, we describe measurements of temporal variability in the chemotaxis pathway activity of single wildtype *E. coli* cells. Gene expression noise is widely recognized as a source of variation across isogenic populations but biochemical reactions carried out by their protein products are also inherently stochastic and can generate additional variability in cell behavior. Such post-translational noise is expected to be particularly important for biochemical processes that play out in small volumes, such as the bacterial cell, but they have been challenging to address experimentally because they require single-cell measurements of interactions between small molecular populations. Using single-cell FRET, we found strong fluctuations of intracellular signaling in *E. coli* cells in the absence of gene expression changes, and obtained evidence that such signaling noise arises in the activity of adaptation enzymes. The typical fluctuation timescale of the intracellular signal was $\sim 10s$, which agrees well with those of previously reported fluctuations in flagellar motor behavior. Surprisingly, the noise amplitudes ($\eta \equiv \sigma_a / < a >= 0.44$) were on average substantially greater than previous theoretical estimates based on stochastic kinetics of the adaptation enzymes and was also found to vary considerably from cell to cell ($\sigma_\eta = 0.24$). While temporal noise in signaling circuits is commonly associated with information loss, our results suggest that having high noise levels in a fraction of cells may enhance foraging performance that is beneficial to the population of chemotactic cells.

This chapter is part of the publication: J.M. Keegstra, K. Kamino, F. Anquez, M.D. Lazova, T. Emonet and T.S. Shimizu. "Phenotypic diversity and temporal variability in a bacterial signaling network revealed by single-cell FRET" *eLife* **6**: e27455, 2017 [81]

4.1 Introduction

Signalling pathways are responsible for reliably transducing and processing information from the outside world to enable cells to make informed decisions, often using intricate webs of molecular interactions. Stochastic effects in such networks has been studied extensively in the context of gene expression [53, 55, 156], which often leads to heterogeneity in the abundance of network components within an isogenic population. Such heterogeneity in protein numbers can profoundly affect network-level behavior of signalling systems. Yet even in the absence of gene expression fluctuations, the stochastic interactions among the gene products, can also contribute additional variability to cell behaviors, but experimental dissection of such post-translational noise has been challanging to address experimentally. Here, we study how molecular noise arising in protein-protein interactions affect performance of the bacterial chemotaxis network, a canonical signaling pathway which controls the motile behavior of bacteria such as *E. coli*. In this network, sensory information processing leading to control of motor behavior is performed by an interaction network involving only protein molecules and operates on a timescale well separated from changes in gene expression. Importantly for our experiments, chemotaxis signaling and behavior remains functional under experimental conditions that do not permit growth or gene expression, as long as a metabolic energy source is provided. In fact, much of the molecular mechanisms underlying this pathway have been elucidated through experiments under such conditions, which allow for precise control of protein expression levels throughout the course of experiments. For an overview of these molecular mechanisms, see chapter 1 (and also refs. [37, 144, 213, 224]).

Theoretically, molecular noise arising in processes other than gene expression, such as protein-protein interactions within signaling pathways, can also contribute to cellular variability even in the hypothetical case that all cells share identical protein concentrations. However, such noise sources tend to be harder to study experimentally because, in contrast to gene-expression noise, which is readily characterized by measuring fluorescent reporter levels [55, 159], requirements for *in vivo* measurements of protein-protein interactions tend to be more demanding and no generically applicable strategies exist. The *E. coli* chemotaxis system provides a compelling experimental paradigm for addressing protein-signaling noise, because a powerful technique for *in vivo* measurements of protein signaling, based on Förster resonance energy transfer (FRET), has been successfully developed [190, 192]. However, in virtually all reported experiments using this technique, the signal was integrated over hundreds of cells, and thus uncorrelated temporal fluctuations in the activity of single-cells was averaged out. A pioneering study applied FRET at the single-cell level to study spatial heterogeneities in CheY-CheZ interactions [219], but those measurements were limited to relatively short times due to phototoxicity and bleaching. We have improved experimental

protocols to enable measurements of the FRET activity in single bacteria over extended (>1h) times (Chapter 2).

The chemotaxis protein signalling network controls the motile behavior of *E. coli* by modulating flagellar motor behavior. When the flagellar motors rotate in the same clockwise (CW) direction, the flagella form a bundle and the bacterium follows a relatively straight path (a "run"). When one of the motors steers the flagella in the counterclockwise (CCW) direction, the flagella bundle breaks up and the bacterium reorientates (a "tumble"). Previous experiments that relied on measurements of motor output [91, 126] did reveal slow steady-state fluctuations in the tumble rate of single cells that significantly increase the incidence of long CCW (run) events in the absence of stimulation with chemoeffectors. Based on analysis of genetic mutants, it was suggested that these slow fluctuations originate in the upstream signalling network, stochastic analysis of the signaling pathway dynamics implicated noise in the slow adaptation kinetics arising in the post-translational receptor modifications by the enzymes CheR and CheB [57, 91, 117]. These motor-switching fluctuations were found to be much smaller in the absence of (de)methylation activity [91], and a subsequent study showed that there is an intimate relationship between the adaptation time to applied stimuli and steady-state fluctuations in the absence of applied stimuli [143]. However, while these elegant motor-level experiments permitted indirect inferences about the origin of noise within the upstream molecular signaling process through the highly noisy motor dynamics, whose response properties can vary over time due to adaptive remodelling [237]. Measurements with a FRET reporter of kinase activity at the single-cell level would provide more direct observations of upstream signalling activity. Such would enable the comparisons of the intracellular signal against that at the level of motor-output, as well as against theoretical predictions [29, 57, 214].

The existence of slow fluctuations in signalling could have profound consequences for the motile behavior of bacteria that it controls. Because the tumble rate has a steep dependence on the response regulator CheY-P, [36, 236], moderate fluctuations in kinase activity (and hence CheY-P level) could lead to large fluctuations in tumble frequency [214], which means that the prevalence of long runs depends on the level of noise [91]. Whereas the situation without upstream signalling fluctuations would lead to an exponential run length distribution, the measured run lengths exhibited non-exponential heavy tails that were better described by a power-law distribution [91]. Elongated runs effectively transform a Brownian random walk into a Lévy walk, which is a much more efficient strategy for space exploration. Occasional long runs may be very useful when cellular resources are distributed in patches [223], and gradients are absent in a large fraction of space. However, the fluctuations in upstream signalling activity responsible for extending runs can also negatively impact the information transfer required to control motor behavior in response to stimuli. This means there could

be a trade-off between space exploration and precise signaling, rendering the signal noise level a critical parameter that tunes the cell's chemotactic phenotypes between these modes of behavior. The high throughput of single-cell FRET experiment opens the door to characterizing the diversity of noise statistics across individual cells within isogenic populations.

4.2 Results

Using our single-cell FRET protocol (described in chapter 2), we measured single cell activity time series over extended times using in the absence of attractant stimulation and found substantial differences between wildtype (CheRB+) and adaptation-deficient (CheRB-) cells in the variability of their FRET signals across time. The effect is clearly visible upon comparing long (∼1h) FRET time series obtained from cells of these two genotypes (Fig. 4.1). The FRET signal in wildtype cells demonstrated transient excursions from the mean level that were far greater in amplitude than those in CheRB- cells. To distinguish between

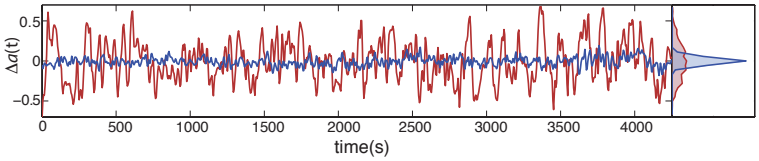

Figure 4.1: Temporal fluctuations in WT cells due to stochastic activity of adaptation enzymes CheR/CheB. Representative single-cell FRET time series of steady-state fluctuations $\Delta a(t) = a(t) - a_0$ in WT cells (VS115, red), together with analogous data from CheRB- cells (TSS58,blue) for comparison (low-pass filtered with a 10s moving average filter).

variability across cells in a population which in this thesis is described in terms of coefficients of variation, CV and that over time within a single cell, we denote the temporal noise amplitude as $\eta \equiv \sigma_a / a_0$, in which σ_a^2 denotes the variance of the temporal fluctuations in the activity a, and $a_0 = \langle a \rangle$ is the average steady-state activity level (e.g. activity in the absence of applied ligand stimulation). This amplitude was quantified by computing the variance of each single-cell time series, low-pass filtered with a moving average filter of 10s, and shows that the fluctuation amplitudes are much larger in wildtype cells compared to adaptation-deficient cells ($\langle \eta \rangle$ =0.44 and 0.09 respectively, Fig. 4.2a). These fluctuations were constant in amplitude over the course of the experiment (Fig. 4.2b). Importantly, these experiments were carried out under conditions in which no protein synthesis can occur due to auxotrophic limitation (see §2.2.1), thus ruling out gene-expression

processes as the source of these fluctuations.

The fluctuations in the FRET signal (as the standard deviation σ) is expected to scale linearly with $A_0/D_0\sqrt{1/D_0 + 1/A_0}$ if they are determined by experimental shot noise from the acceptor (A_0) and donor (D_0) fluorescence intensities (§4.4.1). The fluctuations σ_{TS} of CheRB+ cells did not show this linear relationship (Fig. 4.2c) but fluctuations in CheRB- cells did (Fig. 4.2d), indicating that the fluctuations arising in CheRB- cells are due to experimental shot noise from the fluorescence intensities A_0 and D_0. At high intensities, where shot noise diminishes, the noise magnitude η of a short (100s) segment of the unfiltered time series CheRB- cells still equals approximately 0.09 (as judged from the intersect of a linear fit with the yaxis in Fig. 4.2d, inset), indicating that in the unfiltered FRET signal of CheRB- the presence of other noise sources (apart from shot noise) has an upper limit of ~ 10%.

Power spectral density (PSD) estimates computed from such time series confirm a nearly flat noise spectrum for CheRB- cells, whereas CheRB+ cells demonstrated elevated noise at low frequencies (Fig. 4.3a). However, if the time series are averaged over the population before calculating the power spectrum, the difference disappears (Fig. 4.3b), demonstrating that the low-frequency fluctuations are uncorrelated across cells and can be resolved only in single-cell experiments. The amplitude of the low-frequency noise components cells do clearly vary from cell to cell, as can be gleaned in the diversity of single-cell power spectra (Fig. 4.3a). To quantify this protein-level noise due to CheR/CheB activity, we describe the fluctuating signal as an Ornstein-Uhlenbeck (O-U) process of the single variable a, with relaxation timescale τ and diffusion constant c, which can be interpreted as a linear-noise approximation [54, 221] to the multivariate stochastic kinetics of the underlying chemical network controling the mean kinase activity a [57, 214]:

$$\frac{da}{dt} = -\frac{1}{\tau_m} a(t) + \sqrt{c}\Gamma(t) \tag{4.1}$$

where $\Gamma(t)$ is a Gaussian white noise process. The parameters τ_m and c for each cell are readily extracted via the power-spectrum solution of the O-U process:

$$S_a(\omega) = \frac{2c\tau^2}{1 + (2\pi\omega\tau_m)^2} + E \tag{4.2}$$

where we have added to the standard Lorentzian solution [68] a white-noise term E that may vary from cell to cell to account for experimental shot noise in the photon-limited FRET signal. Single-cell PSD data were well fit by Eq. 4.2 (Fig. 4.4a and 4.5), and the average of extracted single-cell fluctuation timescales ($\langle\tau_m\rangle$ = 12.6s) (Fig. 4.4c) are in good agreement with previously reported correlation times of flagellar motor switching [91, 143], as well as the kinetics of CheRB-mediated changes in receptor modification from *in vivo* measurements using

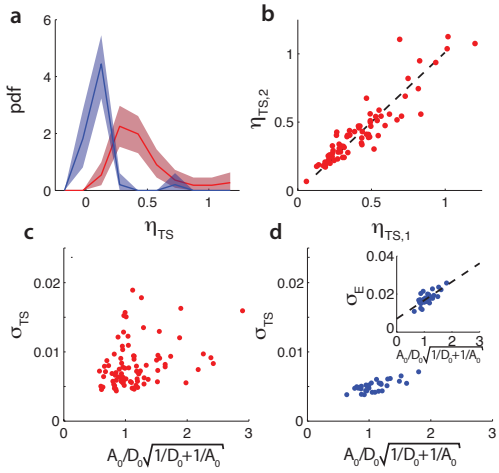

Figure 4.2: Differences in noise amplitudes between CheRB+ and CheRB- cells. **(a)** Histogram of fluctuation amplitude η ($\equiv \sigma_a/a_0$) for both WT (89 cells, red, from 3 independent experiments) and CheRB- (33 cells, blue, from two independent experiments), extracted from calculating the standard deviation of a low-pass filtered FRET time series over a 10s window divided by the mean FRET level of a single cell. Shaded areas represent 95% confidence intervals obtained from bootstrap resampling. **(b)** The noise amplitude of the first ($\eta_{TS,1}$) and second half ($\eta_{TS,2}$) of the time series show high correlation, indicating that fluctuations are constant throughout the experiment. All noise amplitudes are defined as coefficient of variance. Dashed black line indicates the diagonal. **(c)** Dependence of variance of fluctuations σ_{TS} for 89 WT cells , obtained from a 75 min long time series low-pass filtered over a 10s window, on acceptor (A_0) and donor (D_0) fluorescence intensities ($A_0/D_0\sqrt{1/D_0+1/A_0}$), both in arbitrary units. Correlation coefficient between the two distributions is 0.30 ± 0.21 (95 % obtained from bootstrapping). **(d)** Dependence of variance of fluctuations σ_{TS} of 33 CheRB- cells, on acceptor (A_0) and donor (D_0) fluorescence intensities ($A_0/D_0\sqrt{1/D_0+1/A_0}$), both in arbitrary units. Correlation coefficient between the two distributions is 0.71 ± 0.18 (95 % obtained from bootstrapping). Inset: same as main panel, but then fluctuations σ_E calculated as the average standard deviation of three short segments of unfiltered data. The dashed black line represents a linear fit to the data, with slope $9.7{\cdot}10^{-3}$ and offset $7{\cdot}10^{-3}$

radioactively labeled methyl groups [111, 208]. The variance of the fluctuations obtained from the fits of the PSD, $\sigma_a = \sqrt{c\tau_m/2}$ yielded very similar noise amplitudes $\eta_{OU} \equiv \sigma_{a,OU}/a_0$ as calculated from the time series ($\langle\eta_{OU}\rangle = 0.42$, Fig. 4.4b). We note that these noise levels are larger than expected - in a considerable fraction of cells, the standard deviation of fluctuations is comparable to the mean level of activity, and the steady-state fluctuations span the full range of kinase activity (see e.g. that represented by the red curve in Fig. 4.1), but the noise levels are reprodicible between cells grown in a different culture (Fig. 4.6). Previous studies had predicted a value of $\sim 10-20\%$, based either on reported fluctuation amplitudes of motor switching [91, 214] or biochemical parameters of the intracellular signaling network [57, 183] and is also highly variable ($CV = 0.55$,$\sigma_\eta = 0.24$) from cell to cell. What is causing the large cell-to-cell variability in fluctuation amplitudes? Cell-to-cell variation in CheR/CheB ratio generates diversity in the steady-state activity a_0 (see chapter 3) and fluctuation amplitude is predicted to be directly related to the steady-state activity level [29], with zero noise amplitudes at the extreme values ($a_0 \approx 0$ and $a_0 \approx 1$). Indeed, the noise amplitudes in our experiments seemed to be higher at intermediate activity levels (Fig. 4.4e) but even at intermediate activity levels there is large variability between cells. A plausible interpretation of these differences in noise amplitudes could be caused by cell-cell differences in CheR and CheB (CheR+CheB, with constant CheR/CheB ratio). Such variation would lead to different adaptation kinetics at the same steady-state activity level.

In summary, we confirmed the presence of strong temporal fluctuations in single-cell chemotaxis signaling attributable to the stochastic kinetics of the adaptation enzymes CheR/CheB, and further found that the amplitude of these fluctuations was much larger than expected and vary considerably across cells in an isogenic population.

4.3 Discussion

In addition to phenotypic diversity in signaling parameters explored in chapter 3, single-cell FRET has allowed us to resolve temporal fluctuations in signaling about the steady-state output within individual cells. In wildtype cells, we found that the steady-state activity fluctuates slowly (Fig. 4.3, correlation time $\tau \sim 10$ s) with a large amplitude ($\eta \approx 40\%$), but this amplitude also varies significantly from cell to cell ($CV \approx 0.6$). Fluctuations on this timescale were absent in CheRB- cells defective in receptor methylation/demethylation, indicating that these fluctuations are generated by stochastic processes in the activity of the adaptation enzymes CheR and CheB. Whereas the fluctuation correlation time τ in our FRET experiments was in close agreement with those from previously reported flagellar motor switching experiments [91, 143], the fluctuation amplitude

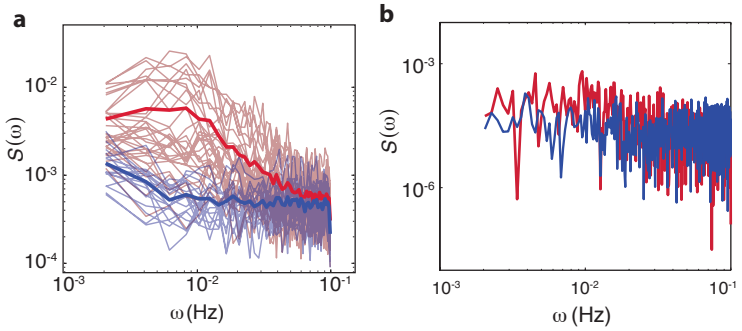

Figure 4.3: Slow temporal variability of network activity due to stochastic activity of adaptation enzymes CheR/CheB. **(a)** Power spectral density (PSD) computed from single-cell FRET time series of 31 WT cells (red, from single experiment) and 17 CheRB- cells (blue, from single experiment). Thin curves in the lighter shade of each color represent single-cell spectra, and their ensemble average is shown as thick curves in a darker shade. **(b)** The increased power at low-frequencies in WT cells in panel (a) was lost when PSD was computed after ensemble-averaging the time series, indicating that these slow fluctuations are uncorrelated across cells.

$\langle\eta\rangle \approx 40\%$ was surprisingly large. Theoretical analysis of the motor-based noise measurements indicated that, in the frequency range of our experiments, stochastic methylation kinetics are indeed the dominant source of noise [34]. Another theoretical study of the motor noise [214], had predicted a modest noise level of intracellular noise, with a lower bound of 20% of the mean. The discrepancy is likely due, at least in part, to the recently discovered adaptation at the level of the flagellar motor [237], which must effectively act as a high-pass filter that attenuates frequencies near or below a cutoff frequency determined by its own characteristic timescale for adaptation. The fluctuation amplitude η was also much greater than previous estimates from pathway-based models [57, 183]. In the next chapter, chapter 5, we show that there is an additional noise source, independent of methylation, which contributes to the total noise amplitude in wildtype cells and not considered in previous modeling efforts.

The large temporal noise we observed in wildtype (CheRB+) cells may seem counterintuitive, given that the chemotaxis pathway is a transduction path for sensory information, and noise generally reduces information transmission capacity of communication channels [177]. However, the chemotaxis signaling pathway is not only a sensory system but also a control circuit for motile behavior, and recent studies have highlighted the importance of considering the behavioral context in understanding the design of this signaling pathway [49, 108, 229]. The temporal noise we observed could have profound implications for *E. coli*'s

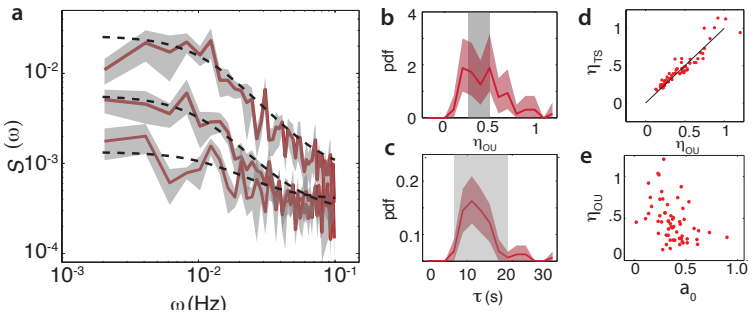

Figure 4.4: Fluctuations in WT cells due to stochastic activity can be well described by an Ornstein-Uhlenbeck (O-U) process. **(a)** Representative single-cell PSDs and fits by an O-U process. Shown are O-U fits (Lorentzian with constant noise floor; dashed curves) to three single-cell PSDs (solid curves). Shaded areas represent standard errors of the mean for PSDs computed from nine non-overlapping segments of each single-cell time series. Fits to all cells from the same experiment are shown in (Fig. 3.5). **(b)** Histogram of fluctuation amplitiudes computed from the O-U fit parameters. The gray shaded region indicates the variability (mean±std) that can be explained by experimental noise and a finite time window, obtained from simulated O-U time series (see §4.4.2). **(c)** Histogram of fluctuation timescales τ extracted from O-U fits to single-cell PSDs (red, 75 out of 89 cells). Cells without a clear noise plateau at low frequencies were excluded from the analysis. Red shaded region represents 95% confidence intervals obtained from bootstrap resampling. The gray shaded region indicates the variability (mean±std) that can be explained by experimental noise and a finite time window, obtained from simulated O-U time series (see §4.4.2). **(d)** Noise amplitudes computed from the O-U fit parameters (panel b) demonstrate excellent agreement with those computed directly from the time series (panel b). **(e)** Noise amplitudes computed from the O-U fit parameters are highest at intermediate steady-state activity levels a_0.

random-walk motility strategy, because slow fluctuations in the intracellular signal can enhance the likelihood of long run events and stretch the tail of the run-length distribution to yield power-law-like switching-time distributions over a range of time scales [91, 214]. Such non-exponential statistics are known to yield superior foraging performance in environments where resource distribution is sparse [223], and temporal fluctuations in run-tumble behavior has also been shown theoretically to enhance climbing of shallow gradients by generating runs that are long enough to integrate over the faint gradient a detectable difference in ligand input [63, 189]. Hence, the noise generated by the adaptation system can be advantageous in resource-poor environments (*deserts*) in which efficient exploration of space for sparsely distributed sources (*oases*) is of utmost importance. By contrast, strong temporal noise clearly degrades response fidelity in rich environments where the

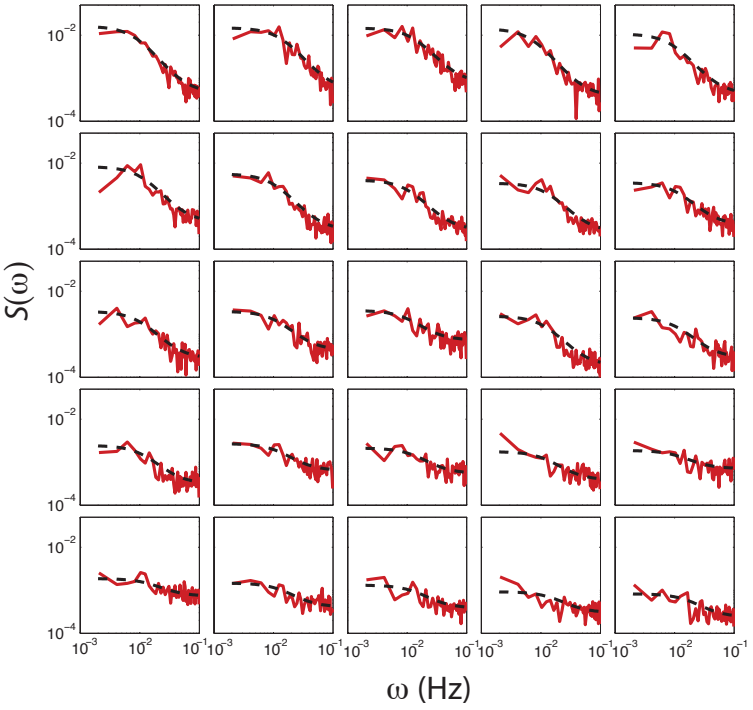

Figure 4.5: PSD estimates obtained from single-cell FRET time series (red dashed curve) with fits of O-U process to PSD estimates to 25 out of 31 cells (black dashed curve) from a single experiment shown in Fig. 4.3a. The cells are sorted by variance calculated from the fit ($c\tau/2$), with top-left having the highest. Cells without a clear low frequency plateau, higher than five times the standard deviation of the high frequency noise, were excluded from the analysis.

gradient signal is strong enough for detection with short runs, and might also complicate coordination of cells in collective behaviors such as the aforementioned traveling-wave exploitation of nutrients. Our finding that the noise amplitude varies strongly from cell to cell thus suggests that isogenic populations might be hedging their bets by partitioning themselves between specialists for local exploitation of identified resource patches and those for long-range exploration in search for new ones.

A promising direction for future studies are the mechanism(s) responsible for the large cell-to-cell variability we observed in the noise amplitudes (η). We have shown that even at the same steady-state activity level, noise levels of single cells are diverse (Fig. 4.4e). A plausible hypothesis is that the differences in noise

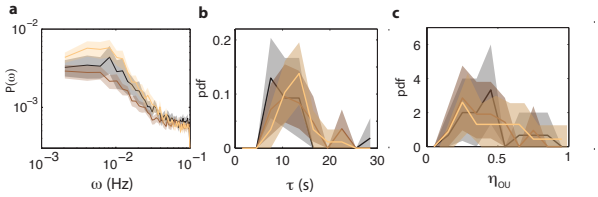

Figure 4.6: Temporal fluctuations in WT cells is reproducible across experimental days. **(a)** Power spectrum density estimates for three independent experiments on CheRB+ cells (VS115), each based on 29 (gold), 28 (brown) and 18 cells (black). Shaded areas represent 95 % confidence intervals (2 s.e.). **(b)** Fluctuation timescale τ obtained from fits of Ornstein-Uhlenbeck process to single-cell power spectra. **(c)** Noise amplitude η_{OU} for the three different experiments.

levels levels are caused by differences in the total expression levels of adaptation enzymes (CheR+CheB, with constant CheR/CheB). Experiments performed at the output of the chemotaxis pathway, have indicated that there is an intimate relationship between cellular fluctuations and response [143], which in the case of our FRET experiments would correspond to a correlation between recovery time and noise amplitude. However, due to the limited experimental duration of FRET experiments, it is hard to measure adaptation kinetics and noise levels in the same cells. Alternatively, one could artificially control the levels of CheR and CheB and measure the adaptation kinetics and noise characteristics separately for different expression levels of the adaptation enzymes. In an appendix to this chapter, section 4.5, we have described the successful tuning of adaptation time at (approximately) constant steady-state kinase activity levels by expressing CheR and CheB from a construct in which the CheR and CheB expression was transcriptionally coupled. These results could facilitate further explorations of the relationship between adaptation kinetics and activity fluctuations.

Large fluctuations in kinase activity with subsecond timescales, leading to wave-like propagation of CheY-P level through the cytoplasm, have been proposed to explain synchronized switching behavior of flagellar motors [120, 207], but these fluctuations have never been measured and their presence is disputed. An alternative hypothesis claims the cause of the interactions could be the hydrodynamic coupling of the flagella [75], but this model cannot easily explain why the flagella correlation disappears when a constitutively active CheY is expressed, and why two motors in close proximity but attached different cells do not show synchronized switching [67]. Yet the flagella synchronisation by CheY-P variability is hard to explain quantitatively, despite assuming quite exotic parameters for the noise amplitude [75]. Could single-cell FRET resolve this debate (as is suggested by Mears and colleagues [120])? The lower limit to

the timescales observable by single-cell FRET that of CheY-CheZ interactions, which at ~100-500 ms [191] is on the same order as the timescale of the CheY-P fluctuations conjectured by these authors and on a much faster timescale compared to the experiments described in this chapter. However, if another source of fluctuations would be present, one would expect the presence of a second knee at higher frequencies in the power spectrum (Fig. 4.3). However, from the noise magnitude at high frequencies we estimated the residual noise (the approximate noise value of non-adapting cells at zero shot noise, Fig. 4.2d) to be less than 10 %, insufficient to coordinate the switching of multiple flagella [75]. Of course, it may be that this additional noise source, if present, only manifests itself at intermediate activity and is suppressed in phenotypes with extreme activity levels (e.g. a ≈ 0 or 1), or that the spectral properties of this noise process are very different compared to O-U process. The amplitude of of fast fluctuations in CheY-P concentration, and the cause of synchronized motor switching, should be a topic for future studies.

In summary, we have measured fluctuations of signaling activity due to stochastic activity of the adaptation enzymes CheR and CheB and observed considerable diversity in noise levels between cells. These results show that diversity of temporal variability noise amplitudes may be subject to selection and high noise levels in a fraction of a chemotactic population of cells may be beneficial for the population as a whole.

4.4 Materials and Methods

4.4.1 FRET experiments

FRET experiments are performed as described in chapter 2, which includes a list of the strains and plasmids used in this study (§2.4).

Dependence of experimental noise in FRET on fluorescence intensity

The standard deviation in $R = A/D$ for two uncorrelated variables A and D equals

$$\frac{\sigma_R}{R} = \sqrt{\left(\frac{\sigma_D}{D}\right)^2 + \left(\frac{\sigma_A}{A}\right)^2} \tag{4.3}$$

since small changes in ratio are proportional to changes in FRET (Eqn. 2.4, [192]) and if both A and D are limited by shot noise one expects the following relation for the experimental noise σ_{E}:

$$\sigma_{\mathrm{E}} \propto \sigma_R = R\sqrt{1/D + 1/A} \tag{4.4}$$

in which the experimental noise σ_{EXP} is defined as average standard deviation of the (unfiltered) FRET signal over three short (100s) segments at the start of the

FRET experiment.

4.4.2 Power Spectral Density Estimates

From FRET time series of length T and acquisition frequency f (0.2 Hz for the experiments in this chapter)we calculated Power Spectral Density (PSD) estimates as

$$S_{\mathrm{FRET}}(\omega) = \frac{1}{T}|\mathscr{F}(\omega)|^2 \tag{4.5}$$

where $\mathscr{F}(\omega)$ is the (discrete-time) Fourier transform of the zero-mean FRET time series FRET(t). We only consider positive frequencies and multiply by two to conserve power.

To study the influence of experimental noise and the effect of estimating τ and c (Eqn. 4.1) from a finite time window, we generated O-U time series using the update formula [68]

$$X(t+\Delta t) = X(t) - \tau^{-1}\Delta t + c^{1/2} n(\Delta(t))^{1/2} \tag{4.6}$$

in which n denotes a sample value from a normally distributed random variable ($\mu = 0, \sigma = 1$). To the generated time series Gaussian white noise was added to simulate experimental noise. The experimental noise amplitude was obtained from the average power at high frequencies (0.09-0.1 Hz).

4.5 Appendix: independent control of a_0 and adaptation kinetics

The noise amplitudes of temporal fluctuations of kinase activity varies greatly from cell to cell, even with the same activity bias (Fig. 4.2). Since the fluctuations are clearly dependent on the activity of the adaptation enzymes CheR and CheB, one possibility is that differences in the total expression levels of CheR and CheB (CheR+CheB, with constant CheR/CheB ratio) could cause the diversity in noise amplitudes. This section shows some preliminary data on controling the adaptation timescale by tuning the expression of the adaptation enzymes, which may be useful for future experiments trying to establish a relationship between adaptation kinetics and noise level.

We expressed the adaptation enzymes from a single transcriptional unit (i.e. a polycistronic operon) placed on an inducible plasmid expression vector, with the aim of tuning the total expression level (CheR+CheB) while maintaining the average ratio (CheR/CheB) constant. We tested several constructs expressing CheR and CheB, using different combinations of plasmid backbones (pKG116 and pBAD33) and the presence or absence of the native ribosome binding site

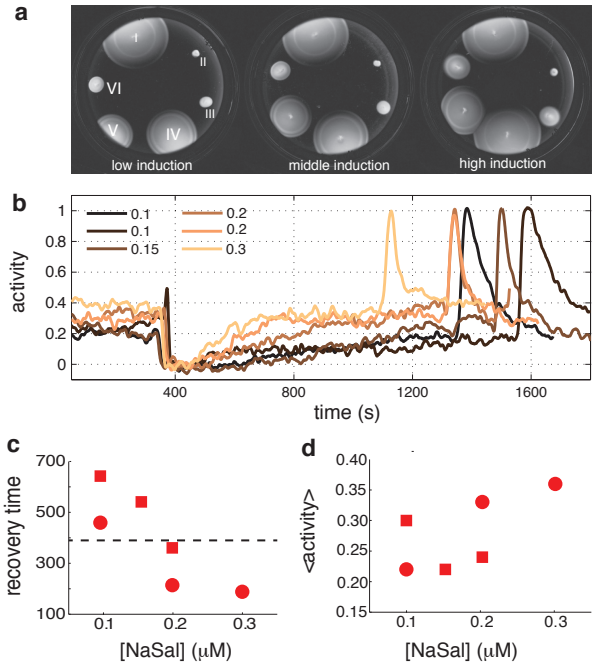

Figure 4.7: Tuning the adaptation kinetics of the bacterial chemotaxis system. **(a)** Comparing the chemotaxis performance on soft-agar of different constructs expressing CheR and CheB in tandem, from a single plasmid with inducible promotor. Shown is result after 10h of growth at 33.5 C without induction (left panel), 0.2 μM NaSal and 10^{-5}% arabinose as inducers (middle) and 0.4 μM NaSal and 10^{-4}% arabinose as inducers (right). Order of the strains is the same in all thee plates: (I) Wildtype (RP437/pKG116) (II) Non-adapting negative control (CheRB-, VS149/pBAD33) (III) CheRB+ from pBAD33 plasmid (TSS744/pSJAB37) (IV) CheRB+ from pKG116 plasmid (TSS744/pSJAB149) (V) CheRB+ from pKG116 plasmid with native RBS (TSS744/pSJAB148) (VI) CheRB+ from pBAD33 plasmid with native RBS (TSS744/pSJAB147). **(b)** Population-averaged FRET time series obtained from cells expressing CheRB+ from an inducible pKG116 plasmid (TSS1845/pSJAB149) with different inducer levels and responding to the addition and removal of 500 μM MeAsp. The time series are aligned horizontally to the attractant addition response, and all time series are normalized to the maximum FRET response when responding to the removal of attractant. The inducer concentration of NaSal (μM) is indicated with the same color as each time series. **(c)** Recovery timescale defined as the time required to recover 50% of the activity after the attractant addition response, as a function of induction level, from the time series shown in panel (b). The red circles and squares indicate experiments performed on the same day and grown from the same saturated overnight culture (See §2.2.1). Black dashed line indicates approximate wildtype recovery level. **(d)** Steady-state activity level a_0 before addition of attractant, as a function of induction level, from the time series shown in panel (b).The red circles and squares indicate experiments performed on the same day and grown from the same saturated overnight culture.

[RBS]. We tested performance in soft agar of *cheR cheB* cells complemented with these expression vectors to determine the best combination of vector and inducer level to match cells with wildtype expression levels of CheR and CheB. We found that expressing CheRB from a pKG116 backbone with the RBS of the expression vector (pSJAB149) and gene product performed better than alternative constructs with different backbone and/or RBS (Fig. 4.7a). We then measured the population-FRET response of cells with CheR and CheB expressed from this plasmid in *cheR cheB* background (TSS1845/pSJAB149) with different induction levels of sodium saliculate [NaSal] (Fig. 4.7b). We found that with increasing induction level, the recovery time of the activity after the addition of a 500 μM stimulus to 50 % of the prestimulus value decreased, with low levels of induction showing slower adaptation kinetics and higher induction faster adaptation kinetics compared to WT cells (Fig. 4.7c). Since the chemoreceptors are more than tenfold more abundant than the adaptation enzymes [102], and hence the adaptation kinetics should change if the adaptation enzymes are expressed differently. We also noted that the actual value of the adaptation time varied from day to day, probably due to subtle differences in growth conditions that affect the plasmid-based expression. The steady-state activity level also demonstrated considerable day-to-day variation, but increased mildly on average with induction (Fig. 4.7c). (We note, however, that this trend was not consistent across experiments performed on the different days). Interestingly, in a recent study in which CheR and CheB were expressed from two different plasmids, it was found that the steady-state tumble frequency of cells was not constant around wildtype CheR and CheB levels (~ 100) [49], contrary to the expectation of many current models of sensory adaptation which predict that the steady-state kinase activity level depends only on the abundance ratio of the adaptation enzymes [10, 183]. Although we do not have a mechanistic understanding of the relation between CheR-CheB expression level and steady-state kinase activity, we note that even if these FRET experiments show a constant average a_0 for a large range of induction concentration, within a population there will be diversity in steady-state activity level.

The average signal-to-noise ratio [SNR] of these cells expressing CheR and CheB from a plasmid — in which SNR is defined as the change in acceptor-donor fluorescence ratio due to FRET divided by the standard deviation of fluctuations in the ratio, see §2.2.2 — of these plasmid-expressing CheRB (in TSS1845, which expresses FliC* from the chromosome) is 3.9 ±1.6, while cells expressing CheRB from the chromosome (FliC* from plasmid ZR1) under the same experimental conditions this yields ~7.5, nearly two fold higher. The difference is likely due to flagella-mediated enhanced secretion of FlgM in cells expressing FliC* from a plasmid, which likely increases the expression levels of all chemotaxis enzymes (see chapter 2). The limited SNR of cells expressing CheRB from a plasmid makes measurements of temporal fluctuations in cells with controled levels of CheR and CheB an interesting challenge for future experiments.

5

Stochastic two-state switching in chemoreceptor activity

In this chapter, we describe experiments that reveal stochastic switching of chemoreceptor arrays in the absence of adaptation kinetics. Two-state switching of proteins between contrasting activity states is a cornerstone of biochemical modeling. Yet, direct experimental observation of the dynamics of such switches has been rare, especially *in vivo*. We present the first direct observations of two-state switching in a canonical protein signaling complex, the bacterial chemoreceptor array, by FRET measurements in single *E. coli* cells. Cells with homogeneous arrays consisting of only a single chemoreceptor species exhibited giant fluctuations often between multiple discrete levels of signal activity, which we observed in the presence of sub-saturating concentrations of ligand. In a chemoreceptor mutant with intermediate activity bias, we observed similar behavior in the absence of applied ligand. In a sizeable minority of the population, fluctuations were dominated by switches between the two extreme states of maximum and zero activity. The rather slow typical timescale of these switches ($\sim$ 100 s) likely reflects the large size of the cooperatively switching array of chemoreceptor-kinase complexes, which are estimated at $\sim$1000 allosteric units. These discrete-level fluctuations suggest that the cooperativity of chemoreceptor arrays in some cells could be much larger than previously estimated, and a preliminary characterization of switching time distributions raise the intriguing possibility that chemoreceptor activity is might involve one or more dissipative (non-equilibrium) processes

The first part (Figures 1-3) of this chapter have been published in: J.M. Keegstra, K. Kamino, F. Anquez, M.D. Lazova, T. Emonet and T.S. Shimizu. “Phenotypic diversity and temporal variability in a bacterial signaling network revealed by single-cell FRET" *eLife* **6**: e27455, 2017 [81]

5.1 Introduction

Two-state models play a prominent role in the theoretical analyses of biochemical systems, providing a simple means of relating experimentally observable continuous variables (such as enzyme activity) to the statistical mechanics of underlying molecular states. However, the motivation for modeling a system as two-state is most often parsimony (Occam's razor), and whether or not the underlying molecular processes actually involve transitions between discrete states is actually unresolved in most cases. Experimental observation of two-state switching dynamics can be challenging because discrete transitions are averaged away in typical ensemble-averaged measurements, but has been achieved *in vitro* in single molecule experiments, as well as in *in vivo* in some compact molecular assemblies comprising up to a few dozen molecular components, such as the opening and closing of ion channels [82], and CW/CCW rotational switching of the bacterial flagellar motor [8]. Here, we report stochastic two-state switching behavior in the activity of bacterial chemosensory arrays, extensive molecular assemblies comprising ~1000 protein subunits in each cell.

Chemoreceptor arrays are the central signal processing entity consisting of thousands of chemoreceptors, kinases and scaffolding molecules, that enable motile bacteria such as *E. coli* to sense and respond to their chemical environment. The most successful models describing the ligand response and sensory adaptation of this receptor-kinase complex are based on two-state allosteric transitions [7, 85, 123, 215]. Previous population-level FRET measurements [183, 192, 193] could be fit consistently with two-state models, but these measurements were unable to resolve two-state transitions directly. Moreover, the cooperativity inferred from population-averaged dose response curves only provides a lower bound to the true cooperativity of single cells, because of potential cell-to-cell variation in cellular sensitivity (defined as the stimulus size that yields half-maximum response). Single-cell experiments thus have the potential to reveal whether the underlying molecular transitions are actually two-state, and provide more accurate estimates of cooperativity in single-cells. Unlike averaged signals (either in time or over a population), stochastic single-cell time series are a useful tool to discriminate between different models. Especially the difference between non-equilibrium or equilibrium descriptions is often hard to resolve in ensemble averages, but have clearly distinct statistical signatures [212].

We developed an *in vivo* single-cell assay of signaling dynamics in bacteria by measuring the FRET between two fluorescent proteins, mRFP1 and YFP, fused to respectively the response regulator CheY and its phosphatase CheZ. The FRET signal is proportional to the activity a of kinase CheA, the output parameter of the chemoreceptor arrays (see Chapter 2). Using this single-cell FRET assay, we reported the presence of large ($\eta \equiv \sigma_a / \langle a \rangle \approx 45\%$) variability in time of the kinase activity of wildtype (CheRB+) cells due to stochastic kinetics of chemoreceptor

methylation and demethylation by the adaptation enzymes CheR and CheB (see Chapter 4). Although the activity fluctuation amplitude was large and in some cells spanned the full range (0 to 1) of kinase activity a, the fluctuations did not include discrete transitions and could be well described as an continuous Ornstein-Uhlenbeck stochastic process with a characteristic timescale $\tau \approx 10s$. The fluctuation amplitude η of cells in the presence of adaptation enzymes was much greater than previous estimates from pathway-based models that considered sublinear kinetics in the enzymatic activities of the adaptation enzymes [57] and receptor cooperativity [183] as possible mechanisms that amplify noise originating in the stochastic kinetics of receptor methylation/demethylation. A possible explanation for this discrepancy between expected and measured noise amplitudes is the presence of one or more additional noise source(s) independent of methylation/demethylation dynamics, an hypothesis which is investigated (and confirmed) in this chapter.

5.2 Results

5.2.1 Fluctuations independent of the adaptation system

By observing fluctuations in single-cell kinase activity using single-cell FRET, we found that the noise amplitude η was much lower than wildtype (CheRB+) in non-adapting (CheRB-) cells (Chapter 4, and Fig. 5.1b). Yet it is possible that the strong activity bias of adaptation-deficient cells cells in the absence of chemoeffectors ($a_0 \approx 1$) masks noise contributions that would be observable if receptors were tuned to the more responsive regime of intermediate activity (e.g. as in wt cells, where $a_0 \approx 1/3$). We reasoned that in CheRB- cells, tuning the activity to an intermediate level by adding and sustaining a sub-saturating dose of attractant could reveal additional noise sources. Hence we measured the temporal variability of CheRB- cells during prolonged stimulation with 50 μM L-serine, which elicits a half-maximal population-level response (Fig. 5.1a). Although no large fluctuations were be observed in the population-averaged time series (Fig. 5.1a), averaging the power spectra computed from all single-cell time series revealed a somewhat elevated noise level at low frequencies, compared to the case without ligand (Fig. 5.1b). These results indicate the presence of a noise source independent of receptor methylation.

5.2.2 Giant fluctuations in homogeneous chemoreceptor arrays

To test whether and how these methylation-independent fluctuations are affected by the composition of the chemoreceptor arrays, we also measured the response

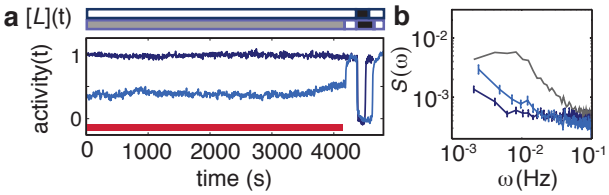

Figure 5.1: Temporal fluctuations in adaptation-deficient cells at intermediate activity levels. **(a)** (Top) Stimulus protocol for modulation of the L-serine ligand concentration ($[L](t)$). Cells were incubated either in buffer ($[L] = 0$, white) or a subsaturating stimulus ($[L] = 50\mu$M, gray) for > 1 hr. A saturating stimulus ($[L] = 1$mM, black) is applied at the end of the experiment. (Bottom) Population- averaged time series for adaptation-deficient cells with wildtype receptor complement (CheRB-, TSS58) for experiments with (18 cells, light blue) and without (17 cells, dark blue) a sustained 50 μM L-serine stimulus during the time interval used to compute the PSDs in panel a (indicated by the red bar). **(b)** Power spectral density (PSD) for temporal signal fluctuations during sub-saturating ligand stimulation of 18 cells with wildtype receptor complement (light blue, CheRB-, TSS58) and of 17 cells of the same genotype but for signal fluctuations observed in the absence of stimulation. Also shown, for comparison, are PSDs from experiments for WT (CheRB+) cells (gray, see Fig. 4.3)). Error bars represent standard error of the mean.

of CheRB- cells expressing Tsr as the sole chemoreceptor during a sustained stimulus of magnitude close to the population-level K (Fig. 5.2). Strikingly, the time series of single-cell responses demonstrated strong deviations from the population average (Figs. 5.2b). Whereas all cells responded identically to the saturating dose of attractant, their behavior during the sub-saturating step was highly diverse. Some cells (11/141) demonstrated no apparent response in kinase activity, whereas in others (32/141) complete inhibition was observed (Fig. 5.2, yellow curves). The majority of cells (98/141), however, had an intermediate level of activity when averaged over time, but demonstrated strong temporal fluctuations, often with magnitudes exceeding those observed in wildtype (CheRB+) cells.

We further noted that within this subset of cells with large temporal fluctuations, a large fraction (54/98) demonstrated fluctuations that resemble rapid step-like transitions between discrete levels of relatively stable activity that could be identified as peaks in the distribution of activity values across time (Fig. 5.2b, marginal histograms). Among these "stepper" cells, the majority (37/54) appeared to transition between 3 or more discrete activity levels (Fig. 5.2b, brown curve), whereas the remaining sizable minority of steppers (17/54) demonstrated binary switching between two discrete levels corresponding to to the maximum ($a \approx 1$) and minimum ($a \approx 0$) receptor-kinase activity states (Fig. 5.2b. red curve). The remaining fraction of cells (44/98) demonstrated fluctuations that were also often large but in which discrete levels could not be unambiguously assigned (Fig. 5.2,

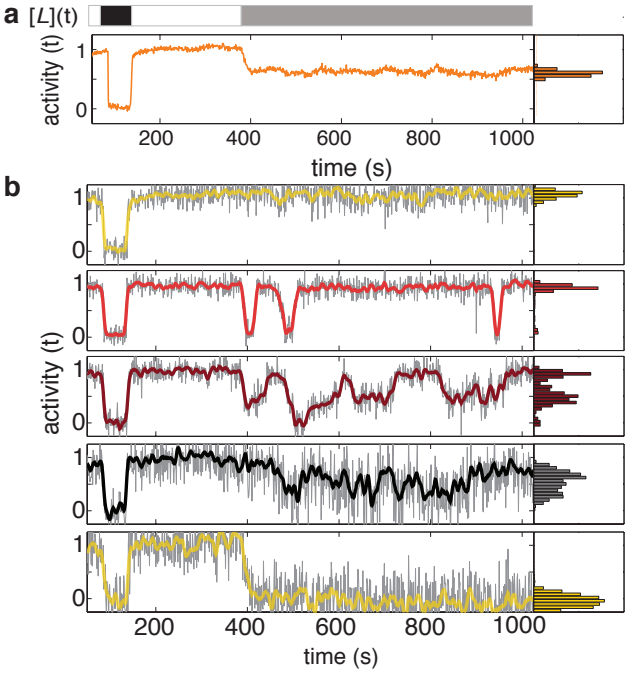

Figure 5.2: Giant temporal fluctuations in adaptation-deficient cells with homogeneous chemoreceptor composition. **(a)** (Top) Stimulus protocol for L-serine concentration ($[L](t)$). At the start of the experiment, a saturating concentration ($[L]$ = 1mM, black) is applied for a short time. After flushing buffer ($[L] = 0$, white), an intermediate concentration ($[L] = 25\mu$M, gray) is sustained for ~10 minutes. (Bottom) Population-averaged time series of 58 adaptation-deficient cells expressing Tsr as the sole chemoreceptor (RB-Tsr+; TSS1964/pPA114) under the stimulus protocol indicated above. **(b)** Selected single-cell time series of the population shown in panel (a), each normalized to its activity level before adding the first stimulus. To the unfiltered data (gray) a 7s moving average filter is applied and superimposed (colored according to categories in Fig. 5.3a).

black curve). The numbers of cells corresponding to each of the categories described above are summarized in Fig. 5.3a.

5.2.3 Stochastic two-state switching of chemoreceptor array activity

The observation of cells that demonstrate spontaneous two-level switching is particularly surprising, given the large number of molecules involved in receptor-kinase signaling. The expression level of each protein component of the chemoreceptor-CheW-CheA signaling complex in our background strain (RP437) and growth medium (TB) has been estimated (by quantitative Western Blots) to be of order 10^4 copies/cell [102]. Considering that the core unit of signaling has a stoichiometric composition of receptor:W:A = 12:2:2 (monomers) [104], the number of core units is likely limited by the number of receptors, leading to an estimate $10^4/12 \sim 10^3$ core units for a typical wildtype cell. This estimate does not apply directly to the experiments of Fig. 5.2 because receptors are expressed from a plasmid in a strain deleted for all receptors. But the FRET response amplitudes of these cells were similar to those of cells with a wildtype complement of receptors [193], and we thus expect the number of active core units per cell in the experiments of Fig. 5.2 to be similar to or greater than that in wildtype cells.

We analyzed further the temporal statistics of the discrete transitions in the subset of cells exhibiting two-level switching (Fig. 5.3). We first quantified the duration of such transitions by fitting segments of the activity time series over which these switches occured (Fig. 5.2b) by a symmetrized exponential decay function (see §5.4.2) to obtain switch durations τ_+ and τ_- for upward and downward transitions, respectively. The fitted values for τ_+ and τ_- correspond to the duration over which the activity trajectory traverses a fraction $1 - e^{-1}$ of the transition's full extent, and were found to be similar between switches in both directions: $\langle\tau_+\rangle \pm \sigma_{\tau_+} = 4.2 \pm 2.2$ s and $\langle\tau_-\rangle \pm \sigma_{\tau_-} = 3.5 \pm 3.2$ s (Fig. 5.3c). We note that these transition times are significantly greater than, but close to, the data acquisition interval (1 s), and so the shape of the fitted function should be considered a first approximation to the true rise and decay dynamics.

We then considered the duration of time between switching events. We defined $\Delta t_{\mathrm{up,k}}$ and $\Delta t_{\mathrm{down,k}}$ as the duration of the k-th time interval between transitions with high- and low-activities, respectively (Fig. 5.3b), and computed the average over all k of $\Delta t_{\mathrm{up/down,k}}$ for each individual cell to estimate its residence timescales $\tau_{\mathrm{up/down}}$ for states of high/low activity, respectively. From each cell's set of intervals $\{\Delta t_{\mathrm{up/down,k}}\}$ we also computed a parameter $a_{1/2}$, defined as the fraction of time the cell spent in the high activity level, as a measure of its time-averaged activity during the sub-saturating (20μM) L-serine stimulus that yielded a population-averaged response $\langle a\rangle \approx 1/2$ (see Measuring FRET in single

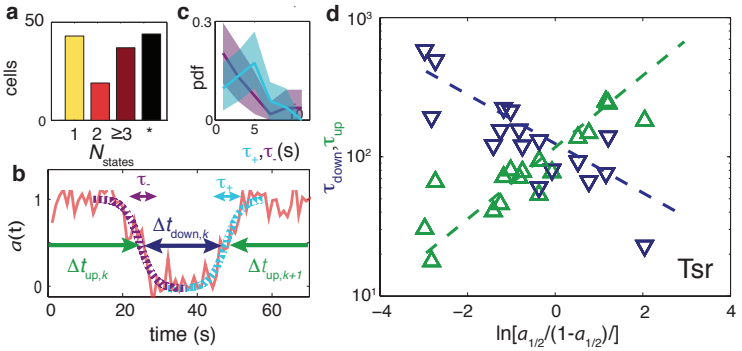

Figure 5.3: Analysis of cells showing two-state switching as a simple barrier-crossing process. **(a)** Classification of RB-Tsr+ single-cell fluctuation phenotypes by the number of stable activity levels observed during the sustained subsaturating stimulus. Many cells show only one stable activity level (yellow), corresponding to either full-amplitude response ($a \to 0$) or no response ($a \to a_0$). Some cells show two (red) or more (purple) apparently stable states. In other cells, fluctuations appeared chaotic with no discernibly stable state (black). **(b)** Definitions for analysis of two-state switching dynamics. The transition timescales τ_+ and τ_- were determined by fits of a symmetric exponential function (see main text) to the upward (cyan) and downward (purple) switching transients, respectively. Residence times $\Delta t_{\mathrm{up,down}}$ were defined as the interval between two successive transitions, at 50% activity. **(c)** Histogram of transition timescales, τ_+ (4.2 ± 2.2s, 26 events, cyan) and τ_- (3.5 ± 3.2, 29 events, purple) from 10 two-state switching cells of a single experiment with 1 Hz acquisition frequency. **(d)** Mean residence times τ_{up} and τ_{down} for two-state switching cells as a function of the average activity bias $\ln[a_{1/2}/(1-a_{1/2})]$. The slopes are $\gamma_{\mathrm{down}} = -0.4 \pm 0.1$ and $\gamma_{\mathrm{up}} = 0.6 \pm 0.1$, and the crossover point at $\tau_{\mathrm{up}} = \tau_{\mathrm{down}} = 110 \pm 10$ s defines a characteristic switching timescale. Data of 17 cells from 3 independent experiments (one at 1 Hz acqusition, two at 0.2 Hz acquisition).

bacteria).

We found that the logarithms of the mean residence times τ_{up} and τ_{down} scale approximately linearly with $\ln[a_{1/2}/(1-a_{1/2})]$ (Fig. 5.3d). The latter can be considered a free-energy difference $(-\Delta G) = G_{\mathrm{down}} - G_{\mathrm{up}}$ between the inactive and active states of an equilibrium two-state switching process in which the time-averaged activity $a_{1/2}$ is given by the probability of being in the active state, $a_{1/2} = p(\mathrm{active}) = (1 + e^{\Delta G/k_B T})^{-1}$. The residence time in each state can then be described by an Arrhenius-type relation with characteristic time for barrier crossing τ_r and the height of the energy barrier dependent on ΔG,

$$\begin{aligned} \tau_{\mathrm{down}} &= \tau_r \exp\left[-\gamma_{\mathrm{down}} \Delta G / k_B T\right] \\ \tau_{\mathrm{up}} &= \tau_r \exp\left[-\gamma_{\mathrm{up}} \Delta G / k_B T\right] \end{aligned} \tag{5.1}$$

where the (dimensionless) constants γ_{down} and γ_{up} describe how the barrier heights of the down and up states, respectively, depend on the free-energy difference $\Delta G = k_B T \ln[(1 - a_{1/2})/a_{1/2}]$. We find $\gamma_{\text{down}} = -0.4 \pm 0.1$, $\gamma_{\text{up}} = 0.6 \pm 0.1$, and the characteristic timescale τ_r, defined here as equivalent to $\tau_{\text{up}} = \tau_{\text{down}}$ when $\Delta G = 0$ (and hence $a_{1/2} = 0.5$), was found to be 110 ± 10 s. The fact that the mean residence times $(\tau_{\text{up}}, \tau_{\text{down}})$ scale exponentially with the apparent free energy difference (ΔG) indicates that receptor-kinase switching can, to a first approximation, be treated as a barrier-crossing process.

In summary, these data demonstrate the existence of a signaling noise source that is independent of the adaptation enzymes CheR/CheB. The fluctuations they generate can be very strong in cells expressing Tsr as the sole chemoreceptor, leading to two-level switching in a subset of cells. The latter observation suggests that cooperativity among signaling units in homogeneous chemoreceptor arrays can reach extremely high values, with up to $\sim 10^3$ units switching in a cooperative fashion. The temporal statistics of these two-level switches are consistent with a barrier-crossing model in which the residence time of both states depend on the activity bias $\ln[a_{1/2}/(1 - a_{1/2})]$ in a nearly symmetric manner with opposing signs.

5.2.4 Giant fluctuations are absent in cells defective in cooperativity

To further investigate the underlying mechanism of these fluctuations, we performed a similar experiment with a Tsr mutant (Tsr-F396Y) which is defective in receptor cooperativity (Fig. 5.4a, see Chapter 6, in which we show that the ligand-response Hill coefficient of single cells is reduced from ~ 20 in wildtype to 1.6). When stimulated with a sub-saturating stimulus that inhibits approximately one half of the population-averaged activity level, the fluctuation amplitude, as judged from the average single-cell power spectra (Fig. 5.4b), decreased drastically. The single cell time series did not show any stochastic discrete transitions (Fig. 5.4c) or large fluctuations. The slight elevation of the spectrum of Tsr-F396Y at low frequencies might be due to the residual cooperativity of this mutant (1.65, instead of 1). Imaging the chemoreceptors revealed that Tsr-F396Y has impaired clustering compared to Tsr-WT (K. Scherer, personal communication), suggesting that the chemoreceptors might be able to form small arrays, but not large ones. The absence of fluctuations and switching in Tsr-F396Y strongly suggests that the fluctuations we have observed in the absence of the adaptation enzymes CheR and CheB either originate in the cooperative interactions within the chemoreceptor array, or that a noise source external to the chemoreceptor array is amplified by the cooperativity of array components.

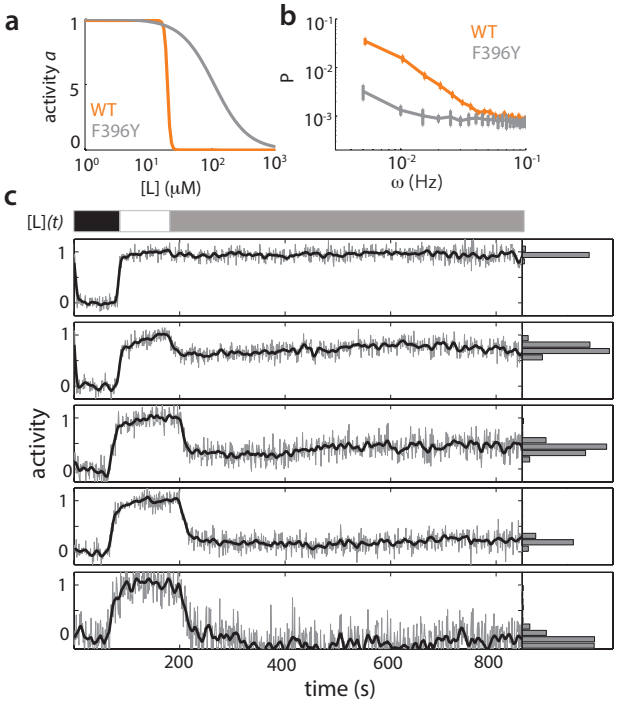

Figure 5.4: Experiments with mutant defective in cooperativity show no stochastic switching behaviour. **(a)** Hill curves illustrating the difference in cooperativity of the dose-response curves between wildtype Tsr and Tsr-F396Y. The dose response parameters are the average single-cell fit values obtained from single-cell FRET experiments on both genotypes in *cheRB* background (See Chapter 6). **(b)** PSD estimates for temporal signal fluctuations from cells expressing wildtype Tsr and Tsr-F396Y in cells without chemoreceptors and adaptation enzymes (TSS1964/pPA114). Shown are the average of the single cell PSD estimates from a single experiment, error bars represent s.e.m. **(c)** (Top) Stimulus protocol for L-serine concentration ($[L](t)$). At the start of the experiment, a saturating concentration ($[L]$ = 1mM, black) is applied for a short time. After flushing buffer ($[L] = 0$, white), an intermediate concentration ($[L] = 150 - 175\mu$M, gray) is sustained for ~10 minutes. (Bottom) Representative single-cell time series, each normalized to its activity level before adding the first stimulus. The top two curves are taken from an experiment (34 cells) responding to 150μM, bottom three curves from a second experiment (49 cells) responding to 175μM. To the unfiltered data (gray) a 10s moving average filter is applied and superimposed.

5.2.5 Adaptation-independent fluctuations in the absence of ligand stimulation

The experiments on Tsr-WT, Tsr-F396Y have in common that fluctuations are studied in the presence of chemoattractant, while the fluctuations due to methylation we have observed (Chapter 4) take place in the absence any applied ligand. Could the observed unsteadiness of signaling in adaptation deficient cells arise from fluctuations in ligand uptake or binding? Wildtype cells (CheRB+) show sponteneous fluctuations because the bias of the chemoreceptor arrays in wildtype cells is reduced from $a_0 \approx 1$ to $a_0 \approx 1/3$ by post-translational modifications of the chemoreceptors due to CheR and CheB. It is possible to change the bias of the chemoreceptor using genetic modifications that mimic the post-translational modifications catalyzed by the adaptation enzymes CheR and CheB [183]. Cells expressing Tar in the QEEE modification state have an intermediate activity bias in the absence of ligand. We measured fluctuations in cells expressing Tar-QEEE (TSS1964/pVS120) in the absence of any stimulus, and then added a saturating amount of chemoattractant and chemorepellent to determine the extremes of each single-cell FRET response. Whereas the population-averaged FRET signal did not show large fluctuations (Fig. 5.5a), we found that individual cells exhibit very large fluctuations (Fig. 5.5b) similar to the fluctuations observed in cells expressing chemoreceptor Tsr, but with the difference that in the case of Tar-QEEE, the fluctuations could be observed in the absence of ligand. Of all the 194 tested single cells of this strain, 33 cells demonstrated two-state switching (Fig. 5.6a). We calculated the residence times $\Delta t_{\mathrm{up,k}}$ of the two-state switching cells and found that the interval times $\tau_{\mathrm{up/down}}$ obtained from the fluctuations in Tar-QEEE cells in the absence of ligand scaled with the free energy from the activity bias (Fig. 5.6b). The slopes of $\log \tau_{\mathrm{up/down}}$ versus $\log[a_{1/2}/(1-a_{1/2})]$ were $\gamma_{\mathrm{up}} = 0.48 \pm 0.06$ and $\gamma_{\mathrm{down}} = -0.40 \pm 0.05$. The characteristic timescale $\tau_r = 75 \pm 6$ s is of the same order, but somewhat shorter, compared to fluctuations observed with Tsr. These similarities between the fluctuations in Tar-QEEE in the absence of stimulation and those from cells expressing Tsr during ligand stimulation (Fig. 5.3b) suggest they have similar mechanistic origins and are a property of the chemoreceptor arrays, not specific to a particular chemoreceptor species.

We investigated the transition time of each switching event in cells with Tar-QEEE arrays. By fitting the decay or increase with the same symmetric exponential function as was used for fluctuations in Tsr arrays we found for the average transition time over all events in all cells $\langle \tau_+ \rangle \pm \sigma_{\tau_+} = 5.4 \pm 4.5$ s and $\langle \tau_- \rangle \pm \sigma_{\tau_-} = 6.0 \pm 4.6$ s (Fig. 5.7a). The variability in these timescales was quite large among al events, raising the question what could be the main variable determining this variability. Although the complete answer is beyond the scope of this present study, we noted a positive and significant correlation ($\rho = 0.49 \pm 0.42$) between the average transition times per cell $\langle \tau_\pm \rangle_i$ for decay and rise events

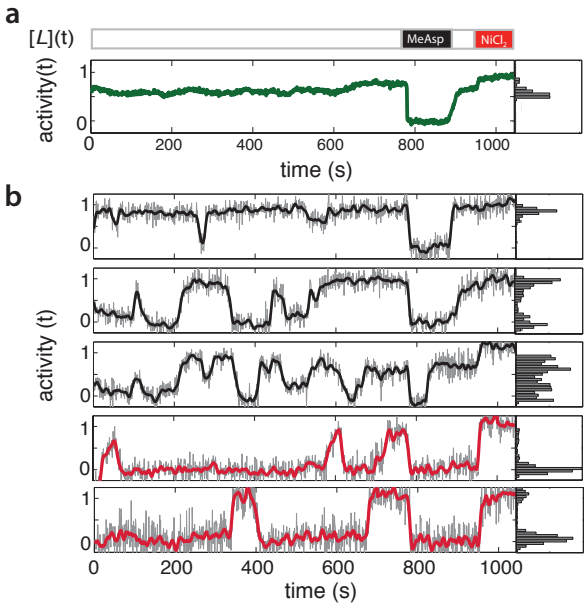

Figure 5.5: Adaptation-deficient cells with intermediate activity bias exhibit fluctuations in the absence of ligand stimulation. **(a)** (Top) Stimulus protocol for L-serine concentration ($[L](t)$). After flushing buffer ($[L] = 0$, white) is sustained for ~10 minutes, after which a saturating attractant concentration ($[L]$ = 1mM MeAsp, black) is applied for a short time, finalized with a saturating repellent stimulation (300μM $NiCl_2$, red). (Bottom) FRET timeseries of a population of 75 cells (RB- Tsr-QEEE; TSS1964/pVS120) responding to the applied stimulus protocol. The time series has been normalized to the response to the repellent stimulus. **(b)** Selected single-cell time series of the population shown in panel each normalized to its activity level to the repellent stimulus. To the unfiltered data (gray) a 10s moving average filter is applied and superimposed (Red colored time series indicate two-state switching, Fig. 5.5a).

(Fig. 5.7), implying there is a cell-specific parameter that affects the transition times of both up and down transitions in a rather symmetric way.

In summary, these experiments on cells expressing Tar-QEEE as the sole chemoreceptor revealed that ligand stimulation is not required for giant fluctuations in signaling activity. including stochastic two-state switching behavior. The two-state switching behavior of these cells expressing Tar-QEEE in the absence of ligand closely resembled that of cells expressing Tsr exposed to subsaturating ligand doses, both in the fraction of cells that exhibited two-state switching (12 % and 17 %, respectively) and the characteristic timescale of the residence times (110 vs 75 seconds). The duration of transition events (3-6 s) were also similar,

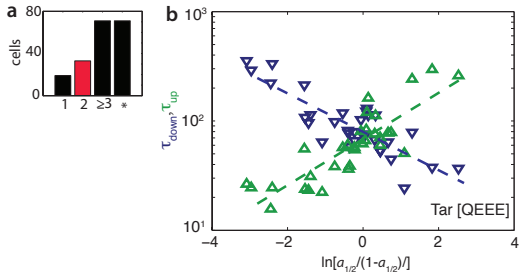

Figure 5.6: Fluctuations in cells with intermediate activity bias in the absence of ligand are consistent with barrier crossing process. **(a)** Inset: classification of RB-Tar-QEEE single-cell fluctuation phenotypes by the number of stable activity levels observed during the sustained subsaturating stimulus, as in Fig. 5.3, with cells showing apparently two stable states indicated in red. Total 194 cells. **(b)** Mean residence times τ_{up} and τ_{down} for two-state switching cells (Tar-QEEE) as a function of the average activity bias $\ln[a_{1/2}/(1-a_{1/2})]$. The slopes are $\gamma_{\mathrm{up}} = 0.48 \pm 0.06$ and $\gamma_{\mathrm{down}} = -0.40 \pm 0.05$, and the crossover point at $\tau_{\mathrm{up}} = \tau_{\mathrm{down}} = 75 \pm 6$ s defines a characteristic switching timescale. Data of 33 cells from 4 independent experiments (three at 1 Hz acqusition, one at 0.2 Hz acquisition). Definitions of residence times as in Fig. 5.3b.

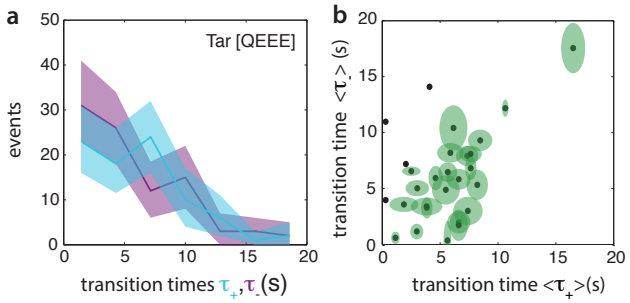

Figure 5.7: Transition times of fluctuations show cell-to-cell variability. **(a)** Distributions of transition time up τ_+ (93 events, purple) and down τ_- (84 events, cyan) from 29 cells showing stochastic two state switching in the absence of ligand (Tar-QEEE). Transition times are defined in Fig. 5.3b. **(b)** Correlation between average transition time up $\langle\tau_+\rangle$ and down $\langle\tau_-\rangle$ for 29 cells showing spontaneous two-state switching (Tar-QEEE) with shaded ellipsoids representing the error basins, with the s.e.m of $\langle\tau_+\rangle$ and $\langle\tau_-\rangle$ for long and short axis. Cells with less than three events up and down do not have an error basin. Pearson-correlation coefficient is $\rho = 0.49 \pm 0.42$. The bias of the distribution is $\langle\tau_+\rangle - \langle\tau_-\rangle = -0.8$

but seem to be somewhat slower for Tar-QEEE compared to Tsr cells. We note that because in our analysis these timescales are constrained to be positive, the difference in sample size may contribute to this disparity.

5.2.6 Is chemoreceptor switching a non-equilibrium process?

Most quantitative models of chemoreceptor array activity have assumed that receptor-kinase activity modulation is an equilibrium process, in which no energy is dissipated and all microscopic transitions obey detailed balance. While these models are usually simpler than non-equilibirum descriptions, and hitherto obtained (population-averaged) experimental data can be explained by equilibrium models, there has been no direct evidence in support of either of these two classes of models. However, a number of key processes within the chemosensory array are in fact dissipative, such as receptor methylation/demethylation, and also CheA kinase autophosphorylation. If the latter would influence the kinetics of receptor-kinase switching, one would expect an asymmetry between switching at high and low activity bias since the kinase dissipates (chemical) energy only when active. While our results show that the mean residence times of cells $\tau_{\mathrm{up/down}}$ scale exponentially with the activity bias, that observation does not rule out the possibility that non-equilibrium processes play a role in switching. Seeking further insight regarding this issue, we asked how the intervals $\Delta t_{\mathrm{up/down},k}$ within each cell are distributed. Since the number of events per cell is small, we sorted the events by activity bias and made histograms of all intervals of cells with Tar-QEEE. As expected, we see that the distributions $\Delta t_{\mathrm{up},k}$ and $\Delta t_{\mathrm{down},k}$ vary systematically with activity bias (Fig. 5.8), with the two distributions appearing similar in cells with an activity bias of $0.45 < a \leq 0.55$ (close to ΔG=0) look similar.

If the interval timescale is a simple memoryless process, the distribution for interval times is expected to be exponential. It has been shown that this property is shared between all equilibrium allosteric models that obey detailed balance [212]. We notice that the distribution of interval times around $a = 0.5$ deviates from an exponential distribution (Fig. 5.6c), indicating the possibility that receptor-kinase is a non-equilibrium process. While drawing events from several cells (each with an exponential distribution defined by a different timescale) could lead to a non-exponential ensemble distribution, this cannot explain why the distribution appears to be peaked. This can be seen simply from considering the derivative of a sum of exponential functions $c_i e^{-t/\tau_i}$ with positive definite prefactors c_i and (potentially) different timescales:

$$\frac{d}{dt}\sum_i c_i e^{-t/\tau_i} = \sum_i \frac{d}{dt} c_i e^{-t/\tau_i} = \sum_i -\overbrace{\frac{c_i}{\tau_i}}^{>0} \underbrace{e^{-t_i/\tau_i}}_{>0} < 0$$

in which the negative derivative shows that the resulting sum of exponentials is a monotonically decaying function. Taken together, while the scaling of mean residence times with the activity is consistent with a simple barrier-crossing (equilibrium) process, the peaked distribution of interval times raises the intriguing possibility that chemoreceptor switching is a dissipative process.

5.3 Discussion

We found temporal fluctuations in adaptation-deficient (CheRB-) cells expressing wildtype chemoreceptor complement (Figs. 5.2), but these fluctuations were most dramatic in cells with only one chemoreceptor species (Figs. 5.2 and 5.5). When brought close to their dose-response transition point (K) by attractant stimulation or by changing the activity bias via genetic modifciation, these cells demonstrated strong temporal fluctuations, revealing that there exist sources of signal fluctuations that are independent of CheR and CheB activity. The origin of these adaptation-independent fluctuations remain unknown, but in broad terms, one can envisage that they are due to either intrinsic sources (i.e. fluctuations arising within the components of the receptor-kinase complex), extrinsic sources (i.e. fluctuations in other cellular processes / environmental variables), or both. Possible intrinsic sources include coupled fluctuations in protein conformations [51, 121, 180, 187], the slow-timescale changes in receptor “packing" that have been observed by fluorescence anisotropy measurements [64, 218], and the stochastic assembly dynamics of receptor clusters [71]. Possible extrinsic sources include fluctuations in the cell’s metabolism, or membrane physiology. Fluctuations of one potential extrinsic noise source, namely active transport/consumption of ligand, is excluded by our observation that the fluctuations can take place in the absence of applied ligand.

The adaptation-independent fluctuations we observed were not only large in amplitude but often (though not always) took the form of discrete steps in activity, in some cases between only two levels. Two-state descriptions of receptor signaling are a common feature of nearly all mechanistic models of bacterial chemotaxis signaling addressing both cooperativity [51, 85, 121, 123, 180] and adaptation [7, 10, 57, 59, 130, 215], yet direct evidence for two-state switching by receptor-kinase complexes has been lacking. Regarding cells that exhibited step-like transitions among more than two stable states, a plausible interpretation is that the underlying transitions are actually two-level, but the majority of the receptor-kinase population is partitioned into two or more disjoint signaling arrays which fluctuate independently. Experiments which visualise the cluster organisation and measure the FRET response on the same cells would provide an interesting direction for future FRET studies.

Although as noted above, it is yet possible that the two-level switching we

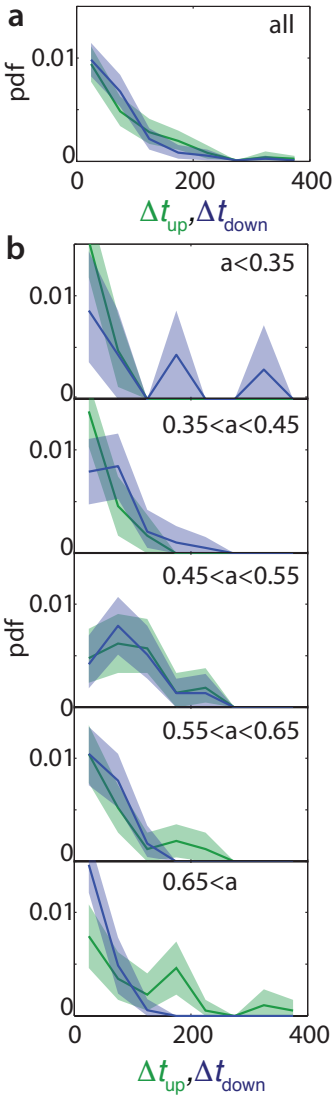

Figure 5.8: Switching residence time distributions. **(a)** Distribution of residence times Δt_{up} (green, 140 events) and Δt_{down} (blue, 136 events) of all events obtained from TarQEEE cells. **(b)** Distribution of residence times Δt_{up} (green) and Δt_{down} (blue) sorted by steady-state activity as indicated in each panel. Number of events $\{\Delta t_{\text{down}}, \Delta t_{\text{up}}\}$ per histogram, from top to bottom: $\{13,12\}$, $\{21,19\}$, $\{34,33\}$, $\{35,38\}$ and $\{33,38\}$. Shaded areas represent 95 % confidence interval obtained through bootstrapping.

observed (Fig. 5.2b) is due to extrinsic noise sources (e.g. metabolism or transport), the temporal statistics (Fig. 5.3 and 5.6) are compatible with a simple model in which two stable signaling states are separated by an energy barrier sensitive to both environmental stimuli and internal cell variables. Our observation of fluctuations in the absence of ligand stimulation exclude one potential external noise source, namely fluctuations in transport or metabolism of chemoeffector ligands. If the stochastic two-level switching we observed is indeed due to intrinsic sources of noise, it would strongly suggest (as discussed in above) that at least many hundreds, if not thousands of receptor-kinase units are switching in a cooperative fashion. The rather long timescale associated with intervals between switches ($\approx 10^2$ s) is indicative of their large size, and is also clearly distinct from the methylation-dependent fluctuation timescale (≈ 10 s) observed in CheRB+ cells. The switching duration (≈ 5 s) , is also much slower than the sub-second response to attractant stimuli [173, 191]. Interestingly, these timescales ($\sim 10^2$ s and $\sim 10^0$ s for inter-switch intervals and switch durations, respectively) are approximately 10^2-fold longer than those measured by [8] for the two-state switching of the flagellar motor ($\sim 10^0$ s and $\sim 10^{-2}$ s for inter-switch intervals and switch durations, respectively), whose C-ring is composed of $\sim 10^1$ allosteric units, approximately 10^2-fold less than the $\sim 10^3$ units we estimate for the number of receptor-kinase units per cell in our experiments. The study of [8] demonstrated impressive agreement between those temporal statistics and predictions of a "conformational spread" model [21, 50], an adaptation of the equilibrium Ising model for ferromagnetism [77]. It would be interesting to investigate whether similar Ising-type models for the receptor lattice [51, 121, 180, 188] can explain the timescales observed in our receptor-kinase switching data.

Although our results indicate that, at least to a first approximation, receptor-kinase switching can be treated as a thermally driven barrier-crossing process, we note that our data do not rule out the possibility of non-equilibrium switching mechanisms [212]. In fact, the deviation from an exponential distribution distribution of the residence times for cells with an activity bias around 1/2 (Fig. 5.8) could indicate a dissipative process [212]. In such a situation, the differences in average transition times per cell could indicate cell-to-cell variability in energy dissipation, possibly in combination with variability in chemoreceptor cluster size, of which the latter could also explain the variability in case the switching process is passive. While equilibrium models have been highly successful in explaining chemoreceptor array behavior, this does not exclude the possibility of non-equilibrium processes. Indeed, despite the success of equilibrium models in closely matching a wealth of data on the flagellar motor switch [8], recent experiments have revealed new evidence that switching of the motor C-ring likely includes also an active component, effectively utilizing part of the energy dissipated in motor torque generation to enhance sensitivity [226]. Like the motor C-ring switch, whose state is only observable when coupled to rotation driven by

dissipative proton conduction, essentially all experimental methods available to study receptor-kinase signaling involve coupling to a dissipative process (ATP hydrolysis by CheA) for readout. The experimental access to receptor-kinase temporal statistics afforded by single-cell FRET holds promise to further help discriminate possible equilibrium and non-equilibrium mechanisms for signal processing within this remarkable protein circuit.

5.4 Materials and Methods

5.4.1 FRET experiments

FRET experiments were performed as described in Chapter 2, which includes a list of the strains and plasmids used in this study (§2.4). The expression of Tsr and Tar-QEEE from a plasmid was set with respectively 0.6 and 2.0 μM sodium salicylate [NaSal].

We thank Fotis Avgidis, Francesca van Tartwijk and Iwan Vaandrager for help with FRET experiments and Simone Boskamp for cloning and cell culture.

5.4.2 Two-state switching analysis

Since the amplitude of two-state switches is much greater than the noise, switching events times t_0 could be easily read off by eye. We obtained switching durations by fitting the function

$$a(t) = \frac{1}{2} \pm \frac{1}{2} \frac{t - t_0}{|t - t_0|} (1 - e^{-2|t-t_0|/\tau_\pm}) \tag{5.2}$$

to the normalized FRET time series in a 30-second time window, approximately ±15 s from t_0. The residence times $\Delta t_{\mathrm{up},i,k}$ and $\Delta t_{\mathrm{down},i,k}$ of event k in cell i were defined by the time between transitions or the beginning/end of the 20 μM stimulus time window. The steady-state activity during activity was then calculated as

$$a_{1/2,i} = \frac{\sum_k \Delta t_{\mathrm{up},i,k}}{\sum_k \Delta t_{\mathrm{up},i,k} + \sum_k \Delta t_{\mathrm{down},i,k}} \tag{5.3}$$

and for the residence times we take the mean of $\Delta t_{\mathrm{up/down},k}$ over k to obtain τ_{down} and τ_{up}. If we treat the system as an equilibrium process we can use the Arrhenius equations that describe the residence times as a function of the distance to the energy barrier

$$\begin{aligned} \tau_{\mathrm{down}} &= \tau_r \exp\left[\gamma_{\mathrm{down}} \ln\left[a_{1/2}/(1 - a_{1/2})\right]/k_B T\right] \\ \tau_{\mathrm{up}} &= \tau_r \exp\left[\gamma_{\mathrm{up}} \ln\left[a_{1/2}/(1 - a_{1/2})\right]/k_B T\right] \end{aligned} \tag{5.4}$$

in which γ_{down} and γ_{up} are constants corresponding to the slopes of $\ln \tau_{\mathrm{down}}$ and $\ln \tau_{\mathrm{up}}$ against $\ln [a_{1/2}/(1-a_{1/2})]$, respectively. The fit parameters and standard error are obtained with the robustfit function in Matlab (statistics toolbox).

6

The Molecular Origins of Signal Amplification

In this chapter, we use single-cell FRET to investigate the relation between single-cell and population-averaged responses of the chemotaxis pathway activity. We consider two types of responses: the time course of kinase activity upon rapid changes in input ligand concentration (step-response time series) and the amplitude of kinase activity change as a function of stimulus sizes (dose response curves). We show that for these nonlinear functions (of time or ligand concentration, respectively), very similar population-averaged behaviour can result from very different underlying single-cell responses. When changes in activity appear gradual (either versus time or ligand concentration) in population averaged experiments, they may correspond either to truly gradual single-cell responses or to steep single-cell responses in combination with high variability in the value of the independent variable (time or ligand concentration) that yields a half-maximum response. Recently reported population-averaged experiments have identified genetic mutations that reduce the steepness of population dose response curves. We confirm that these mutations demonstrate genuine cooperativity defects at the single-cell level. These data provide new insights for understanding the molecular mechanisms that underlie signal amplification, a fundamental and widely observed property of signalling networks. We also describe single-cell experiments with a chemoreceptor point mutation that results in a dramatically (~1000 fold) slowed decay in activity upon stimulation with sub-saturating concentrations of attractant. The experiments presented in this chapter highlight the potential pitfalls of ensemble-averaging in measuring intracellular signalling dynamics, and the power of single-cell FRET in overcoming them.

6.1 Introduction

Bacteria such as *E. coli* navigate spatial chemical gradients by means of a chemotaxis signal transduction network. This signaling pathway has been widely studied, and exhibits many interesting network phenomena [216] such as signal amplification [2], sensory adaptation by integral feedback [3, 233], and fold-change detection [98]. Because of strong functional similarities between the behavior of electrical and biological circuits, the study of biological circuits has greatly benefitted from the analogies of biochemical signalling networks and electronic circuits, the latter being studied extensively control theory [43, 215, 233]. However, the physical implementation of biochemical networks is very different from electrical networks. First, electrical circuits are generally designed to have low variability from device to device, whereas variability in biological systems can be considerable. Second, because the spatial organisation of biological systems originates entirely from molecular interactions, cells are able to dynamically rewire signaling circuits by spatially reorganising these components. Therefore, understanding signal processing in biological circuits is challanged by both variability across cells in a population, and within an individual across time.

An example of biological signal processing is the chemoreceptor arrays of the bacterial chemotaxis pathway, a protein complex consisting of transmembrane chemoreceptors, kinases and scaffolding molecules [144]. Unlike other well known large protein complexes, such as the bacterial flagellar motor, the eukaryotic nuclear pore complex and the mitochondrial complex I (NADH dehydrogenase in human mitochondria), the number of protein species is limited, but the recurring hexagonal pattern formed by these components may contain up to thousands of protein molecules. Despite years of research on chemoreceptor arrays, especially in model organism *E. coli*, the molecular mechanisms by which signals are transmitted throughout the array to achieve the observed signal amplification remain poorly understood. Signal amplification is an important functional feature of the pathway that enables bacteria to detect very small changes in chemoeffector concentrations

Soon after the discovery that chemoreceptors are clustered in the cell membrane [113], it was hypothesised that this spatial arrangement has a functional role in signal amplification [22]. Since then, many quantitative models of receptor activity have included receptor-receptor interactions without specifying the molecular details [85, 123, 215]. Despite the success of these models in reproducing a wealth of experimental data, until recently there has been no direct evidence for the role of clustering in signal amplification. Early attempts to identify genetic mutations that break cooperativity, yielded genotypes defective in array formation, but all such mutants were also completely defective in signaling [4], thus precluding tests of cooperativity.

Recent advances in resolving the molecular structure of the chemoreceptor

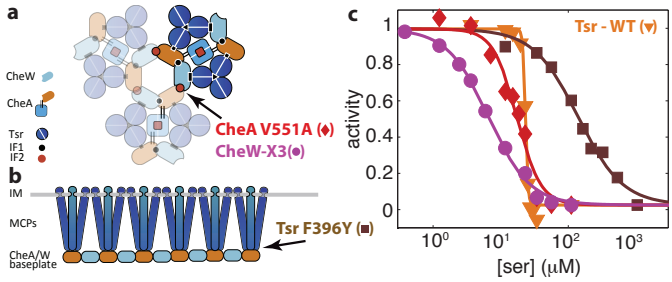

Figure 6.1: Genetic mutations in chemosensory array components can reduce response cooperativity in population-averaged experiments. **a)** Schematic top view of chemoreceptor arrays. A single core unit consists of six chemoreceptor dimers (blue half circles) with one CheA dimer and one CheW scaffolding molecule, through a connection between CheW and the P5 domain of CheA (interface 1, black circles). The core unit is shown in connected to other core units (shaded) by another CheW-CheA-P5 interaction (interface 2, red circles). Mutations CheW-X3 and CheA-V551A are found to reduce the interface 2 binding, which allows for formation of core units but prevents formation of larger arrays. Image adapted from [149]. **b** Schematic side view of chemoreceptor arrays with transmembrane chemoreceptors and a CheA-CheW baseplate. The mutant Tsr-F396L carries a point mutation at the receptor tip, close to the CheA-CheW baseplate. Image adapted from [78]. **c** Mutants of Tsr and CheA-CheW interface 2 (colors and symbols as in panel a-b) show lower cooperativity of the cellular response to serine, compared to Tsr-WT (orange triangles). Measurements are population averaged results from FRET experiments shown in Figs. 6.4 and 6.5.

array dramatically narrowed the search space for the critical residues responsible for signal amplification. These studies have revealed that chemoreceptor clusters are organized as large arrays with a recurring hexagonal geometry ([25, 26, 144], see Fig. 6.1a). The basic functional unit of such an array —the core complex— consists of six chemoreceptor dimers, one CheA dimer with two CheW molecules. Core units are formed though an interaction between the P5 domain of CheA (see Fig. 1.5c for a the domain structure of CheA) and CheW, and the adjoining segments of these proteins have been named interface 1. A second interaction, at segments named interface 2, between CheA-P5 and CheW allows links core units into larger arrays. By targeting residues in CheW or CheA-P5 that are located in or close to this interface, it was possible to identify mutations that reduce interface 2 interactions and thus preventing formation of large chemoreceptor arrays [149]. Unlinked core units in interface 2 mutants maintain there ability to respond to attractant stimuli, but with very low cooperativity (Fig. 6.1c).

Amino acid replacements at a highly conserved phenylalanine residue in the receptor tip (F396 in Tsr, Fig. 6.1b) impair chemotaxis performance on soft agar plates [141] and some replacements at this site also reduce response cooperativity

in FRET kinase assays (J.S. Parkinson, personal communication, and see Fig. 6.1c) while retaining approximately equivalent steady-state activity level to wild-type chemoreceptors.

Structural studies of this large protein complex tend to focus on the static molecular configurations, because the highest resolution techniques to study chemoreceptor arrays, most notably X-ray crystallography and electron microscopy, only provide snapshots in time of the chemoreceptor array structure. However, because function follows structure, the dynamic properties of signalling complexes are important for signalling dynamics within array complexes. This idea has led to suggestions that the stability of the chemoreceptor cluster might change upon ligand stimulation, a controversial issue in the field with conflicting evidence. Biochemical *in vitro* data indicated that receptor clusters are "ultrastable" over time [60], and diffraction-limited fluorescence microscopy indicated there is no large-scale reorganisation of clusters upon ligand stimulation [23, 106]. The vast majority of *in vivo* (population) FRET data [123, 183] are satisfactorily described by models that assume a fixed receptor array size and configuration. However, studies using immunostaining indicated that large clusters decrease in size upon stimulation [232]. Also recent population FRET data indicated a slow-timescale reorganisation of chemoreceptor arrays upon ligand stimulation [64]. Hence further measurements that specifically include information on the dynamics of signal processing might tell us how signals progress through the chemoreceptor arrays and how ligand stimulation influences array output and structure. While FRET microscopy does not have a very high spatial resolution compared to many other imaging techniques, but unlike these techniques with high spatial resolution it's temporal resolution is high.

6.2 The necessity of single-cell measurement techniques

Population-averaged FRET has been highly successful in facilitating high-throughput measurements of the activity of both wild-type chemoreceptor arrays as well as mutants with altered arrays [64, 149, 193], but the problem with population averaged measurements such as shown in Fig. 6.1b is that these measurements average the signal over hundreds of cells. Generally, when measuring non-linear functions such as the sigmodal shaped dose response curve of chemoreceptor activity versus ligand concentration, the average of the responses can be different from the response average. Mathematically, this is a consequence of Jensen's inequality. In the context of stochastic variables, this can be formulated as

$$f(\mathbb{E}(X)) \neq \mathbb{E}[f(X)] \tag{6.1}$$

in which X is a random variable, $\mathbb{E}$ the expectancy value and f is a function. If f is convex, the inequality sign can be replaced with $\leq$ and if f is concave, it becomes $\geq$. For our purposes, the main point illustrated by Jensen's inequality is that single-cell measurements are not only relevant for providing error bars. If one considers a biological network as a set of transfer functions (f, g, and so on) that map the molecular input to the phenotypic output, signal propagation through such a network can then potentially be described as a series of nested transfer functions ($f[g[h[X]]]$). If X is a deterministic variable calculating the output is relatively straightforward. However, in case X is stochastic, calculating the expectancy value is more complicated. It may seem tempting to ignore variability, perform the calculation as if X is deterministic and finally just acknowledge that there probably is some variability in calculation result because of error propagation. If all functions are linear, or deviations of linearity are small, this works well. However, when one starts averaging nonlinear functions this becomes a sin which cannot be simply patched by adding error bars, since the expected value depends on the entire distribution. It is in these circumstances that single-cell experiments are most important. This effect is nicely illustrated by a recent study of bacteria swimming up a chemical gradient using run-and-tumble motion [225], a performance measure which depends (non-linearly) on the phenotypical trait of the fraction of time spent tumbling. Consequently, the performance of the average phenotype is lower than the average performance, because there were some individuals that were able to climb the gradient much faster than the rest of the population.

In the case of dose response curves, the difference between population-averaged and single-cell responses is illustrated in Fig. 6.2, in which three examples single-cell dose response ensembles that give rise to indistinguishable population dose response curves are shown. Dose response curves can often be described well by a hill curve, $[1 + ([L]/K)^H]^{-1}$, where the parameters $(1/K)$ and H are defined as the sensitivity and steepness. A high cell-to-cell variability in the sensitivity (or half-maximum value) K can manifest itself as being low-cooperative despite a large fraction of the population having steep responses. Hence genotypes that appear to have a cooperativity defect, such as the interface 2 mutants, might or might not show a cooperativity defect on the single cell level. The only way to discriminate between these two possibilities to measure dose response curves on the single cell level.

6.3 Cooperativity defects in single-cell ligand sensing

FRET between of fluorescent fusions to CheZ and CheY is proportional to the dephosphorylation rate of CheY-P by CheZ. On timescales longer than the CheY-P

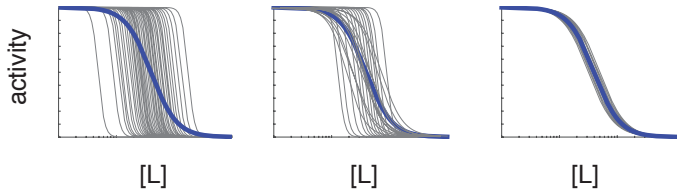

Figure 6.2: Schematic illustration of three contrasting distributions of single-cell dose-responses (gray) that lead to identical population-averaged dose response curves (red). In cases where both the sensitivity (K) and steepness (H) of single-cell dose response curves are nearly uniform across the populatoin (right), the ensemble averaged reflects well the single-cell phenotype. But if either K (left) or both K and H vary strongly across the population, the steepness of ensemble-averaged Hill curves will underestimate the true steepness of the underlying single-cell responses (Jensen's inequality).

lifetime (~ 100 ms), this rate is equal to the production rate of CheY-P by the kinase CheA in the chemosensory arrays, which is in turn controlled by ligand-receptor binding. In many cases, a convenient measure of kinase activity a, is to normalize the FRET level by the maximum FRET level. This activity can be interpreted as the fraction of active kinases or the fraction of time the kinases are active during a time interval. By monitoring the activity at different ligand concentrations, a dose-response curve can be constructed which describes how the activity depends on extracellular ligand concentration. Previous dose response curves were obtained by integrating the fluorescence signal from a dense layer containing hundreds of cells, but by using image segmentation on sparse samples the FRET level can be obtained for single bacteria. All measurements described in this chapter were performed in a background where the genes responsible for adaptation, *cheR* and *cheB*, are deleted. This fixes the modification level of the chemoreceptors and hence should reduce the cell-to-cell variability. Also, the steady-state activity level of Tsr in its native methylation state (QEQEE) is close to 1, which greatly benefits signal-to-noise in these experiments. We measured single-cell dose response curves on one of the population-average cooperativity defect strains, CheW-X3, expressing only the chemoreceptor Tsr, by exposing them to a series of stimuli of serine (Fig 6.3b). From the single-cell FRET time series, a dose response curve is calculated and fitted with a Hill function (Fig 6.3b). The vast majority of cells could be properly fit with a Hill function and look qualitatively similar to the population-averaged time series, although the parameters required for a good fit vary from cell to cell. We find values of $H = 1.5 \pm 0.5$ (mean and standard deviation) and K =5.7 $\pm$ 1.8 (geometric mean and standard deviation). When comparing the Hill curves for the CheW-X3 mutant with wild-type cells (Tsr in UU2567, $H = 24 \pm 13$, $K = 20 \pm 2$), there is a

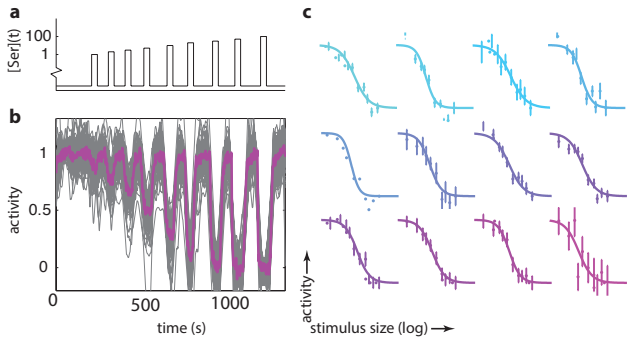

Figure 6.3: Single-cell FRET can be used to measure dose response curves of single cells. **(a)** ligand stimulation protocol for typical dose response experiment. **(b)** Activity time series of 86 of 93 single cells (grey), expressing CheW-X3 in CheRB- background with Tsr as the only chemoreceptor and measured by single-cell FRET. The population-averaged signal is superimposed (purple). Each single-cell time series is normalized by its maximum FRET level before the first stimulus. **(c)** Representative fits of Hill curves to activity data measured by FRET. Error bars are standard error of the mean obtained from the fluctuation of the FRET ratio over a time window, in which each of the ≈ 20 measurement points per stimulus is an independent measurement.

dramatic decrease in the single-cell steepnesses (Fig. 6.4). Also experiments and fits to cells expressing CheA-V551A ($H = 2.6 \pm 1.4$, $K = 15 \pm 6$), another interface 2 mutant, and Tsr-F396Y ($H = 1.65 \pm 0.4$, $K = 109 \pm 33$), another cooperativity defect suspect, showed a decrease in cooperativity at the single-cell level. Hence in all these mutants, the Hill curve parameters from the population averaged time series fit agree well with the average single-cell parameters.

A low Hill coefficient measured with FRET at the population level does not necessarily imply a low Hill coefficient at the single-cell level. As a proof of principle, we engineered an ensemble of cells with large spread in ligand sensitivities. It has been shown that the sensitivity of the receptors can be tuned artificially by exploiting the fact that replacing one of four specific glutamic acid (E) modification residues with glutamate (Q) reduces the sensitivity to ligand, mimicking the CheR-mediated methylation (Em) of the residue [72, 183]. We used this to generate cells with modification states {QEQE,QQQQ,QEmQEm}, in which the extremes of the sensitivity are three orders of magnitude apart. We measured this mixture (Fig. 6.5a) and found that the response of the population seemed very shallow ($H_{pop} = 0.8$) but the single cells show a highly cooperative response ($H = 9.8 \pm 9.9$, $K = 99 \pm 225$). In this case, inferring single-cell responses from an ensemble average without prior knowledge of the ensemble is impossible. This problem is not limited to mixed batches but can also occur in isogenic popu-

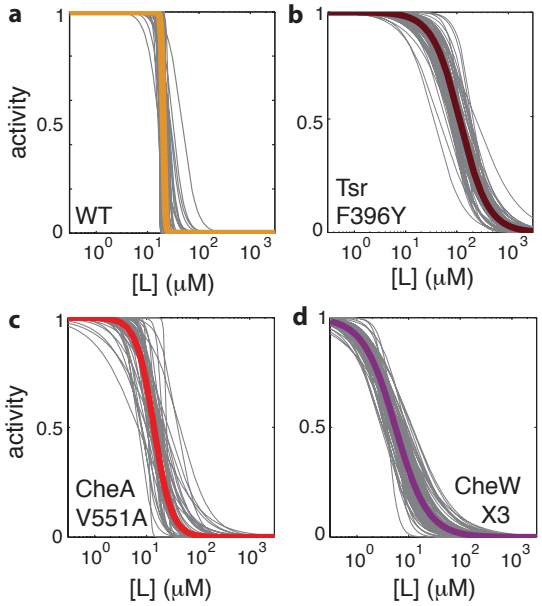

Figure 6.4: Family of dose response curves obtained from Hill curve fits to single cell FRET timeseries responding to L-serine reveal low cell-cell variation. **(a)** Tsr-WT (Tsr in UU2567, 103 cells) **(b)** Tsr-F396Y (in UU2567, 81 cells) **(c)** Family of dose response curves obtained from CheA V551A mutant cells (Tsr in UU2933, 42 cells). **(d)** CheW^{X3} mutant cells (Tsr in UU2869, 89 cells).

lations. In cells expressing a truncated version of CheB, in *tsr cheB* background (Fig. 6.5b), the response of a group of cells also was very shallow ($H_{pop} = 1.13$) but the single cells showed a range of sensitivities with both steep and shallow responses ($H = 1.9 \pm 2.6$, $K = 42 \pm 67$). The average single-cell value for K agrees very well with the population average, but the steepness of the response H is underestimated in single-cell experiments.

While some mutations clearly affect the cooperativity on the single cell level, and others may not, all experimental results show variability in the estimated sensitivity ($1/K$) and steepness H. In single-cell FRET experiments the single-cell information is obtained at a cost of signal to noise in compared to population-averaged experiments. Hence the obtained distributions for the fit parameters are likely to have a contribution from experimental noise. To estimate the level of variability due to experimental noise we generated artificial FRET time series to which we applied our dose response analysis. We assumed all cells have identical dose response curves with parameters equal to the estimates obtained for the population-averaged time series. We then add gaussian white noise to each of the

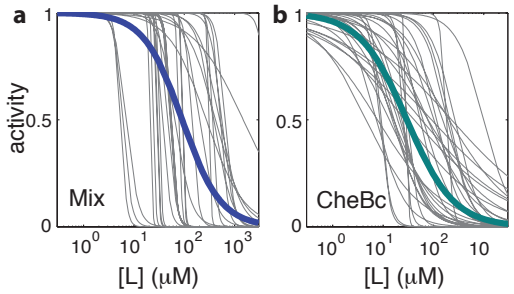

Figure 6.5: Family of dose response curves obtained from Hill curve fits to single cell FRET timeseries responding to MeAsp reveal large cell-cell variation **(a)** but for mutant cells expressing CheBc in a *tsr tap cheB* background (31 cells). **(b)** As in (a) but a mixture of three *tsr tap (cheR) cheB* strains with Tar-receptor modification fixed by mutations to QEQE,QQQQ,QEmQEm and grown separately (33 cells).

cells and fit a Hill function to the simulated data. The noise amplitude is chosen such to approximate the averaged mean squared error [MSE] of the simulated data fit to the average MSE of the single-cell data. The results of the simulation (Fig. 6.6) show that in the cooperativity defect mutants, the observed cell-to-cell variability is dominated by experimental noise. For the Hill curve steepness H it seems that all variability is explained by experimental error, while variability in the K exceeds variability expected by experimental noise. Also in the experiment with CheBc and the experiment with mixed strains there is a contribution of experimental noise, but the steepnesses obtained cannot be explained exclusively by shot noise.

6.4 Signalling response dynamics of chemoreceptor arrays

Some of the F396 mutants did not reveal a defect in cooperativity, but showed a slow temporal response to ligand in population averaged experiments. F396W in its natural QEQEE configuration is locked in an ON-state, meaning that the kinase activity is always active and not sensitive to ligand stimuli. However, measuring cells with Tsr-F396W in QEEEE configuration shifted the sensitivity down, to ± 300 μM. The dose response parameters (H=5.4, K=0.3 mM) indicated a decreased cooperativity compared to wild-type, but still much higher than the cooperativity defect mutants. Surprisingly, the response to sub-saturating stimuli was very slow while removing the same stimulus showed response timescale comparable to

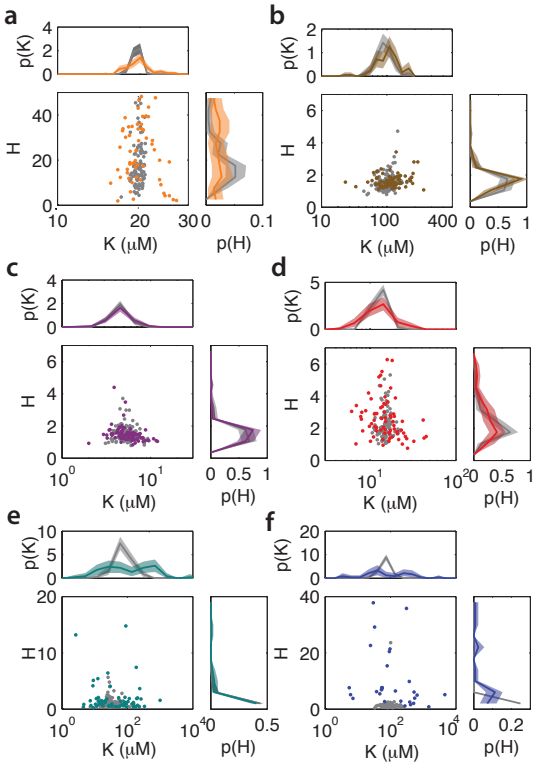

Figure 6.6: Comparison between measured and simulated data reveals the influence of experimental noise on fit parameters. For each single-cell FRET experiment, a simulated dataset was generated with the same parameters as the population-averaged dose response curve. To each of the simulated responses experimental white noise was added, and fit to a Hill function. Shown are scatter plots (square panels) and distributions (rectangular panels above and to the right of each square panel) of Hill fit parameters K and H from both experimental and simulated data. Colored points and lines indicate results for measurement data, gray lines and points are from a simulated data in which gaussian white noise is added to a dose response curve with parameters obtained from a fit to data on the population averaged time series (see main text, §6.3). Experimental data with a mse exceeding a determined threshold of 0.1 are removed from the analysis. **(a)** Tsr-WT (UU2567/pPA114), 103/108 cells **(b)** Tsr-F396Y, 81/84 cells **(c)** CheW-X3, 89/93 cells **(d)**, CheA-V551A, 77/120 cells **(e)**, CheBc in *tsr tap cheB* background (VS140), 64/141 cells **(f)** and the mixing experiment, 33/41 cells

wild-type. Interestingly, measuring in CheW-X3 background [149], preventing large array formation, the slow timescale disappeared (J.S. Parkinson, personal communication). These phenomena may reveal new insights on how the signal is propagated between core units of the chemosensory arrays influence the signal processing: since the discovery of chemoreceptor array core units, the question has emerged how the signal is transduced from one core unit to another. While virtually all experiments on chemoreceptor arrays have been concerned with static signalling parameters of the ligand response (such as dose response parameters), with temporal dynamics originating only by adaptation, studying the response dynamics (e.g. rate of change in activity) could provide important information on the mechanism of signal transduction. However, as is the case for the experiments described above, many population-averaged experiments average out single-cell dynamic responses. In analogy to the relation between population average and single cell dose response curves (Fig 6.2, only here considering activity as a function of time instead of ligand concentration) one can ask if this slow decay of cells expressing Tsr-F396W is a single cell property, or that the activity of a single cell decays rapidly with a delay which is variable from cell to cell.

6.4.1 Tsr mutant exhibits slow response to ligand stimuli

With population FRET, we observed the decay of cells expressing only the chemoreceptors Tsr-WT or the mutant Tsr-F396W from an inducable plasmid in CheRB- background (UU2567) and found that the response to an intermediate stimulus is slow (Fig. 6.7). A population of cells expressing F396W responded, defined as the time to reach half maximum of the response, in 200 s to a subsaturating stimulus, while responding to a saturated stimulus in 15 s. Tsr-WT cells responded in 80 and 10 s, respectively. Surprisingly, the response time of cells expressing Tsr-WT was still significantly longer than one would expect based on the finite exchange time of ligand in the flow cell. The latter was calculated by approximating the exchange dynamics of the flow cell by a fluorescence dye at a flow speed of 600 μL/min [64]with a sigmodial curve, and a estimate of a dose response curve with K=30 μM and H=5 (conservative estimate) for the cells. The timescale of the Tsr-WT cells is also large compared to the saturating stimulus. This raises the question wether the slow timescales of Tsr-F396W and Tsr-WT are related, or that there are qualitatively different mechanisms underlying this quantitative difference. One possibility is that the population-averaged response looks very similar, while the single-cell responses are very different. Hence we measured both genotypes with single-cell FRET, we can measure the single-cell responses as a function of time and try to see if the similarity in slow responses of Tsr-WT and Tsr-F396W also exists on the single-cell level.

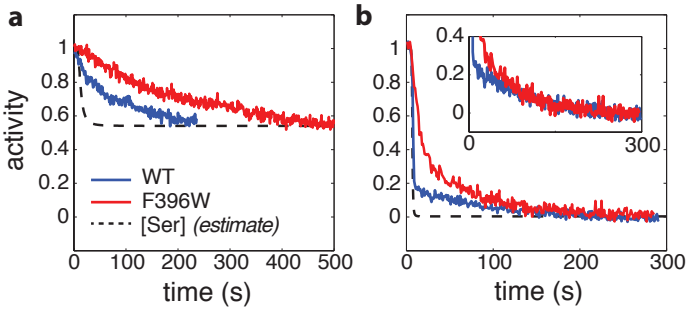

Figure 6.7: Population FRET timeseries on cells expressing Tsr-WT (blue) and Tsr-F396W (red) shows slow responses of kinase activity upon stimulation with attractant. **(a)** Response to sub-saturating stimuli, namely 20 uM (WT) and 300 uM (F39W). **b** Response to saturating stimili (both 10 mM Ser). Dashed line represents an estimation of the minimal cellular response time based on finite ligand exchange time in the flow-cell. Inset: same graph but with Tsr-F396W (red) response scaled to compare the decay shape with Tsr-WT (blue).

6.4.2 Individual Tsr-F396W cells respond slowly to ligand stimuli

When measuring the response of Tsr-WT cells (UU2567), as described in chapter 5, to prolonged stimulation with a subsaturating stimulus, we found that while the activity level of the population-averaged time series during the stimulus was stable, the single-cell time series showed large, often step-like fluctuations in time. We interpreted these step-like fluctuations as stochastic switchings of large and highly cooperative chemoreceptor arrays, between discrete states whose equilibrium probabilities are affected by ligand. In the first few hundred seconds after the stimulus is initiated (Fig. 6.8), we observed that some Tsr-WT cells do not respond, some respond immediately, and some respond with a delay. For the majority of the cells respondng with a delay, the slope of the temporal change in activity was much steeper than the slope response of the population-averaged time series. This raises the question if the Tsr-F396W has similar stochasticity in the timing of single-cell responses.

However, we measured the response of single-cells expressing Tsr-F396W to an intermediate and saturating ligand stimulus with single-cell FRET and found that individual time series seemed to behave qualitatively similarly to the population average (Fig. 6.9a), and large step-like fluctuations were absent. The population averaged decay looks approximately as a straight line on a log-linear or linear-log scale (Fig. 6.9b-c).

We chose to quantify the variability between cells by fitting the decay in the

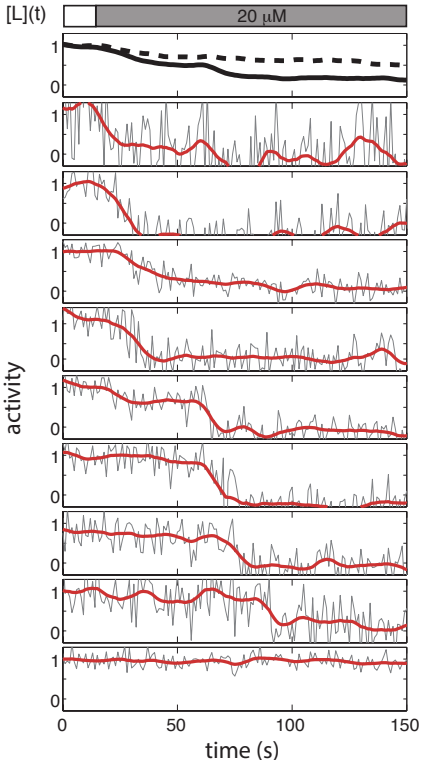

Figure 6.8: FRET experiment on Tsr-WT cells responding to a 20 μM serine stimulus shows fast activity decay in single cells. (Top panel) Population averaged time series of 9 selected cells showing delayed responses (black curve) and all 41 cells (dashed black curve). (Bottom panels) Raw single-cell time series of 9/41 cells (black) from a representative experiment with a low-pass filtered time series with a time window of 7s superimposed (red)

individual time series to exponential decay functions. The response to a sub-saturating stimulus can be well fitted wit a single exponential function for each cell i

$$a_i(t) = \exp[-t/\tau_i] + a_{c,i} \tag{6.2}$$

in which the decay timescale is τ_i and the activity levels at $a_{c,i}$. The fit is constrained such that τ and $a_{c,i}$ are non-negative. For saturating stimuli, some cells were more properly fit by a double exponential function

$$a_i(t) = \beta_i \exp\left[-t/\tau_{f,i}\right] + \gamma_i \exp\left[-t/\tau_{s,i}\right] \tag{6.3}$$

in which the $\tau_{f,i}$ and $\tau_{s,i}$ timescales are the fast and slow timescales, respectively. If they differ by less then two-fold, they are averaged to give a single timescale $\tau_{f,i}$, effectively collapsing to a single exponential fit. Several representative single-cell time series and corresponding fits are shown in Fig. 6.10.

From the estimates of τ_i, $\tau_{f,i}$ and $\tau_{s,i}$ obtained by fitting we can construct a family of curves representing response time series ensemble (Fig. 6.11), which

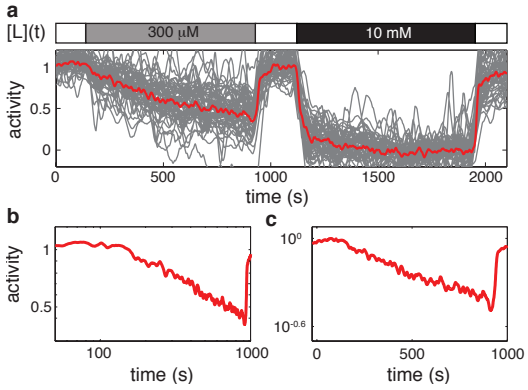

Figure 6.9: Single-cell FRET experiment on Tsr-F396W cells. **(a)** (top panel) Ligand exposure protocol. Cells are exposed to buffer (white), an intermediate stimulus of 300 μM (grey) and saturating stimulus of 10 mM (black). (bottom panel) FRET time series of 55 single cells (24s average filtered, grey) and population averaged time series (red). **(b)** Population-averaged response to 300 μM stimulus on logarithmic time axis. **(c)** Population-averaged response to 300 μM stimulus on logarithmic activity axis.

shows large variability from cell to cell in both the intermediate stimulus and saturating stimulus from a single experiment. In total, we found the average response time of F396W cells to an intermediate serine stimulus (300 μM), $\langle \tau_i \rangle$, to be 339 ± 348 s. For a saturating stimulus (10 mM), the short and fast timescales,$\langle \tau_{s,i} \rangle$ and $\langle \tau_{f,i} \rangle$, are found to be 151 ±128 and 16±20 s. On average 78 % of the response amplitude was given by the fast timescale. When performing similar fits to wildtype cells (Tsr in UU2567), we find for a saturating stimulus 51±33 and 8±17 as slow and fast timescales, respectively. The distributions of the timescales (Fig 6.12) clearly show differences timescale between conditions and strains, but that there is variability in each condition, that is in each case around one standard deviation from the mean.

Both the subsaturating stimulus as well as the saturating stimulus responses have a slow timescale component, and we wondered if these are related. The mean of these timescales is clearly different if one averages over many cells, but we wondered if these two quantities might be related on the single cell level. However, the correlation between the subsaturating response timescales τ_i and saturating response timescale τ_s, i (Fig. 6.13a) was not significant (ρ=0.05 ± 0.18, in which the uncertainty is calculated from bootstrapping). This indicates that the slow response to large stimuli is different in origin to the slow response to intermediate stimuli. While a slow response to large stimuli has been observed in Tar chemoreceptors [64], we note that the Tar chemoreptors can be stimulated

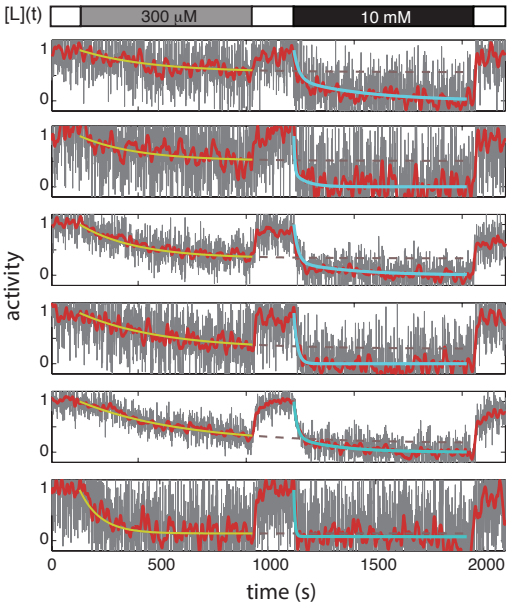

Figure 6.10: FRET decay upon stimulation in F396W are well described by exponential decay functions. (top panel) Ligand exposure protocol. Cells are exposed to buffer (white), an intermediate stimulus of 300 μ (grey) and saturating stimulus of 10 mM (black). (bottom panels) Shown are six representative single cell time series from a single experiment, in which the raw time series (grey) is shown together with 5s moving average filter (red). The response to the sub-saturating stimulus is fitted with a single exponential (yellow) and the saturating stimulus response is fitted to a double exponential, both to the single cell raw time series.

by a αmethyl-aspartate [MeAsp], a non-metabolizable homolog of aspartate, we use serine to stimulate the Tsr receptors, which could induce metabolic changes that affect kinase activity on longer timescales. A non-metabolizable analog of L-serine, α-aminoisobutyrate [AmBu], has been reported [125], but in FRET experiments with cells expressing Tsr-WT we could not observe an attractant responses to AmBu up to concentrations of 10 mM (data not shown).

What determines the variability in timescales? We wondered if this timescale would depend on the activity level the cell reaches during the stimulus, since the response to sub-saturating and saturating stimuli implies that this plays an important role. When we inspected the correlation between the extrapolated steady-state activity level from the fit ($a_{c,i}$), the correlation is weak but significantly negative (ρ=-0.25 ±0.18). However, when we normalized the response to the sub-saturating

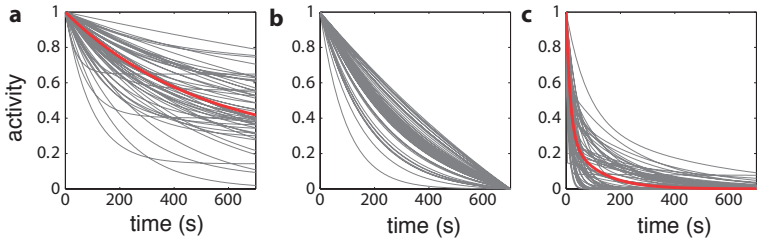

Figure 6.11: Family of response time series obtained from fit to single cell FRET time series (55 cells, grey) from a single experiment together with the fit to the population average (red) show variability in single-cell responses. **(a)** Family of response curves to the sub-saturating response. **(b)** Family of responses for sub-saturating response, each time series normalized to the response amplitude measured at the time of stimulus removal. **(c)** Family of responses to and saturating stimulus.

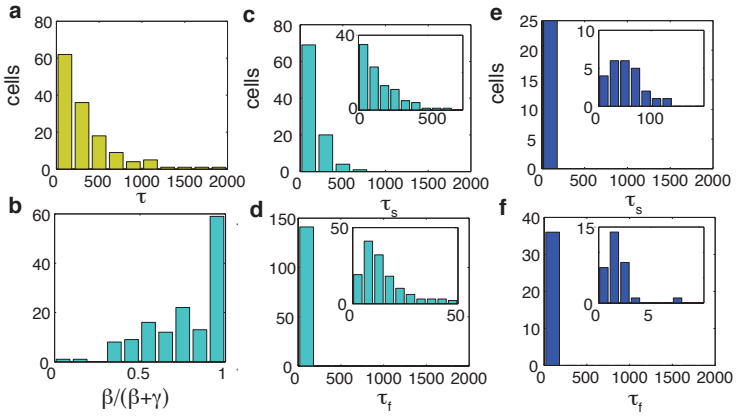

Figure 6.12: Histograms of response timescales of cells expressing Tsr F396W (141 cells from 3 independent experiments) and Tsr-WT (37 cells, 1 experiment) to sub- and saturating stimuli of L-serine, obtained from single and double exponential fits to the single cell FRET timeseries. **(a)** Timescale τ as the response to sub-saturating (300 μM Ser) stimulus of Tsr-F396W cells. **(b)** fraction of fast timescale amplitude in double exponential fit for Tsr-F396W cells responding to a saturating stimulus. **(c)** Slow timescale τ_s) from double exponential fit to 96 cells expressing Tsr-F396W response to saturating (10 mM Ser) stimulus. In 45 cells there was no slow timescale present. **(d)** Fast timescale τ_f from double exponential fit to F396W response to saturating (10 mM Ser) stimulus. **(e)** Slow timescale τ_s from double exponential fit to 25/37 Tsr-WT cells response to saturating (10 mM Ser) stimulus. For 12/37 cells there was no slow timescale. **(f)** Fast timescale τ_f) from double exponential fit to 37 Tsr-WT cells response to saturating (10 mM Ser) stimulus.

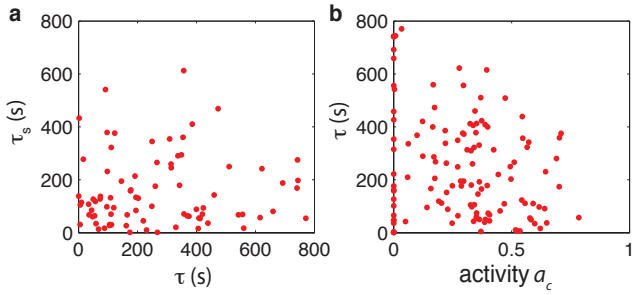

Figure 6.13: Correlations between parameters in F396W response. **(a)** Correlations between the response timescale of intermediate stimulus τ and slow response timescale to saturating stimulus τ_s of 81 cells. ρ=0.05 ± 0.18, in which the latter number represents the 95% confidence interval obtained from bootstrapping. **(b)** Correlations between the activity before removing the subsaturating stimulus (grey), or extrapolated from the fit (red), and the response timescale of intermediate stimulus τ for 125 cells. Cells with a response timescale larger than the stimulus duration (800s) were excluded.The correlation coefficient is calculated for the extrapolated activity data, ρ=-0.25 ±0.17

stimulus time series of each cell to its response amplitude the variability seems much lower (Fig. 6.11b).

While the activity response to stimuli in time can be well described by exponential decay, we also noted linearity of the activity versus logarithmic time. Logorathmic time dynamics have been observed in a homo-FRET study, in which the receptor packing is measured in a population of cells [64]. This study found that the receptor packing decays linearly with the logarithm of time. Single-cell FRET time series of kinase activity observe that if each curve is normalized to its response amplitude to the intermediate 300 μM stimulus, variability decreases, although not each single-cell time series falls on this curve (Fig. 6.14). This suggests that the main variability in the response to intermediate stimuli is determined by its response amplitude, presumably caused by cell-cell variability in the half-maximum responses of cells, and the response shape is actually quite similar, but with some additional variability. Furthermore, the low variability in response dynamics independent from response amplitudes, agrees with the low variability in the receptor packing response of different populations responding to different stimulus sizes. This implies the activity decay in Tsr-F396W is slow because it is limited by large arrays breaking apart, and this is consistent with the observation the slow timescale disappears in CheW-X3 background (JS Parkinson, personal communication).

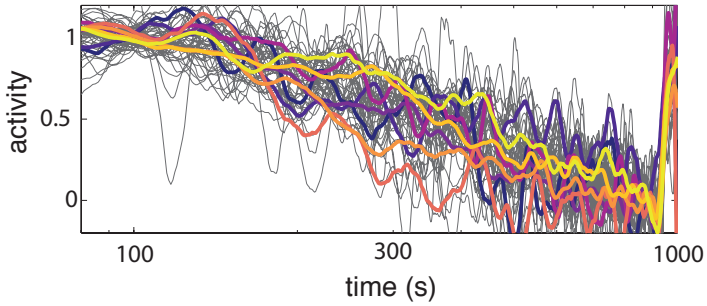

Figure 6.14: Single-cell responses to a sub-saturating stimulus and normalized to response amplitude and plotted versus logarithmic time show reduced variability. FRET time series on a logarithmic time axis, of single cells expressing Tsr-F396W responding to 300 μM stimulus and each normalized by the response amplitude of each cell. In total 52/59 cells are shown (grey) with 9 cells highlighted (colored curves). Time series are low-pass filtered with a window size of 15 s. Cells with a small response were removed from the analysis.

6.5 Discussion

With single-cell FRET, we have been able to measure single cell responses of kinase activity to extracellular attractant concentrations, both changes in activity over time as well as equilbrium activity levels for different concentrations of attractant.

6.5.1 Cooperativity defects in dose response curves

We measured dose response curves of single cells and thereby confirmed the single-cell cooperativity defects in two of the CheA-CheW interface 2 mutants, as well as one Tsr-F396 mutant. The cell-to-cell variability in the dose response parameters (K and H) is lower than the precision which these parameters can be determined given experimental noise, indicating that the population-averaged results are representative of single cell behavior. This raises two related questions. The first is whether these experimental results on single-cells could have been somehow predicted by the population averaged response, and the second if we can extrapolate these results on the dose response curves to any other genotype exhibiting low cooperativity in population-averaged experiments. The cell to cell variabilty in K for Tsr-WT cells is relatively low, with a geometric coefficient of variance, given as the geometric coefficient of variance $\mathrm{CV}^{\mathrm{geo}} = \sqrt{\exp\left[s[\ln x]^2\right] - 1}$, with $s[x]$ the standard deviation, of 0.14. Cells expressing all five chemoreceptors show much higher variability ($\mathrm{CV}^{\mathrm{geo}} \approx 0.49$), which is mostly determined by cell to cell

variability in Tar/Tsr ratio due to stochastic gene expression (see Chapter 3). In the case of a single receptor species, the variability cannot be explained by variability in chemoreceptor species but in our experiments, is dominated by experimental noise. How likely is it that the cooperativity defects can be explained only by cell-to-cell variability in K? If one assumes a single-cell Hill curve coefficient H of 20 (the average value for H in Tsr-WT cells) and a log-normal distributed K, this requires a CV^{geo} of 0.9 to generate a population Hill curve similar to CheA-V551A ($\approx$ 2.5), or 1.5 to be similar to CheW-X3 or Tsr-F396Y ($\approx$ 1.4). Though not impossible, these noise levels are higher than typically found in stochastic gene expression, since stochastic gene expression CV's for highly expressed level proteins typically do not exceed 0.3 [202]. Hence based on estimates of the variability of dose-response parameters, it seems unlikely that the decrease in cooperativity at the population level can be completely explained by cell-to-cell variability in population, but single-cell experiments are still required to establish that the average single-cell hill curve steepness in the cooperativity defective mutants is close to the population-averaged value. In general, unless there is for an additional noise generating or amplification mechanism, it is quite reasonable to expect that cooperativity defect mutants with similar (population) cooperativity defects as measured here also show a defect at the single-cell level.

Evidence from cluster-imaging and crosslinking experiments suggest that the mechanism by which the interface 2 mutants disrupt cooperativity on the single cell level is by prevention of large cluster formations. The mechanism of decreased cooperativity of Tsr-F396Y is not known, but preliminary experiments with fluorescently labeled Tsr-F396Y chemoreceptors indicate that cluster formation is also defective in these cells (K. Scherer, personal communication), which is perhaps not surprizing given the location of the mutation, close to the CheA-CheW baseplate. Therefore, we assume that the confirmation of a single-cell cooperativity defect because of impaired clustering extends to other mutations that show impaired clustering, but have not been measured on the single cell level (such as interface 2 mutants CheA-L545S and CheA-Y558G [149]). However, for other mutations with lower population-cooperativity at residues located far away from the CheA-CheW baseplate it is less clear how they would disrupt clustering, and it would be interesting to see if they have intact clusters. If a cooperativity mutant demonstrates additional phenotypes indicative of a different mechanism for low cooperativity, for example intact clusters in combination with reduced cooperativity, this would be a good candidate for further testing with single-cell FRET.

By far the largest variability in K we found in an isogenic population was in cells expressing CheBc in*tsr tap cheB* background (CV^{geo}=2). We found that cells expressing phosphorylation defective mutants (like CheBc) in wildtype background (VS124) have larger variability in steady-state kinase activity (see chapter 3). Both the steady-state activity level and K are determined by the

receptor methylation state. Since CheR and CheB work close to saturation, the steady-state methylation state becomes ultransensitive to variability in the CheR/CheB ratio and hence amplifies noise orginating from stochastic gene expression, leading to considerable cell-cell variability in steady-state activity ($CV \approx 1$). Hence the variability in single-cell dose response curve parameters K and H is likely caused by the lack of phosphorylation feedback.

Many open questions remain on the nature of signal amplification in chemosensory arrays. It is still impossible to predict the cooperativity of the cellular response from only the structure. In cells with only core units (CheAW interface 2 mutants), one could expect the cooperativity to be as high as 6 (one receptor binding pocket per dimer). Similarly, cells with intact chemoreceptor arrays can have Hill curve coefficients that are much higher. Although in other dose response experiments we do see that Hill curve coefficients can be high (see Chapter 3), as is also suggested by observed two-state switching (see chapter 5), it seems plausible that the cooperativity has an upper limit that is lower than the number of units in the array. Of course, there are few examples in biology where cooperativity can be directly inferred from the structure of the reaction components. Even in the classic example of cooperativity, the binding of oxygen to haemoglobin, there is not a clear relation between the number of binding sites (4) and observed Hill curve steepness (1.5-3.2) [227], although the difference between upper limit and actual value of the hill curve steepness is less than in the case of the chemoreceptor arrays.

6.5.2 Measurements of slow activity decay

In addition to measurements of equilibrium activity levels as a function of ligand concentrations, we have also studied the activity decay time in response to stimuli. In cells expressing Tsr-F396W we have observed a slow decay in kinase activity upon stimulation with a saturating stimulus, while stimulating with a saturating stimulus resulted in a fast response. In Tsr+ cells we have observed a qualitatively similar but much smaller effect on the population level, while single-cell responses were generally rapid and fluctuating. We did not observe any fluctuations or rapid decrease in Tsr-F396W cells. Hence thanks to single-cell resolution we are able to distinguish the two different forms of decay. If we interpret the slow decay as receptor clusters breaking apart into smaller units, which is consistent with the observation that the slow timescale disappears in CheW-X3 background, as well as with a previous observation (with Tar receptors) that clusters fall apart after prolonged stimulation (F. Anquez and J. Solari, personal communication).

The origin of the cell-to-cell variability in response timescales for Tsr-F396W in the decay timescale remains to be identified, while this variability in timescales seems to be connected to the response amplitude to an intermediate stimulus. If the interpretation that the decay of activity is caused by large chemoreceptor arrays

breaking apart, one potential cause of cell-to-cell variability is the cluster size distribution. Cells with many large clusters might require more time for cluster dispersal. Alternatively, there is the possibility that within the chemoreceptor array structures there can be structural defects that differ from cell to cell. (e.g. some core units are closer connected than others). Some of these differences might be attributed to different expression level ratios of components of the chemoreceptor array.

Finally, the experiments in this chapter confirm the importance of the formation of large chemoreceptor array for signal amplification, and also reveal a crucial role of the array formation in the activity response timescale. These experiments further establish single-cell FRET as a quantitative *in vivo* measurement technique that can discriminate different ligand sensing phenotypes which are unresolved in ensemble-averaged experiments.

6.6 Methods

The experiments in this chapter were generally performed as described in chapter 2, which includes a list of the strains and plasmids used in this study (§2.4). For all single-cell FRET experiments in this chapter, cells were immobilised with anti-FliC antibodies (a gift from Howard Berg). Interface 2 mutants were expressed from the chromosome (strains constructed by G. Piñas), Tsr chemoreceptor was expressed from pPA114 plasmid with 0.6 μM NaSal induction). In all experiments concerning F396W, the Tsr is in the EEQEE modification state, while Tsr-WT was always in its native QEQEE state. FRET plasmid was pSJAB106 and induced with 50 μM IPTG.

This chapter was the result of a collaboration with J.S. Parkinson and G. Piñas (University of Utah, USA) and we thank both for materials, sharing experimental data and discussions, and we thank J.S. Parkinson for a critical reading of this chapter. We thank Simone Boskamp for cell culture and Francesca van Tartwijk for the FRET measurements on Tsr-F396W .

To compare our results with previous experiments we always stimulate the cells with a large (10 mM serine) stimulus before or at the start of each experiment. If no stimulus is given, population-averaged FRET results indicated that the response to the first and second large stimulus in F396W were not identical, shifting the sensitivity to serine of the population down from ≈ 3 mM to ≈0.3 mM.

References

[1] M Ackermann. A functional perspective on phenotypic heterogeneity in microorganisms. *Nat. Rev. Microbiol.*, 13:497–508, 2015.

[2] J Adler. Chemotaxis in bacteria. *Science*, 153(3737):708–716, August 1966.

[3] U Alon, MG Surette, N Barkai, and S Leibler. Robustness in bacterial chemotaxis. *Nature*, 397(6715):168–171, 1999.

[4] P Ames, CA Studdert, RH Reiser, and JS Parkinson. Collaborative signaling by mixed chemoreceptor teams in escherichia coli. *PNAS*, 99:7060–65, 2002.

[5] DN Amin and GL Hazelbauer. Chemoreceptors in signalling complexes: shifted conformation and asymmetric coupling. *Mol Microbiol.*, 78:1313–23, 2010.

[6] G.S. Anand and A.M. Stock. Kinetic basis for the stimulatory effect of phosphorylation on the methylesterase activity of cheb. *Biochemistry*, 41:6752–6760, 2002.

[7] S Asakura and H Honda. Two-state model for bacterial chemoreceptor proteins. the role of multiple methylation. *J Mol Biol*, 176:349–69, 1984.

[8] F Bai, RW Branch, DV Nicolau, T Pilizota, BC Steel, PK Maini, and RM Berry. Conformational spread as a mechanism for cooperativity in the bacterial flagellar switch. *Science*, 327:685–9, 2010.

[9] N Barkai, U Alon, and S Leibler. Robust amplification in adaptive signal transduction networks. *C. R. Acad. Sci. Paris*, IV:871–877, 2001.

[10] N. Barkai and S. Leibler. Robustness in simple biochemical networks. *Nature*, 387(6636):913–917, 1997.

[11] R Belas. Biofilms, flagella, and mechanosensing of surfaces by bacteria. *Trends Microbiol.*, 22:517–527, 2014.

[12] HC Berg. Motile behavior of bacteria. *Physics Today*, 53:24, 2000.

[13] HC Berg and DA Brown. Chemotaxis in escherichia coli analysed by three-dimensional tracking. *Nature*, 239(5374):500–504, 1972.

[14] HC Berg and PM Tedesco. Transient Response to Chemotactic Stimuli in Escherichia coli. *PNAS*, 72(8):3235–3239, August 1975.

[15] T Bergmiller, AMC Andersson, K Tomasek, E Balleza, DJ Kiviet, R Hauschild, G Tkacik, and CC Guet. Biased partitioning of the multidrug efflux pump acrab-tolc underlies long-lived phenotypic heterogeneity. *Science*, 356:311–15, 2017.

[16] W.J. Blake, M Kaern, C Cantor, and J.J. Collins. Noise in eukaryotic gene expression. *Nature*, 422:633–37, 2003.

[17] SM Block, JE Segall, and HC Berg. Impulse responses in bacterial chemotaxis. *Cell*, 31:215–26, 1982.

[18] AJ Boersma, IS Zuhorn, and B Poolman. A sensor for quantification of macromolecular crowding in living cells. *Nat. Meth.*, 12:227–229, 2015.

[19] MA Boin, MJ Austin, and CC Häse. Chemotaxis in vibrio cholerae. *FEMS Microbiol Lett*, 239:1–8, 2004.

[20] A Borczuk, A Staub, and J Stock. Demethylation of bacterial chemoreceptors is inhibited by attractant stimuli in the complete absence of the regulatory domain of the demethylating enzyme. *Biochem Biophys Res Commun.*, 141:918–23, Dec 1986.

[21] D Bray and T Duke. Conformational spread: The propagation of allosteric states in large multiprotein complexes. *nnu. Rev. Biophys. Biomol. Struct.*, 33:53–73, 2004.

[22] D Bray, MD Levin, and CJ Morton-Firth. Receptor clustering as a cellular mechanism to control sensitivity. *Nature*, 393(6680):85–88, 05 1998.

[23] A Briegel, P Ames, JC Gumbart, CM Oikonomou, JS Parkinson, and GJ Jensen. The mobility of two kinase domains in the escherichia coli chemoreceptor array varies with signalling state. *Mol. Microbiol.*, 89:831–41, 2013.

[24] A Briegel and G Jensen. Progress and potential of electron cryotomography as illustrated by its application to bacterial chemoreceptor arrays. *Ann. Rev. Biophys.*, 4:1–21, 2017.

[25] A Briegel, X Li, AM Bilwes, KT Hughes, GJ Jensen, and BR Crane. Bacterial chemoreceptor arrays are hexagonally packed trimers of receptor dimers networked by rings of kinase and coupling proteins. *PNAS*, 109:3767, 2012.

[26] A Briegel, D.R. Ortega, E.I Tocheva, K. Wuichet, Z. Li, S. Chen, A Mueller, C.V. Iancu, G.E. Murphy, M. J Dobro, I.B. Zuhlin, and G.J. Jensen. Universal architecture of bacterial chemoreceptor arrays. *PNAS*, 106:17181–86, 2009.

[27] L Cai, N Friedman, and S Xie. Stochastic protein expression in individual cells at the single molecule level. *Nature*, 440:358–62, 2006.

[28] RE Campbell, O Tour, AE Palmer, PA Steinbach, GS Baird, DA Zacharias, and Tsien RY. A monomeric red fluorescent protein. *PNAS*, 99:7877–82, 2002.

[29] A. Celani and M. Vergassola. Nonlinearity, fluctuations, and response in sensory systems. *Phys. Rev. Lett.*, 108:258102+, 2012.

[30] G Chalancon, CNJ Ravarani, S Balaji, A Martinez-Arias, L Aravind, R Jothi, and MM Babu. Interplay between gene expression noise and regulatory network architecture. *Trends in Genetics*, 28:221, 2012.

[31] FFV Chevance and KT Hughes. Coordinating assembly of a bacterial macromolecular machine. *Nat. Rev. Microbiol.*, 6:455–65, 2008.

[32] GS Chilcott and KT Hughes. Coupling of flagellar gene expression to flagellar assembly in salmonella enterica serovar typhimurium and escherichia coli. *Microbiol Mol Biol Rev*, 64:694–708, 2000.

[33] M Christen, HD Kulasekara, B Christen, BR Kulasekara, LR Hoffman, and SI Miller. Asymmetrical distribution of the second messenger c-di-gmp upon bacterial cell division. *Science*, 328:1295–97, 2010.

[34] D Clausznitzer and RG Endres. Noise characteristics of the escherichia coli rotary motor. *BMC Systems Biology*, 5:151, 2011.

[35] D Clausznitzer, O. Oleksiuk, L Løvdok, V Sourjik, and RG Endres. Chemotactic Response and Adaptation Dynamics in Escherichia Coli. *PLoS Comp. Biol.*, 6(5):e1000784+, 2010.

[36] P Cluzel, M Surette, and S Leibler. An ultrasensitive bacterial motor revealed by monitoring signaling proteins in single cells. *Science*, 287(5458):1652–1655, March 2000.

[37] R Colins and C Sourjik. Emergent properties of bacterial chemotaxis pathway. *Curr. Op. Microbiol.*, 39:24–33, 2017.

[38] K Colville, N Tompkins, AD Rutenberg, and MH Jericho. Effects of poly(L-lysine) substrates on attached Escherichia coli bacteria. *Langmuir*, 26(4):2639–2644, 2010.

[39] MJ Costello, RM May, and NE Stork. Can we name earth's species before they go extinct? *Nature*, 339:413–416, 2013.

[40] PJ Cranfill, BR Sell, MA Baird, JR Allen, Z Lavagnino, HM de Gruiter, GJ Kremers, MW Davidson, A Ustione, and DW Piston. Quantitative assessment of fluorescent proteins. *Nat. Meth.*, 13(7):557–562, 2016.

[41] F. Crick. Central dogma of molecular biology. *Nature*, 227:561–563, 1970.

[42] Crocker and Grien. Methods of digital video microscopy for colloidal studies. *Journal of colloid and interface science*, (179):298–310, 1996.

[43] ME Csete and JC Doyle. Reverse engineering of biological complexity. *Science*, 295:1664–9, 2002.

[44] CJ Davidson and MG Surette. Individuality in bacteria. *Ann. Rev. Genet.*, 42:253–268, 2008.

[45] M Delbrück. Statistical fluctuations in autocatalytic reactions. *The Journal of Chemical Physics*, 8, 1940.

[46] N Dhar and JD McKinney. Microbial phenotypic heterogeneity and antibiotic tolerance. *Curr. Opin. Microbiol.*, 1:30–38, 2007.

[47] D Di Paolo, O Afanzar, JP Armitage, and RM Berry. Single-molecule imaging of electroporated dye-labelled chey in live escherichia coli. *Philos. Trans. R. Soc. Lond. B*, 371, 2016.

[48] S. Djordevic, P.N Goudreau, Q. Xu, A.M. Stock, and A.H West. Structural basis for methylesterase cheb regulation by a phosphorylation-activated domain. *PNAS*, 95:1381–1386, 1998.

[49] YS Dufour, S Gillet, NW Frankel, DB Weibel, and T Emonet. Direct correlation between motile behavior and protein abundance in single cells. *PLoS Comp. Biol.*, 12, 2016.

[50] TA Duke, N Le NovÃ¨re, and Bray D. Conformational spread in a ring of proteins: a stochastic approach to allostery. *J Mol Biol.*, 308:541–53, 2001.

[51] TAJ Duke and D Bray. Heightened sensitivity of a lattice of membrane receptors. *PNAS*, 96:10104–8, 1999.

[52] MJ Dunlop, RS Cox III, JH Levine, RM Murray, and MB Elowitz. Regulatory activity revealed by dynamic correlations in gene expression noise. *Nat. Gen.*, 40:1493–8, 2008.

[53] A Eldar and MB Elowitz. Functional roles for noise in genetic circuits. *Nature*, 467(7312):167–173, September 2010.

[54] J Elf and M. Ehrenberg. Spontaneous separation of bi-stable biochemical systems into spatial domains of opposite phases. *Syst. Biol*, 1:230–236, 2004.

[55] M. B. Elowitz, A. J. Levine, E. D. Siggia, and P. S. Swain. Stochastic gene expression in a single cell. *Science*, 297(5584):1183–1186, 2002.

[56] MB Elowitz and S Leibler. A synthetic oscillatory network of transcriptional regulators. *Nature*, 403:335–8, 2000.

[57] T. Emonet and P. Cluzel. Relationship between cellular response and behavioral variability in bacterial chemotaxis. *PNAS*, 105(9):3304–3309, March 2008.

[58] R. G Endres, O. Oleksiuk, C. H. Hansen, Y. Meir, V. Sourjik, and N. S. Wingreen. Variable sizes of escherichia coli chemoreceptor signaling teams. *Mol. Sys. Biol.*, 4(211):211, 2008.

[59] RG Endres and NS Wingreen. Precise adaptation in bacterial chemotaxis through assistance neighbourhoods. *PNAS*, 103:13040–44, 2006.

[60] Annette H. Erbse and Joseph J. Falke. The core signaling proteins of bacterial chemotaxis assemble to form an ultrastable complex. *Biochemistry*, 48(29):6975–6987, 2009.

[61] A Esposito, M Gralle, MA Dani, D Lange, and Wouters FS. phlameleons: a family of fret-based protein sensors for quantitative ph imaging. *Biochemistry*, 47:13115–26, 2008.

[62] JJ Falke, RB Bass, SL Butler, SA Chervitz, and MA Danielson. The two-component signaling pathway of bacterial chemotaxis: a molecular view of signal transduction by receptors, kinases, and adaptation enzymes. *Ann. Rev. Cell Dev. Biol.*, 13:457–512, 1997.

[63] M Flores, TS Shimizu, PR ten Wolde, and F Tostevin. Signaling noise enhances chemotactic drift of *E. coli*. *Phys. Rev. Lett.*, 109:148101+, 2012.

[64] V. Frank and A. Vaknin. Prolonged stimuli alter the bacterial chemosensory clusters. *Mol. Microbiol.*, 88:634–44, 2013.

[65] NW Frankel, W Pontius, YS Dufour, J Long, L Hernandez-Nunez, and T Emonet. Adaptability of non-genetic diversity in bacterial chemotaxis. *eLife*, pages e03526+, 2014.

[66] N. Friedman, L. Cai, and X. S. Xie. Linking stochastic dynamics to population distribution: an analytical framework of gene expression. *Phys. Rev. Lett.*, 97(16), 2006.

[67] H Fukuoka, T Sagawa, Y Inoue, H Takahashi, and A Ishijima. Direct imaging of intracellular signaling components that regulate bacterial chemotaxis. *Science Sign.*, 7, 2014.

[68] DT Gillespie. The mathematics of brownian motion and johnson noise. *American Journal of Physics*, 64:225–240, 1996.

[69] A Goldbeter and DE Koshland. An amplified sensitivity arising from covalent modification in biological systems. *PNAS*, 78(11):6840–6844, 1981.

[70] I Golding, J Paulsson, SM Zawilski, and EC Cox. Real-time kinetics of gene activity in individual cells. *Cell*, 123:1025–36, 2005.

[71] D Greenfield, AL McEvoy, H. Shroff, GE Crooks, NS Wingreen, E Betzig, and J Liphardt. Self-organization of the escherichia coli chemotaxis network imaged with super-resolution light microscopy. *PLoS Biology*, 7, 2009.

[72] XS Han and JS Parkinson. An unorthodox sensory adaptation site in the e. coli serine chemoreceptor. *Journal of Bacteriology*, 196:641–649, 2014.

[73] A Hilfinger, T.M Norman, G. Vinnicombe, and J. Paulsson. Constraints on fluctuations in sparsely characterized biological systems. *Phys. Rev. Lett.*, 116:058101, 2016.

[74] R Holliday. Epigenetics: a historical overview. *Epigenetics*, 1:76–80, 2006.

[75] B Hu and Y Tu. Coordinated switching of bacterial flagellar motors: Evidence for direct motor-motor coupling? *Phys. Rev. Lett.*, 110:158703, 2013.

[76] D Huh and J Paulsson. Non-genetic heterogeneity from stochastic partitioning at cell division. *Nature Genetics*, 43, 2011.

[77] E. Ising. Beitrag zur theorie des ferromagnetismus. *Z. Physik*, 31:253, 1925.

[78] CW Jones and JP Armitage. Positioning of bacterial chemoreceptors. *Trends in Microbiology*, 23:247, 2015.

[79] M Kærn, T.C. Elston, W.J. Blake, and J.J. Collins. Stochasticity in gene expression: from theories to phenotypes. *Nat. Rev. Genetics*, 6:451–64, 2005.

[80] Y. Kalinin, S. Neumann, Victor S., and M. Wu. Responses of Escherichia coli bacteria to two opposing chemoattractant gradients depend on the chemoreceptor ratio. *Journal of Bacteriology*, 192(7):1796–1800, 2010.

[81] JM Keegstra, K Kamino, F Anquez, Lazova MD, T Emonet, and TS Shimizu. Phenotypic diversity and temporal variability in a bacterial signaling network revealed by single-cell fret. *eLife*, 6:e27455, 2017.

[82] BU Keller, Hartshorne RP, JA Talvenheimo, WA Catterall, and M Montal. Sodium channels in planar lipid bilayers. channel gating kinetics of purified sodium channels modified by batrachotoxin. *J Gen Physiol.*, 88:1–23, 1986.

[83] JB Keller. The probability of heads. *The Am. Math. Monthly*, 93:191–7, 1986.

[84] D. Kentner and V. Sourjik. Dynamic map of protein interactions in the escherichia coli chemotaxis pathway. *Mol. Sys. Biol.*, 2009.

[85] JE Keymer, RG Endres, M Skoge, Y Meir, and NS Wingreen. Chemosensing in Escherichia coli: Two regimes of two-state receptors. *PNAS*, 103(6):1786–1791, February 2006.

[86] CM Khursigara, G Lan, S Neumann, X Wu, S Ravindran, MJ Borgnia, V Sourjik, J Milne, Y Tu, and S Subramaniam. Lateral density of receptor arrays in the membrane plane influences sensitivity of the e. coli chemotaxis response. *EMBO J*, 30:1719–29, 2011.

[87] H Kitano. Biological robustness. *Nat. Rev. Genetics*, 5:826–37, 2004.

[88] S Kitanovic, P. Ames, and J.S. Parkinson. A trigger residue for transmembrane signaling in the escherichia coli serine chemoreceptor. *J. Bacteriology*, 197:2568–79, Aug 2015.

[89] DJ Kiviet, P Nghe, N Walker, S Boulineau, V Sunderlikova, and SJ Tans. Stochasticity of metabolism and growth at the single-cell level. *Nature*, 514:376–9, 2014.

[90] M. Kollmann, L. Løvdok, K. Bartholomé, J. Timmer, and V. Sourjik. Design principles of a bacterial signalling network. *Nature*, 438(7067):504–507, 2005.

[91] E Korobkova, T Emonet, J. M. Vilar, TS Shimizu, and P Cluzel. From molecular noise to behavioural variability in a single bacterium. *Nature*, 428(6982):574–578, 2004.

[92] JR Kroll, J Tsiaxiras, and JS Van Zon. Multiple sources of variability drive a stochastic cell fate decision in c. elegans. *BioRxiv*, 2018.

[93] E. Kussell and S. Leibler. Phenotypic diversity, population growth, and information in fluctuating environments. *Science*, 309:2075–8, 2005.

[94] J.R. Lakowicz. *Principles of Fluorescence Spectroscopy*. Springer, New York City, USA, 3 edition, 2006.

[95] AJ Lam, F St-Pierre, Y Gong, JD Marshall, PJ Cranfill, MA Baird, MR McKeown, J Wiedenmann, MW Davidson, MJ Schnitzer, RY Tsien, and MZ Lin. Improving fret dynamic range with bright green and red fluorescent proteins. *Nat. Meth.*, 9:1005–12, 2012.

[96] G Lan, P Sartori, S Neumann, V Sourjik, and Y Tu. The energy-speed-accuracy trade-off in sensory adaptation. *Nature Physics*, 8:422–428, 2012.

[97] G Lan, S Schulmeister, V Sourjik, and Y Tu. Adapt locally and act globally: strategy to maintain high receptor sensitivity in complex environmentsi. *MSB*, 7(475), 2011.

[98] MD Lazova, T Ahmed, D Bellomo, R Stocker, and TS Shimizu. Response rescaling in bacterial chemotaxis. *PNAS*, 108(33):13870–75, 2011.

[99] I. Lestas, V. Glenn, and J. Paulsson. Fundamental limits on the suppression of molecular fluctuations. *Nature*, 467:174–178, Sep 2010.

[100] MD Levin, TS Shimizu, and D Bray. Binding and diffusion of cher molecules within a cluster of membrane receptors. *Biophys. J.*, 82:1809–17, 2002.

[101] G.W. Li, D. Burkhardt, C. Gross, and J. S. Weissman. Quantifying absolute protein synthesis rates reveals principles underlying allocation of cellular resources. *Cell*, 157(3):624–35, apr 2014.

[102] M. Li and G. L. Hazelbauer. Cellular stoichiometry of the components of the chemotaxis signaling complex. *J. Bacteriol.*, 186(12):3687–3694, June 2004.

[103] M Li and GL Hazelbauer. Adaptational assistance in clusters of bacterial chemoreceptors. *Mol. Microbiol.*, 56:1617–26, 2005.

[104] M Li and G.L. Hazelbauer. Core unit of chemotaxis signaling complexes. *PNAS*, 108:9390–5, 2011.

[105] LW Liang, R Hussein, DHS Block, and HN Lim. Minimal effect of gene clustering on expression in escherichia coli. *Genetics*, 193(2):453–465, 2013.

[106] L Liberman, HC Berg, and V Sourjik. Effect of chemoreceptor modification on assembly and activity of the receptor-kinase complex in *Escherichia Coli*. *J of Bacteriology*, 186(19):6643–46, August 2004.

[107] J C W Locke, J W Young, M Fontes, M J H Jimenez, and M B Elowitz. Stochastic Pulse Regulation in Bacterial Stress Response. *Science*, 334(6054):366–369, 2011.

[108] J. Long, SW Zucker, and T Emonet. Feedback between motion and sensation provides nonlinear boost in run-and-tumble navigation. *PLoS Comp. Biol.*, 13(3):e1005429, 2017.

[109] L Løvdok, K Bentele, N Vladimirov, A Müller, FS Pop, D Lebiedz, M Kollmann, and V Sourjik. Role of translational coupling in robustness of bacterial chemotaxis pathway. *PLoS One*, 7:e1000171, 2009.

[110] HP Lu, L Xun, and XS Xie. Single-molecule enzymatic dynamics. *Science*, 282:1877–82, 1998.

[111] A. Lupas and J. Stock. Phosphorylation of n-terminal regulatory domain activates the cheb methylesterase in bacterial chemotaxis. *J of Biological Chemistry*, 264:17337–17342, 1989.

[112] Webster MA. Evolving concepts of sensory adaptation. *F1000 Biology reports*, 4:21, 2012.

[113] JR Maddock and L Shapiro. Polar location of the chemoreceptor complex in the escherichia coli cell. *Science*, 259:1717–23, 1993.

[114] D Magde, E Elson, and WW Webb. Thermodynamic fluctuations in a reacting system: Measurement by fluorescence correlation spectroscopy. *Phys. Rev. Lett*, 29, 1972.

[115] L Mahadevan and EH Yong. Probability, physics and the coin toss. *Physics Today*, 64:66–67, 2011.

[116] R Mathis and M Ackermann. Response of single bacterial cells to stress gives rise to complex history dependence at the population level. *PNAS*, 113:4224–9, 2016.

[117] F Matthäus, M Jagodic, and J Dobnikar. E. coli superdiffusion and chemotaxis-search strategy, precision, and motility. *Biophys. J.*, 97:946–57, 2009.

[118] RM May. Simple mathematical models with very complicated dynamics. *Nature*, 261:459–67, 1976.

[119] TB McAnaney, W Zeng, CF Doe, N Bhanji, S Wakelin, Pearson DS, P Abbyad, X Shi, SG Boxer, and Bagshaw CR. Protonation, photobleaching, and photoactivation of yellow fluorescent protein: a unifying mechanism. *Biochem.*, 44:5510–24, 2005.

[120] PJ Mears, S Koirala, CV Rao, I Golding, YR Chemla, and M Laub. Escherichia coli swimming is robust against variations in flagellar number. *eLife*, 3, February 2014.

[121] BA Mello, LB Shaw, and Y Tu. Effects of receptor interaction in bacterial chemotaxis. *Biophys. J.*, 87:1578–95, 2004.

[122] BA Mello and Y Tu. Perfect and near-perfect adaptation in a model of bacterial chemotaxis. *Biophys. J.*, 84:2943–56, 2003.

[123] BA Mello and Y Tu. An allosteric model for heterogeneous receptor complexes: Understanding bacterial chemotaxis responses to multiple stimuli. *PNAS*, 102(48):17354–17359, 2005.

[124] BA Mello and Y Tu. Effects of adaptation in maintaining high sensitivity over a wide range of backgrounds for Escherichia Coli chemotaxis. *Biophys. J.*, 92(7):2329–2337, April 2007.

[125] R Mesibov and J Adler. Chemotaxis toward amino acids in escherichia coli. *J Bacteriol.*, 112:315–26, 1972.

[126] TL Min, Patrick J Mears, LM Chubiz, CV Rao, I Golding, and YR Chemla. High-resolution, long-term characterization of bacterial motility using optical tweezers. *Nat. Meth.*, 6(11):831–835, 2009.

[127] TL Min, PJ Mears, I Golding, and YR Chemla. Chemotactic adaptation kinetics of individual escherichia coli cells. *PNAS*, 2012.

[128] A Miyawaki, J Llopis, R Heim, JM McCaffery, JA Adams, I Mitsuhiko, and RJ Tsien. Fluorescent indicators for ca2+ based on green fluorescent proteins and calmodulin. *Nature*, 388:882–7, 1997.

[129] J Monod, J Wyman, and JP Changeux. On the nature of allosteric transitions: A plausible model. *J. Mol. Biol.*, 12:88–118, 1965.

[130] CJ Morton Firth, TS Shimizu, and D Bray. A free-energy-based stochastic simulation of the tar receptor complex. *J Mol Biol.*, 286:1059–74, 1999.

[131] B Munsky, G Neuert, and A Van Oudenaarden. Using gene expression noise to understand gene regulation. *Science*, 336:183–7, 2012.

[132] D Muzzey, CA Gomez-Uribe, JT Mettetal, and A van Oudenaarden. A systems-level analysis of perfect adaptation in yeast osmoregulation. *Cell*, 138:160–71, 2009.

[133] P.C. Nelson. *Biological Physics: Energy, Information, Life*. W.H.Freeman, 1 edition, 2004.

[134] G Neuert, B Munsky, RZ Tan, L Teytelman, M Khammash, and A. van Oudenaarden. Systematic identification of signal-activated stochastic gene regulation. *Science*, 339:584–7, 2013.

[135] S Neumann, K Grosse, and V. Sourjik. Chemotactic signaling via carbohydrate phosphotransferase systems in escherichia coli. *PNAS*, 109:12159–64, 2012.

[136] S Neumann, N Vladimirov, AK Krembel, NS Wingreen, and V Sourjik. Imprecision of adaptation in Escherichia Coli chemotaxis. *PLoS ONE*, 9(1):1–6, 2014.

[137] AW Nguyen and PS Daugherty. Evolutionary optimization of fluorescent proteins for intracellular fret. *Nat. Biotechn.*, 23:335–360, 2005.

[138] B Ni, B Ghosh, FS Paldy, R Colin, T Heimerl, and V Sourjik. Evolutionary remodeling of bacterial motility checkpoint control. *Cell Reports*, 18:866–77, 2017.

[139] Kazuya Nishimura, Saburo Tsuru, Hiroaki Suzuki, and Tetsuya Yomo. Stochasticity in gene expression in a cell-sized compartment. *ACS Synthetic Biology*, 4(5):566–576, 2015. PMID: 25280237.

[140] O Oleksiuk, V Jakovljevic, N Vladimirov, R Carvalho, E Paster, WS Ryu, Y Meir, NS Wingreen, M Kollmann, and V Sourjik. Thermal robustness of signaling in bacterial chemotaxis. *Cell*, 145(2):312–321, 2011.

[141] D. R. Ortega, C. Yang, P. Ames, J. Baudry, J. S. Parkinson, and I. B. Zhulin. A phenylalanine rotameric switch for signal-state control in bacterial chemoreceptors. *Nature Communications*, 4:1–8, 2013.

[142] E. M. Ozbudak, M. Thattai, I. Kurtser, A. D. Grossman, and A. Van Oudenaarden. Regulation of noise in the expression of a single gene. *Nat. Gen.*, 31(1):69–73, 2002.

[143] H. Park, W. Pontius, C.C. Guet, J. F. Marko, T. Emonet, and Ph. Cluzel. Interdependence of behavioural variability and response to small stimuli in bacteria. *Nature*, 468(7325):819–823, 2010.

[144] J.S. Parkinson, G.L. Hazelbauer, and J.J. Falke. Signaling and sensory adaptation in escherichia coli chemoreceptors: 2015 update. *Trends in Microbiology*, 23(5):257–266, 2015.

[145] JS Parkinson and SE Houts. Isolation and behavior of escherichia coli deletion mutants lacking chemotaxis functions. *J. Bacteriol.*, 151:106–13, 1982.

[146] A Paulick, V Jakovljevic, S Zhang, M Erickstad, A Groisman, Y Meir, W S Ryu, N S Wingreen, and V Sourjik. Mechanism of bidirectional thermotaxis in escherichia coli. *eLife*, 6, 2017.

[147] J Paulsson. Prime movers of noisy gene expression. *Nat. Gen.*, 37:937–44, 2005.

[148] JM Pedraza and A Van Oudenaarden. Noise propagation in gene networks. *Science*, 307:1965, 2005.

[149] GE Piñas, V Frank, A Vaknin, and JS Parkinson. The source of high signal cooperativity in bacterial chemosensory arrays. *PNAS*, 113(12):3335–3340, 2016.

[150] W Pontius, MW Sneddon, and T Emonet. Adaptation dynamics in densely clustered chemoreceptors. *PLoS Comp. Biol.*, 9, 2013.

[151] S. L. Porter, G. H. Wadhams, and J. P. Armitage. Signal processing in complex chemotaxis pathways. *Nat. Rev. Microbiol.*, 9(3):153–165, February 2011.

[152] J Prost, JF Joanny, and JM Parrondo. Generalized fluctuation-dissipation theorem for steady-state systems. *Phys. Rev. Lett.*, 103:090601, 2009.

[153] EN Pugh, S Nikonov, and TD Lamb. Molecular mechanisms of vertebrate photoreceptor light adaptation. *Curr. Opin. Neurobiol.*, 9:410–18, 1999.

[154] A Raj, C Peskin, D Tranchina, D Vargas, and S Tyagi. Stochastic mrna synthesis in mammalian cells. *PLoS Biology*, 4, 2006.

[155] A Raj, SA Rifkin, E Andersen, and A Van Oudenaarden. Variability in gene expression underlies incomplete penetrance. *Nature*, 463:913–20, 2010.

[156] A Raj and A Van Oudenaarden. Nature, nurture, or chance: stochastic gene expression and its consequences. *Cell*, 135(2):216–26, 2008.

[157] CV Rao, JR Kirby, and AP Arkin. Design and diversity in bacterial chemotaxis: A comparative study in escherichia coli and bacillus subtilis. *PLoS Biol.*, 2:e49, 2004.

[158] CV Rao, DM Wolf, and AP Arkin. Control, exploitation and tolerance of intracellular noise. *Nature*, 420(6912):231–237, 11 2002.

[159] JM Raser and EK O'Shea. Control of stochasticity in eukaryotic gene expression. *Science*, 304:1811–14, 2004.

[160] JM Raser and EK O'Shea. Noise in gene expression: Origins, consequences and control. *Science*, 309:2010–13, 2005.

[161] A Robinson, JP McDonald, VE Caldaz, M Patel, EA Wood, CM Punter, G Ghodke, MM Cox, R Woodgate, MF Goodman, and AM Oijen. Regulation of mutagenic dna polymerase v activation in space and time. *PLoS Genet.*, 11:e1005482, 2015.

[162] B Rotman. Measurement of activity of single molecules of beta-d-galactosidase. *PNAS*, 15:1987–91, 1961.

[163] H.M. Salis. The ribosome binding site calculator. *Meth. Enzym.*, 498:19–42, 2011.

[164] HM Salis, EA Mirsky, and CA Voigt. Automated design of synthetic ribosome binding sites to control protein expression. *Nat. Biotechn.*, 10:946–50, 2009.

[165] H Salman and A Libchaber. A concentration-dependent switch in the bacterial response to temperature. *Nature Cell Biology*, 9(9):1098–1100, 2007.

[166] I Sampedro, RE Parales, T Krell, and JE Hill. Pseudomonas chemotaxis. *FEMS Microbiol. Rev.*, 39:17–46, 2015.

[167] O. Sandler, S.P. Mizrahi, N. Weiss, O. Agam, I. Simon, and N. Q. Balaban. Lineage correlations of single cell division time as a probe of cell-cycle dynamics. *Nature*, 519(7544):468–471, 2015.

[168] P Sartori and Y Tu. Free energy cost of reducing noise while maintaining a high sensitivity. *Phys. Rev. Lett.*, 115, 2015.

[169] BE Scharf, KA Fahrner, L Turner, and HC Berg. Control of direction of flagellar rotation in bacterial chemotaxis. *PNAS*, 95:201–206, 1998.

[170] E. Schrödinger. *What Is Life? The Physical Aspect of the Living Cell*. Cambridge University Press, 1994.

[171] S Schulmeister, M Ruttorf, S Thiem, D Kentner, D Lebiedz, and V Sourjik. Protein exchange dynamics at chemoreceptor clusters in Escherichia coli. *PNAS*, 105(17):6403–6408, April 2008.

[172] JE Segall, SM Block, and HC Berg. Temporal comparisons in bacterial chemotaxis. *PNAS*, pages 8987–8991, 1986.

[173] JE Segall, MD Manson, and HC Berg. Signal processing times in bacterial chemotaxis. *Nature*, 296:855–7, 1982.

[174] NC Shaner, RE Campbell, PA Steinback, BNG Giepmans, AE Palmer, and RY Tsien. Improved monomeric red, orange and yellow fluorescent proteins. *Nat. Biotechn.*, 22:1567–72, 2004.

[175] NC Shaner, GG Lambert, A Chammas, Y Ni, PJ Cranfill, MA Baird, BR Sell, JR Allen, RN Day, M Israelsson, MW Davidson, and J Wang. A bright monomeric green fluorescent protein. *Nat. Meth.*, 10:407–9, 2013.

[176] NC Shaner, P Steinbach, and RY Tsien. A guide to choosing fluorescent proteins. *Nature*, 2(12):905–909, 2005.

[177] CE Shannon. Communication in the presence of noise. *Proceedings of the IRE*, 37(1):10–21, 1949.

[178] D Shcherbo, CS Murphy, GV Ermakova, EA Solovieva, TV Chepurnykh, AS Shcheglov, VV Verkhusha, VZ Pletnev, KL Hazelwood, PM Roche, S Lukyanov, AG Zaraisky, MW Davidson, and DM Chudakov. Far-red fluorescent tags for protein imaging in living tissues. *Biochemical Journal*, 418(3):567–574, 2009.

[179] E Shelden and P Wadsworth. Observation and quantification of individual microtubule behavior in vivo: microtubule dynamics are cell-type specific. *J Cell Biology*, 120:935–45, 1993.

[180] TS Shimizu, SV Aksenov, and D Bray. A spatially extended stochastic model of the bacterial chemotaxis signalling pathway. *J. Mol. Biol.*, 329(2):291–309, 2003.

[181] TS Shimizu, N Delalez, K Pichler, and HC Berg. Monitoring bacterial chemotaxis by using bioluminescence resonance energy transfer: absence of feedback from the flagellar motors. *PNAS*, 2006.

[182] TS Shimizu, N Le Novere, M.D. Levin, AJ Beavil, BJ Sutton, and D Bray. Molecular model of a lattice of signalling proteins involved in bacterial chemotaxis. *Nature Cell Biology*, 2:792–6, 2000.

[183] TS Shimizu, Y Tu, and HC Berg. A modular gradient-sensing network for chemotaxis in Escherichia coli revealed by responses to time-varying stimuli. *Mol. Sys. Biol.*, 6, June 2010.

[184] G Shinar, R Milo, MR Martínez, and U Alon. Input output robustness in simple bacterial signaling systems. *PNAS*, 104(50):19931–5, 2007.

[185] M Silverman and M Simon. Flagellar rotation and the mechanism of bacterial motility. *Nature*, 249(452):73–74, 1974.

[186] S.A. Simms, M.G. Keane, and J. Stock. Multiple forms of the cheb methylesterase in bacterial chemosensing. *J of Biological Chemistry*, 260:10161–10168, 1985.

[187] M Skoge, Y Meir, and NS Wingreen. Dynamics of cooperativity in chemical sensing among cell-surface receptors. *Phys. Rev. Lett.*, 107:178101, 2011.

[188] ML Skoge, RG Endres, and NS Wingreen. Receptor-Receptor coupling in bacterial chemotaxis: Evidence for strongly coupled clusters. *Biophys. J.*, 90(12):4317–4326, June 2006.

[189] MW Sneddon, W Pontius, and T Emonet. Stochastic coordination of multiple actuators reduces latency and improves chemotactic response in bacteria. *PNAS*, 109(3):805–810, 2012.

[190] V Sourjijk, A Vaknin, TS Shimizu, and HC Berg. In vivo measurement by FRET of pathway activity in bacterial chemotaxis. *Methods Enzymology*, (423):365–91, 2007.

[191] V Sourjik and HC Berg. Binding of the Escherichia coli response regulator CheY to its target measured in vivo by fluorescence resonance energy transfer. *PNAS*, 99(20):12669–12674, 2002.

[192] V Sourjik and HC Berg. Receptor sensitivity in bacterial chemotaxis. *PNAS*, 99(1):123–127, 2002.

[193] V Sourjik and HC Berg. Functional interactions between receptors in bacterial chemotaxis. *Nature*, 428(6981):437–441, 2004.

[194] V Sourjik and NS Wingreen. Responding to chemical gradients: bacterial chemotaxis. *Curr. Op. Cell Biol.*, 24:262–8, 2012.

[195] JL Spudich and DE Koshland. Non-genetic individuality: chance in the single cell. *Nature*, 262(5568):467–471, August 1976.

[196] R.C. Stewart. Activating and inhibitory mutations in the regulatory domain of cheb, the methylesterase in bacterial chemotaxis. *J of Biological Chemistry*, 268:1921–1930, 1993.

[197] R.C. Stewart, A.F. Roth, and F.W. Dahlquist. Mutations that affect control of the methylesterase activity of cheb, a component of the chemotaxis adaptation system in e. coli. *J of Bacteriology*, 172:3388–3399, 1990.

[198] H Strahl and LW Hamoen. Membrane potential is important for bacterial cell division. *PNAS*, 107(27):12281–12286, 2010.

[199] SH Strogatz. *Nonlinear dynamics and chaos: with applications to physics, biology, chemistry and engineering*. Addison-Wesley Publishing, 1994.

[200] M Suël, Jordi Garcia-ojalvo, Louisa M Liberman, and MB Elowitz. An excitable gene regulatory circuit induces transient cellular differentiation. *Nature*, 440:545–550, 2006.

[201] K. Takahashi, S. Tanase-Nicola, and P.R. Ten Wolde. Spatio-temporal correlations can drastically change the response of a mapk pathway. *PNAS*, 107:2473–79, 2010.

[202] Y. Taniguchi, P. J Choi, G.W. Li, H. Chen, M. Babu, J. Hearn, A. Emili, and X. S. Xie. Quantifying E. Coli Proteome and Transcriptome with Single-Molecule Sensitivity in Single Cells. *Science*, 329(5991):533–539, 2010.

[203] X Tao, X Chen, X Yang, and J Tian. Fingerprint recognition with identical twin fingerprints. *PLoS One*, 7:e35704, 2012.

[204] KM Taute, S Gude, SJ Tans, and TS Shimizu. High-throughput 3d tracking of bacteria on a standard phase contrast microscope. *Nat. Comm.*, 6, 2015.

[205] B.L. Taylor and D.E. Koshland. Electron taxis and blue light effect on bacterial chemotaxis. *Journal of Bacteriology*, 123:557–569, 1975.

[206] B.L. Taylor, J.B. Miller, H.M. Warrick, and D.E. Koshland. Electron acceptor taxis and blue light effect on bacterial chemotaxis. *J. Bacteriol.*, 140:567–573, 1979.

[207] S Terasawa, H Fukuoka, Y Inoue, T Sagawa, H Takahashi, and A Ishijima. Coordinated reversal of flagellar motors on a single e. coli cell. *Biophys. J.*, 100:2193–2200, 2011.

[208] TC Terwilliger, JY Wang, and DE Koshland. Kinetics of receptor modification. *Journal of Biol Chemistry*, 261:10814–20, 1986.

[209] M Thattai and A Van Oudenaarden. Intrinsic noise in gene regulatory networks. *PNAS*, 98:8614–19, 2001.

[210] S Thiem, D Kentner, and V Sourjik. Positioning of chemosensory clusters in e. coli and its relation to cell division. *EMBO J*, 26:1615–23, 2007.

[211] RY Tsien. The green fluorescent protein. *Ann. Rev. Biochem.*, 7:509–44, 1998.

[212] Y Tu. The nonequilibrium mechanism for ultrasensitivity in a biological switch: Sensing by maxwell's demons. *PNAS*, 105:11737–41, 2008.

[213] Y Tu. Quantitative modeling of bacterial chemotaxis: Signal amplification and accurate adaptation. *Ann. Rev. Biophys.*, 42:337–359, 2013.

[214] Y Tu and G Grinstein. How white noise generates power-law switching in bacterial flagellar motors. *Phys. Rev. Lett.*, 94:208101, 2005.

[215] Y Tu, TS Shimizu, and HC Berg. Modeling the chemotactic response of Escherichia coli to time-varying stimuli. *PNAS*, 105(39):14855–14860, September 2008.

[216] A Typas and V Sourjik. Bacterial protein networks: properties and functions. *Nat. Rev. Microbiol.*, 13:559–72, 2015.

[217] JJ Tyson, KC Chen, and B Novak. Sniffers, buzzers, toggles and blinkers: dynamics of regulatory and signaling pathways in the cell. *Curr. Opin. Cell Biol.*, 15(2):221–231, April 2003.

[218] A Vaknin. The dynamics in the bacterial chemosensory arrays. *AIP Conference Proceedings*, 1610:34–40, 2014.

[219] A Vaknin and HC Berg. Single Cell FRET imaging of phosphatase activity in the escherichia coli chemotaxis system. *PNAS*, 101(49):170272–7, 2004.

[220] A Vaknin and HC Berg. Osmotic stress mechanically perturbs chemoreceptors in escherichia coli. *PNAS*, 103:592–6, 2006.

[221] N. G. Van Kampen. *Stochastic Processes in Physics and Chemistry*. Elsevier Science, January 1981.

[222] JW Veening, WK Smits, and OP Kuipers. Bistability, epigenetics, and bet-hedging in bacteria. *Ann. Rev. Microbiol.*, 62:193–210, 2008.

[223] GM Viswanathan, SV Buldyrev, S Havlin, da Luz MGE, EP Raposo, and HE Stanley. Optimizing the success of random searches. *Nature*, 401:911–914, 1999.

[224] G.H. Wadhams and J.P. Armitage. Making sense of it all: bacterial chemotaxis. *Nat. Rev. Mol. Cell Biol.*, 5(12):1024–1037, December 2004.

[225] A.J. Waite, N.W. Frankel, Y.S. Dufour, J.F. Johnston, J. Long, and T. Emonet. Non-genetic diversity modulates population performance. *Mol. Sys. Biol.*, 12, 2016.

[226] F Wang, H Shi, R He, R Wang, R Zhang, and J Yuan. Non-equilibrium effect in the allosteric regulation of the bacterial flagellar switch. *Nature Physics*, 2017.

[227] JN Weiss. The hill equation revisited: uses and misuses. *FASEB J*, 11:835–41, 1997.

[228] AJ Wolfe and HC Berg. Migration of bacteria in semisolid agar. *PNAS*, 86(18):6973–6977, September 1989.

[229] J Wong-Ng, A Melbinger, A Celani, and M Vergassola. The role of adaptation in bacterial speed races. *PLoS Comp. Biol.*, 12(6):e1004974, 2016.

[230] S Wright, B Walia, JS Parkinson, and S Khan. Differential activation of Escherichia coli chemoreceptors by blue-light stimuli. *J of Bacteriol.*, 188(11):3962–3971, June 2006.

[231] J Wu, G Li, D Li, DG Long, and RM Weis. The receptor binding site for the methyltransferase of bacterial chemotaxis is distinct from the sites of methylation. *Biochemistry*, 35:4984–93, 1996.

[232] K. Wu, H.E. Walukiewicz, G.D. Glekas, G.W. Ordal, and C.V. Rao. Attractant binding induces distinct structural changes to the polar and lateral signalling clusters in *Bacillus subtillis* chemotaxis. *J of Biological Chemistry*, 286(4):2587–95, 2011.

[233] TM Yi, Y Huang, MI Simon, and JC Doyle. Robust perfect adaptation in bacterial chemotaxis through integral feedback control. *PNAS*, 97(9):4649–4653, 2000.

[234] A Yoney and H Salman. Precision and Variability in Bacterial Temperature Sensing. *Biophys. J.*, 108, 2015.

[235] J. Yu, J Xiao, X Ren, K Lao, and S Xie. Probing gene expression in live cells, one protein molecule at the time. *Science*, 311:1600–3, 2006.

[236] J Yuan and HC Berg. Ultrasensitivity of an adaptive bacterial motor. *J Mol Biol.*, 425:1760–4, 2013.

[237] J Yuan, RW Branch, BG Hosu, and HC Berg. Adaptation at the output of the chemotaxis signalling pathway. *Nature*, 484(7393):233–236, April 2012.

Summary

Many important biological processes are influenced by molecular fluctuations (often called 'noise'), since they often depend on a limited number of chemical reaction events. Stochastic effects in gene expression have been widely studied and it has been established that in a population of cells with the same DNA sequence, and grown under identical conditions, cells show diversity in the protein copy number. However, there are many of open questions remaining into the consequences of such differences in protein levels to more complex phenotypes such as signalling systems. How does the network architecture of signalling systems shape the variability in output parameters? Have networks always evolved towards a state in which diversity in signal processing within a population is minimal? And since these molecular interactions within the network are in principle also probabilistic, is it also possible to measure these additional sources of noise produced the network itself?

In this thesis, we have addressed such questions of variety and fluctuations in a simple biochemical network, namely the chemotaxis pathway in *Escherichia coli*, a textbook example of cellular signalling and behavior. The pathway enables bacteria to control its flagellar motor rotation in response to chemical stimuli and operates only by protein-protein interactions. Single-cell experiments have focussed on measuring the output at the level of the bacterial flagellar motor and have been instructive in establishing behavioural variability, but since this motor itself is a stochastic two-state switch it can obscure upstream signalling dynamics. FRET microscopy has been successful in characterizing the signalling dynamics in population-averaged experiments, but in which information on diversity and fluctuations are lost. We have developed a protocol to apply FRET to measure signalling dynamics in single bacteria over extended times. The efforts to optimize this protocol are explained in chapter 2. We found that the attachment method is a critical step in obtaining a high signal-to-noise and can be further increased by allowing for FRET acceptor maturation after harvesting with up to ~ 25 %. Using the single-cell FRET method, we have studied cell-to-cell variability and temporal fluctuations in bacterial chemotaxis, which is described in chapters 3-6.

In chapter 3, we present *in vivo* measurements of phenotypic diversity or cell-to-cell variability of the chemotaxis pathway of *E. coli*. In isogenic populations simultaneously experiencing identical stimuli, we found considerable variability in adaptation times. In mutants deficient in adaptation, strong variability is observed not only in the steady-state network output, but also in the sensitivity and gain of response to identical ligand stimuli that was likely due to stochastic expression of the dominant chemoreceptors Tar and Tsr. We found, using mutant strains with altered network topologies, that variability in the steady-state network activity is reduced by the phosphorylation feedback loop of the adaptation system mediated by the methylesterase CheB. Without this feedback loop, which is dispensable for

precise adaptation, the network variability is not only enhanced but demonstrates likely detrimental bimodality. These results demonstrate how gene expression variability can influence the design of protein signaling networks.

Two chapters, chapter 4 and 5, are mainly concerned with variability in time of a single cell. These fluctuations are not caused by differences in portein copy numbers due to stochastic gene expression, but rather fluctuations of the protein interactions within the network itself. In chapter 4, we describe measurements of fluctuations due to stochastic kinetics of chemoreceptor methylation and demethylation by the adaptation enzymes. We found that the timescale of these fluctuations ($\sim$ 10 s) agrees well with previously performed motor-level experiments, but the fluctuation magnitude ($\sim$ 45 % as standard deviation over the mean of the signal) was much larger than expected. In chapter 5, we find evidence that this discrepancy can be explained, at least in part, by the existence of another noise source that is independent from the (de)methylation activity. In a fraction of the population of non-adapting cells ($\sim$ 10 %) these fluctuations take the form of stochastic two-state switching. We found that these fluctuations can be observed at intermediate activity bias, which can be controlled by added attractant or genetic modifications in the chemoreceptor. We found a characteristic timescale for the two-state switching of $\sim$ 100 seconds. To our knowledge, these measurements were the first direct measurements of signalling fluctuations in a protein-signaling network. The observation of two-state switching *in vivo* only has been observed in systems that consist of much smaller number of components (by at least one order of magnitude). Together, these results show that stochastic activity of protein complex reveal important insights into the mechanistic functioning of these complexes.

In chapter 6, we explore the origins of two network-level properties of the chemotaxis network. We focus on a limited number of genetic mutations containing only one or a few amino acids in one of the chemosensory array components. These mutants have been implicated in population-averaged experiments with different network-level signaling properties, such as reduced signal cooperativity or reduced ligand response timescales. However, these properties are described by nonlinear functions and hence similar population-averaged behaviour may have very different underlying single-cell responses and we describe single-cell FRET measurements that confirm cooperativity and response swiftness level of single cells. These results indicate that mutations in single amino acids can have a profound impact on signalling properties of the entire network.

Samenvatting

Moleculaire fluctuaties, vaak 'ruis' genoemd, spelen een grote rol in biologische processen, omdat deze processen in veel gevallen het gevolg zijn van een klein aantal chemische reacties. Onderzoek naar ruis in de expressie van genen heeft vastgesteld dat puur door kansprocessen binnen een genetisch identieke populatie van cellen, gekweekt onder identieke condities, het eiwitniveau tussen cellen nog steeds verschilt. Er zijn echter nog vele open vragen over de consequenties van dergelijke ruis voor cellulaire netwerken en gedrag, zoals signaalverwerking in cellen. De vraag is hoe de architectuur van signaalverwerkingsnetwerken de gevolgen van zulke ruis bepaald en of signaalverwerkingsnetwerken altijd geëvolueerd zijn naar een staat waarin er weinig ruis is. De interacties binnen het signaalverwerkingsnetwerk zijn echter in principe ook het gevolg van een kansproces, en de vraag is of we de ruis die door het netwerk zelf worden geproduceerd ook kunnen meten.

In deze dissertatie worden dergelijke vragen over variatie en fluctuaties benaderd met behulp van een simpel biochemisch netwerk, te weten het chemotaxis netwerk in de bacterie *Escherichia coli*, een schoolvoorbeeld van signaalverwerking in cellen. Dit netwerk stelt bacteriën in staat de rotatie van de zweepstaart (of flagellum) in reactie op chemische signalen te veranderen en werkt alleen door middel van eiwit-eiwit interacties. Experimenten op het niveau van een enkele cel hebben zich gericht op het meten van het gedrag van de zweepstaart. Door deze metingen weten we dat dit gedrag veranderlijk is in de tijd, maar aangezien de motor die de zweepstaart laat draaien zelf een stochastische schakelaar is, geven deze metingen slechts een indirect beeld van het signaal dat de motor aanstuurt. FRET microscopie, welke de interactie tussen eiwitten kan meten door een fysisch principe van de afstandsafhankelijke energieoverdracht tussen lichtdeeltjes, is juist zeer succesvol in het meten van dit signaal in experimenten waarin de uitkomst wordt gemiddeld over honderden cellen, maar deze metingen kunnen op hun beurt geen informatie geven over de variaties en fluctuaties in het signaal van een enkele cel. Daarom hebben wij een experimenteel protocol ontwikkeld voor FRET microscopie waarmee de netwerkactiviteit van een enkele bacterie gemeten kan worden. De werkzaamheden die noodzakelijk waren om dit protocol te optimaliseren zijn beschreven in hoofdstuk 2. Met deze FRET methode voor individuele bacteriën hebben we de variatie in signaalverwerking tussen cellen alsmede fluctuaties van de netwerkactiviteit binnen een enkele cell bestudeerd, welke zijn beschreven in de hoofdstukken 3-6.

In hoofdstuk 3 presenteren we *in vivo* metingen van phenotypische diversiteit of cell-cell variatie van het chemotaxis netwerk in *E. coli*. In een genetisch identieke populatie welke dezelfde stimuli ondergaan, vonden we aanzienlijke verschillen in de adaptatietijd van enkele cellen. In cellen zonder adaptatie hebben we grote variatie gezien in de sensitiviteit en amplificatie in de respons van

enkele cellen, welke waarschijnlijk gebeurd door stochastische expressie van de dominante chemoreceptoren Tar and Tsr. Met behulp van mutanten met een veranderde netwerktopologie konden we vaststellen dat de variatie in het netwerksignaal tussen cellen wordt gereduceerd door een terugkoppeling op het signaal door middel van de methylesterase CheB. Zonder deze terugkoppeling, welke niet noodzakelijk is voor perfecte adaptatie, is de variatie tussen cellen niet alleen verhoogd maar laat ook een bimodaliteit zien die vermoedelijk het functioneren van het netwerk bemoeilijkt. Deze resultatien laten zien hoe variatie door genexpressieruis het ontwerp van signaalnetwerken van eiwitten kan beïnvloeden.

De daaropvolgende twee hoofdstukken, 4 en 5, zijn voornamelijk gericht op het bestuderen van variatie over tijd binnen een enkele cel. Deze fluctuaties worden niet veroorzaakt door verschillen in hoeveelheid eiwit door genexpressieruis, maar door fluctuaties van de eiwitinteracties binnen het netwerk zelf. In hoofdstuk 4, worden experimenten beschreven van fluctuaties door de stochastische kinetica van de methylatie van de chemoreceptoren door de adaptatie-eiwitten. De tijdschaal van deze gemeten fluctuaties ($\sim$ 10 s) komen goed overeen met metingen aan de motor, maar de amplitude ($\sim$ 45 %, als de standaarddeviatie over het gemiddelde van het signaal) was veel groterdan verwacht. In hoofdstuk 5 vonden we aanwijzingen dat dit verschil gedeeltelijk verklaard kan worden door een andere, nog niet bekende, ruisbron welke onafhankelijk is van de (de)methylatie activiteit. In een gedeelte ($\sim$ 10 %) van de populatie van cellen waarin methylatie is uitgeschakeld vonden we fluctuaties in de vorm van een binaire schakelaar. We vonden een karakteristieke tijdschaal van ongeveer 100 seconden. Voor zover wij kunnen nagaan zijn deze experimenten de eerste directe metingen van signaalfluctuaties in een signaalnetwerk bestaande uit eiwitten. De observatie van fluctuaties in de vorm van binaire schakelingen in levende cellen is slechts in veel kleinere (ten minste een orde van grootte kleiner) systemen waargenomen. Deze resultatien laten zien dat de stochastische activiteit van eiwitcomplexen inzicht kan verschaffen in het functioneringsmechanisme van deze complexen.

Hoofdstuk 6 onderzoeken we twee netwerkeigenschappen van het chemotaxissysteem. Een klein aantal van genetische modificaties van slechts enkele aminozuren in de componenten van de chemosensorische clusters zijn door eerdere experimenten op populatieniveau in verband gebracht met veranderingen van verschillende eigenschappen van de signaalverwerking, met name een verminderde responscooperativiteit of een verminderde responssnelheid. Deze eigenschappen worden echter door niet-lineare functies beschreven en daardoor kan een vrijwel identieke populatierespons totaal verschillende onderliggende responsen van de individuele cellen bevatten. We beschrijven FRET metingen aan individuele cellen die bevestigen dat de netwerkeigenschappen van het chemotaxis systeem door de mutaties op het niveau van de enkele cel plaatsvinden. Deze resultatien laten zien dat mutaties in enkele aminuzuren van grote invloed kunnen zijn op de signaaleigenschappen van het gehele signaalverwerkingsnetwerk.

About the author

Curriculum vitae

Johannes M. Keegstra (1987) was born in Utrecht, the Netherlands. He graduated with a Bachelor of Arts in Philosophy from the University of Leiden in 2012 and a Master of Science in Applied Physics from Delft University of Technology in 2013, during which he determined mechanical properties of double-stranded RNA using single-molecule techniques in the in the lab of prof. Nynke Dekker and he spend 5 months at the lab of dr. Jan Ellenberg at the European Molecular Biology Laboratory in Heidelberg, Germany. Thereafter, he worked with prof. Tom Shimizu at AMOLF Institute in Amsterdam on chemotaxis in *E. coli*, of which the work is presented in this thesis. Upon completion of his doctorate he will continue his academic career as a postdoctoral researcher at the lab of prof. Roman Stocker at the Swiss Federal Institute of Technogy (ETH) in Zurich, Switserland.

Publications

Publications in this thesis

- **J.M. Keegstra**, K. Kamino, F. Anquez, M.D. Lazova, T. Emonet, T.S. Shimizu. Phenotypic diversity and temporal variability in a bacterial signaling network revealed by single-cell FRET *eLife* **6**:e27455 (2017)
- **J.M. Keegstra**, F. Avgidis, Y. Mulla, J.S. Parkinson, T.S. Shimizu. Non-equilibrium stochastic switching of bacterial chemosensory arrays. *(in preparation)*

Other publications by the author

- P. Szymanska*, N. Gritti*, **J.M. Keegstra***, M. Sultani* and B. Munsky Using noise to control heterogeneity in isogenic populations in homogenous environments. *Physical Biology*, **12** (4) 045003 (2015)
- J. Lipfert*, G.M. Skinner*, **J.M. Keegstra**, T. Hensgens, T. Jager, D. Dulin, X. Hiang, S. Donkers, and N.H. Dekker
  Double Stranded RNA under force and torque: similarities to and striking differences from DNA, *PNAS*, **111**(43), *15408-15413* (2014)
- A.R. Hall, **J.M. Keegstra**, M.C. Duch, M. Hersam and C. Dekker
  Translocation of Single-Wall Carbon Nanotubes Through Solid-State Nanopores, *Nano Letters*, **11** (6), *2446* (2011)